9. ANALOGUES FOR UNSATURATED ZONE FLOW

9.1 INTRODUCTION

The conceptual and numerical modeling methodologies for the unsaturated zone (UZ) at Yucca Mountain are applicable to other sites, including Apache Leap (Arizona), Box Canyon (Idaho), Rainier Mesa (Nevada), and other semi-arid sites in fractured rock. These and other examples are presented in *Natural Analogs for the Unsaturated Zone* (CRWMS M&O 2000 [141407]) and in the *Yucca Mountain Site Description* (CRWMS M&O 2000 [151945], Sec. 13). Analogues for climate and infiltration processes are presented in the *Yucca Mountain Science and Engineering Report* (S&ER) (DOE 2001 [153849], Table 4-5). Analogues for UZ flow and seepage processes are listed in the S&ER (DOE 2001 [153849], Table 4-6). In general, these analogues contribute to providing confidence in the understanding of paleoclimatic conditions, the bounds on various climate models, the efficacy of a UZ in isolating nuclear waste, the occurrence of very limited seepage in the UZ, and limited fracture-matrix interactions.

Section 9 presents results of a quantitative analogue investigation that had the objective of utilizing related data sets gathered at the Idaho National Engineering and Environmental Laboratory (INEEL) to test the dual-permeability approach of the Yucca Mountain UZ flow model at another site in an attempt to match results of field tests, thus building confidence in the UZ modeling approach. This section also presents a number of possible locations and configurations for testing the drift shadow zone concept in analogous settings and conditions.

9.2 UZ FLOW MODEL

The UZ flow model is described in *Unsaturated Zone Flow and Transport Model Process Model Report* (UZ PMR) (CRWMS M&O 2000 [151940]) and in the S&ER (DOE 2001 [153849], Section 4.2.1). Available site data are used to provide infiltration and percolation flux distributions and hydrologic properties. The model accounts for the occurrence of perched water and the effects of the PTn unit and fault zones on flow in the UZ.

Upper bound limits on infiltration rates and percolation fluxes at Yucca Mountain are estimated based on multiple approaches, including analyses of chloride and chlorine-36 isotopic ratios, calcite deposition, and the occurrence of perched water. The analysis of chloride data indicates that the average percolation rate over the model domain at Yucca Mountain is about 4.6 mm/yr. Analysis of calcite deposition gives infiltration rates of 2 to 20 mm/yr in the vicinity of borehole USW WT-24. To match perched water occurrences, three-dimensional model calibrations require that the present-day infiltration rate be greater than 1 mm/yr, with an upper limit of about 15 mm/yr (DOE 2001 [153849], Section 4.2.1.3.2). Infiltration and flow patterns at Yucca Mountain are summarized below.

Rainfall for the modern mean climate is about 190 mm/yr (7.5 in/yr) resulting in average steady-state net infiltration of 4.6 mm/yr (0.18 in/yr, DOE 2001 [153849], Table 4-11). The net infiltration is episodic, with a significant amount infiltrating only every few years. There is large spatial variability of infiltration, with most water infiltrating on ridge-tops and in the upper reaches of washes where there is little alluvial cover. Fracture flow dominates in the Tiva Canyon welded hydrogeologic unit (TCw), transmitting water rapidly through the TCw to the

underlying Paintbrush tuff nonwelded hydrogeologic unit (PTn). Flow through the PTn is primarily matrix flow with most of the fast flow occurring via faults, although this represents only a very small fraction of the total flow. Lateral flow occurs in the PTn.

Episodic flow into the Topopah Spring welded hydrogeologic unit (TSw) is damped by the PTn to the extent that flow can be considered steady-state at the boundary to the TSw. However, at or near major faults, episodic flow may still persist through the PTn. Fracture flow dominates in the TSw because this unit is densely welded and highly fractured; additionally, within some subunits of the TSw, the low-permeability matrix is incapable of transmitting the percolation flux estimated to be moving through the unit. Fracture flow in the potential repository horizon, which intersects the Topopah Spring middle nonlithophysal, lower lithophysal and lower nonlithophysal stratigraphic units, is estimated to range from 84 to 94 percent of the total water flow.

Water drainage in the potential repository units is expected to be good, owing to the generally high fracture permeability ($\sim 10^{-11}$ to 10^{-10} m^2 [10^{-10} to 10^{-9} ft^2]) (DOE 2001 [153849], Section 4.2.1.2.5). Evidence for fast or preferential flow is seen at the potential repository horizon, primarily near major faults. It is estimated that the fast component of flow is less than a few percent of the total flow.

9.3 THE SUBSURFACE DISPOSAL AREA AT THE IDAHO NATIONAL ENGINEERING AND ENVIRONMENTAL LABORATORY AS AN ANALOGUE FOR TESTING YUCCA MOUNTAIN MODELING APPROACHES

This section discusses modeling of UZ flow and tracer tests at INEEL. Modeling of UZ transport at this site is discussed in Section 10. Section 9.3.1 provides information on the geologic and hydrologic setting of the Radioactive Waste Management Complex (RWMC) at INEEL as background for a flow modeling study in Section 9.3.2 and a radioactive transport model in Section 10.3. Further discussion comparing similarities and differences between INEEL and Yucca Mountain is found in Section 10.3.5.

9.3.1 Background

Between 1952 and 1986, approximately 180,000 m^3 of transuranic and low-level radioactive mixed wastes, containing about 9.5 million curies of radioactivity, were buried in unlined trenches and pits in shallow sediment above basalt flows at the INEEL in the 144,100 m^2 Subsurface Disposal Area (SDA) of the Radioactive Waste Management Complex (RWMC) (Cecil et al. 1992 [156256], p. 709). Included with these buried wastes were approximately 334,000 liters of transuranic-contaminated mixed-waste sludges that were absorbed on calcium silicate and placed in 55-gallon steel drums (Rawson et al. 1991 [156439]). Since 1970, transuranic wastes have been stored in containers placed above ground on asphalt pads in a part of the RWMC known as the transuranic disposal area. Subsurface disposal of radioactive waste at the SDA is planned to continue until at least 2003 (Lockheed Idaho Technologies Company 1995 [156430]). Environmental monitoring beneath the SDA in both the unsaturated and saturated zones has resulted in positive detections of americium, plutonium, and other waste products that have migrated from the SDA (Dames and Moore 1992 [157409], pp. 73–74; Becker et al. 1998 [157407], pp. 4-36 to 4-37), thereby raising concerns about the long-term

water quality of the Snake River Plain Aquifer (SRPA), the principal source of potable groundwater in the area. Effort is underway to evaluate the long-term risk posed to the aquifer by past waste-disposal practices (Magnuson and Sondrup 1998 [156431]; Becker et al. 1998 [157407]) and to determine the necessity of potentially costly remedial strategies, including exhumation and redisposal of the buried waste.

9.3.1.1   Geologic and Hydrologic Setting

The geologic and hydrologic setting of the RWMC has been described in a series of reports by the U.S. Geological Survey (USGS) and the U.S. Department of Energy (DOE) and its contractors (e.g., Rightmire and Lewis 1987 [156440]; [156441]; Magnuson and Sondrup 1998 [156431]). The top of the surficial sediment in which the wastes are buried is approximately 175 to 180 m above the regional water table. The thick UZ beneath the SDA contains 13 individual basalt flows ranging in thickness from less than 1 m to 17 m and averaging about 5 m in thickness (Knutson et al. 1990 [107839], p. 21). The individual basalt flows can be subdivided into four zones, with varying amounts of rubble, vesicles, and fractures, and grouped on the basis of the presence of three major sedimentary interbeds. Three sedimentary interbeds at 9 m, 34 m, and 73 m have been used to subdivide the basalts into A-, B-, C-, and D-group basalts; correspondingly, the 9 m, 34 m, and 73 m interbeds are alternatively known as the A-B, B-C, and C-D sediment layers (Figure 9.3-1).

Annual precipitation at INEEL ranges from 13 to 36 cm/yr, with an average of 20 cm/yr. About 30 percent of the annual precipitation typically occurs as snow (Barraclough et al. 1976 [156426], p. 45). Chlorine-36, tritium, and neutron-logging data from a series of shallow boreholes drilled just outside the northern boundary of the SDA provided estimates of background infiltration rates for undisturbed soils of 0.36 to 1.1 cm/yr (Cecil et al. 1992 [156256], p. 709). Infiltration rates within the SDA have been estimated to be higher than the background infiltration rates because of the drifting and accumulation of snow within the SDA. Based on neutron-probe measurements of soil moisture changes for the years 1994 to 1995 and weather data extending back to 1952, Martian (1995 [156432], pp. 32–36) estimated that the spatially and temporally variable infiltration rates within the SDA have averaged between 6 and 10 cm/yr since 1952. Only two of the seventeen neutron-probe boreholes were located in the soils within the trenches; therefore, moisture content changes and infiltration rates through the trench fill are not as well characterized as the areas between the trenches. In addition, the SDA has been flooded three times (1962, 1969, and 1982) as a result of the local accumulation of overland flow associated with rapid snowmelt (Vigil 1988 [157416], p. 1, 8). Estimates have been made of the amounts of water that infiltrated (Vigil 1988 [157416]) and which areas of the SDA were flooded (Magnuson and Sondrup 1998 [156431], Figures 2–17). The average depths of the infiltrated water in the flooded areas in the SDA were estimated by Magnuson and Sondrup (1998 [156431], Tables 2–3) to be 0.17 m in 1962, 0.12 m in 1969, and 0.08 m in 1982.

Perched water has been encountered by boreholes within the SDA at depths that correspond roughly to the tops of the sedimentary interbeds (Rightmire and Lewis 1987 [156441], pp. 43–45, Figure 10). Rightmire and Lewis (1987 [156441], p. 45) proposed a hypothesis that the source of at least some of the perched water was actually infiltration from spreading areas, located about 1.7 km to the southwest of the SDA. This infiltration migrated laterally in the UZ along and across the interbeds. Water is diverted from the Big Lost River into these spreading

areas during periods of high flow (>14 m^3/s) to minimize flooding to downstream areas. Support for the hypothesis that the deeper perched water beneath the SDA originated from the spreading areas seemed to Rightmire and Lewis (1987 [156441], p. 65) to be provided by delta-deuterium (δD) and delta oxygen-18 (δ^{18}O) data. The δD and δ^{18}O values of the deep perched water indicated little evidence for evaporation compared to shallow perched water or to groundwater from the regional aquifer, a relation that Rightmire and Lewis (1987 [156441]) considered to be consistent with their hypothesis that the deep perched water originated from the rapid infiltration (and minimal evaporation) of large amounts of water through the spreading areas. For a comparison of the hydrologic settings of INEEL and Yucca Mountain, see Section 10.3.5.1.

9.3.1.2   Surficial Sediments and Sedimentary Interbeds

The surficial sediments consist of the undisturbed areas between the waste trenches and the trench backfill, which is a mixture of excavated material. In some cases, the trenches and pits were originally excavated down to the top of the uppermost basalt layer; however, in these cases a sediment buffer ranging in thickness from 0.67 to 1.0 m was placed in the trench between the waste and the underlying basalt (Rawson et al. 1991 [156439]).

9.3.1.2.1   Mineralogy

The predominant minerals in surficial sediments and sedimentary interbeds are quartz, plagioclase with the composition of labradorite, pyroxene (probably augite), potassium feldspar, clay, and calcite (Rightmire and Lewis 1987 [156441], p. 11). The percentage of clay is higher and the percentages of plagioclase, potassium feldspar, and pyroxene are lower in the surficial sediments compared to the sedimentary interbeds. Calcite is often 10% or more by weight of the surficial material and sedimentary interbeds (Rightmire and Lewis 1987 [156441], p. 26), with much higher percentages of calcite present locally.

The 9 m interbed (A-B Sediment Layer) contains some organic-rich paleosols, with the organic material possibly introduced by infiltrating water, as well as a red color (due to the oxidation of ferrous iron derived from minerals in the nearby basalts). The 34 m interbed (B-C Sediment Layer) also contains a dark-brown organic-rich soil horizon and caliche, amorphous silica, and Ca-smectite. The 73 m interbed (C-D Sediment Layer) has a red color resulting from iron oxyhydroxides throughout its entire thickness (Rightmire and Lewis 1987 [156441], pp. 24–28).

A study of the clay mineralogy of the surficial sediment, the sedimentary interbeds, and fill material of fractures in the basalt indicated that the dominant clay species are illite, followed by mixed illite/smectite, and finally, kaolinite plus chlorite (Rightmire and Lewis 1987 [156441], Table 8). The smectite that is present is mainly a calcium smectite (Rightmire and Lewis 1987 [156441], p. 40).

9.3.1.2.2   Geochemical Properties

Four measurements of the cation exchange capacity (CEC) of the surficial sediments ranged from 11 to 27 meq/100 g, with an average of 19 meq/100 g (Rightmire and Lewis 1987 [156441], Table 5). There was no apparent correlation between the CEC and the clay content of the sediments. The CEC of the interbed sediments is highly variable (0.9 to 36 meq/100 g) and

appears to be related to the percentage of the expandable layer clays present as either pure smectite or mixed illite/smectite (Rightmire and Lewis 1987 [156441], pp. 33–34).

The distribution coefficient (K_d) values of various radionuclides are given for the surficial sediments, sedimentary interbeds, and basalts in Table 9.3-1 (Dicke 1997 [157410], Table 1). The K_d values were measured using composite samples from the interbed sediments and crushed basalts with the fines removed. The reported values for Am, Cs, Co, Hg, Pu, Sr, Tc, and U were based on site-specific data, with values for other elements estimated from the literature or by analogy with chemically similar elements (Dicke 1997 [157410], pp. 10–11). In cases where literature values were used, the data were screened to remove those values obtained using water compositions very dissimilar to that of water that is present in the UZ beneath the SDA. Data from the literature were also adjusted to reflect differences in the amount and type of clays present in the test material and in the surficial and interbed sediments (Dicke 1997 [157410], p. 5). The data indicate higher K_d values for the sediments, possibly because of a greater amount of reactive minerals, such as smectite, in the sediments. Because the interbed sediments were combined in a single sample, there is no basis for estimating how the sorptive properties vary among the interbeds.

9.3.1.2.3   Unsaturated Zone Matric Potentials

A summary of the matric potentials measured beneath the SDA in the surficial sediments and sedimentary interbeds using tensiometers, heat-dissipation probes, and gypsum blocks was presented by McElroy and Hubbell (1990 [156433]). In the surficial sediments, the shallowest measurements ranged between about -0.2 and -1.3 bars, reflecting seasonal wetting and drying cycles. The deepest measurements taken from near the sediment/basalt interface were near 0 bars, indicating near-saturated conditions. Hydraulic gradients varied over time, ranging between upward and downward flow within the upper 1.2 to 3.3 m of the sediment profile, depending on the location of the borehole, but were consistently downward beneath this range of depths.

The equilibrium matric potentials within the 9 m, 34 m, and 73 m interbeds were between -1.4 and -0.3 bars. In general, wetter conditions existed at the tops of the interbeds compared to the bottoms, and hydraulic gradients across the interbeds were greater than unity.

9.3.1.2.4   Unsaturated Zone Gas Chemistry

Soil gas samples taken from a 0.3 to 0.76 m depth in the surficial sediment at a site approximately 11 miles from the SDA were reported by Rightmire and Lewis (1987 [156441], Table 12). The data from this site may be representative of conditions at the SDA prior to its development as a waste disposal area. The chemistry of the soil gas samples closely resembled the chemistry of air, except for $CO_2(g)$, whose concentration in the soil gas was several times higher than in the atmosphere. The logarithm of carbon dioxide partial pressure (log P_{CO2}) and the delta carbon-13 value ($\delta^{13}C$) of the $CO_2(g)$ were observed to vary seasonally and with depth in the soil zone. Rightmire and Lewis (1987 [156441], p. 59) concluded that log P_{CO2} values (expressed as bar) of -2.84 to -3.04, and $\delta^{13}C$ values of -15.5 to -19.6 per mil were characteristic of shallow soil zone gas in late spring, summer, and early autumn, and that log P_{CO2} values of -2.97 to -3.09, and $\delta^{13}C$ values of -16.4 to -17.2 per mil were characteristic of shallow soil zone gas in early spring. Snow melt in early spring has been hypothesized to be the principal source of

recharge at the SDA (Rightmire and Lewis 1987 [156441], p. 59). A comparison of the geochemical settings of INEEL and Yucca Mountain is presented in Section 10.3.5.2.

9.3.2   Modeling the Large-Scale Aquifer Pumping and Infiltration Test at INEEL

Regional and local-scale Large-Scale Aquifer Pumping and Infiltration Test (LPIT) models were developed as a goal of this work to address issues related to the fate and transport of radionuclides from the RWMC. Modeling activities related to this work were documented in Simmons (2002 [157578], SN-LBNL-SCI-186-V1, pp. 17–21). A companion study that used some of the same data sets to investigate radionuclide retardation is presented in Section 10.3. A location map of the RWMC and SDA sites within INEEL is provided in Figure 9.3-2. Statistically significant radionuclide concentrations have been measured as deep as 43 m (140 ft) and possibly deeper (Becker et al. 1998 [157407], pp. 4-23 to 4-39) beneath the SDA in core samples from a sedimentary interbed. This is thought to be a consequence of the SDA having been flooded in 1962, 1969, and 1982 (Section 9.3.1.1), when infiltrating water may have initiated subsurface migration of the plutonium-contaminated waste. The migration pathway is suspected to be vertically downward through the unsaturated basaltic lava flows and then laterally on the low permeability (silt, clay) interbeds as ponded-water conditions develop. Lateral transport of the radionuclides is suspected to have been enhanced by water infiltrating from the spreading area (Figure 9.3-2), causing ponded-water conditions at a scale significantly larger than the SDA. The fate and transport of radionuclides at the regional scale involves the RWMC, the spreading area, and the inferred saturated zone pathway potential that radionuclides would take from beneath the RWMC to the INEEL boundary (Magnuson and Sondrup 1998 [156431]).

Migration of radionuclides from the RWMC is dependent upon the mechanisms controlling unsaturated flow of infiltrating water. It is also dependent upon the fate and transport of radionuclides within the infiltrating water as it flows through the undulating fractured basaltic lava flows and sedimetary interbeds beneath the SDA. To address these issues, the LPIT was conducted in the summer of 1994 to mimic the intermittent flood events observed at the SDA. The test was located approximately 1.43 km south of the RWMC within the same geological units (Figure 9.3-2). Details concerning the location, design, implementation, and data sets collected during the LPIT are summarized in Dunnivant et al. (1998 [156402]). Magnuson (1995 [156404]) developed a numerical model to simulate the highly transient water infiltration and ponding conditions that existed during the LPIT, as well as transport of the conservative selenium (^{75}Se) tracer introduced in the infiltrating water. The modeling approach involved determining parameters controlling unsaturated and saturated flow and transport in the fractured basalt and sedimentary interbeds. The model was calibrated to ponded water hydrographs and ^{75}Se breakthrough curves within the ponded water measured during the LPIT.

The goal of the new modeling presented in Section 9.3.2 was to build confidence in the modeling approach used for UZ process modeling at Yucca Mountain by comparing simulations to results of the LPIT. To achieve the goals of this work, both regional and local-scale LPIT models were developed. These models were based upon the work of Magnuson (1995 [156404]) and Magnuson and Sondrup (1998 [156431]). The sequence of model development was first to use a local-scale LPIT model (Figure 9.3-2) to determine a set of hydrological parameters by simultaneous calibration to multiple hydrographs, while using a dual-permeability representation

of the basalt fracture and matrix continua. These parameters would represent the large-scale properties of the lithological units affected by the field-scale LPIT test as used in the dual-permeability approach rather than local-scale heterogeneities influencing individual hydrographs. Calibration of the model to the LPIT hydrographs and ^{75}Se breakthrough curves is important from the perspective of the work conducted in support of the potential Yucca Mountain repository. This is because it tests confidence in the dual-permeability approach, which is also used to represent flow and transport processes that are anticipated to occur in the tuff fracture and matrix continua at Yucca Mountain. The next step in the sequence of model development was to use hydrological parameters obtained from the LPIT calibration to simulate the fate and transport of radionuclides from the SDA in the regional model. The dimensions of the regional model are shown in Figure 9.3-2. Results presented here are limited to the LPIT analysis.

9.3.3 Conceptual and Numerical Model

The LPIT consists of a 183 m diameter infiltration pond that was constructed by removing surficial soil to build a 1.5 m high earthen berm. The floor of the infiltration pond was highly uneven, with approximately 80% of the basin floor consisting of a thin layer of soil overlying the basalt, while the remaining 20% consisted of exposed and elevated basalt. The water depth in the infiltration pond ranged from 0.3 m to 2 m (Dunnivant et al. 1998 [156402], p. 950). The area beneath the infiltration pond that was instrumented and influenced by the LPIT test consists of three separate basalt flows (the A, B, and C basalts) with a laterally continuous dense clay sedimentary interbed between the B and C basalts. No sedimentary interbed was found between the A and B basalt flows at the LPIT site.

The three-dimensional model (3–D) made to represent the region influenced by the LPIT used a radial coordinate approach consisting of 20 spokes evenly spaced at 18 degree intervals. The centroids of the elements are shown in plan view in Figure 9.3-3a, which shows contours of the elevation of the top of the B-C interbed. A radial coordinate approach was used because during the LPIT, the infiltrating water was observed to pond on the B-C interbed. It was expected to flow radially away from the perimeter of the infiltration pond, with flow controlled by the topography of the B-C interbed. Lateral flow caused by ponding on the B-C interbed was detected in wells located on the B, C and E rings (Figure 9.3-3a) at several locations (Burgess 1995 [156401]). The perimeter of the LPIT model was located sufficiently far from the E ring to remove any influence of boundary conditions. The surface of the B-C interbed is irregular and is crudely approximated by the plan-view discretization shown in Figure 9.3-3a. Note that this discretization does not place the centroid of a node at the exact position of a well where a specific hydrograph was measured and therefore at the exact elevation of the B-C interbed. This approximation was adopted because of constraints in model size required to achieve reasonable calibration times.

Figure 9.3-3b shows a vertical E-W cross-sectional cut through the center of the model. This figure shows the undulating thickness of the A and B basalts and the B-C interbed. The centroids of the elements are shown in cross section in Figure 9.3-3b, indicating significant mesh refinement at the interface between the B basalt and B-C interbed. Grid refinement exercises necessitated 0.02 m thick elements at this interface to obtain a convergent solution to the physics of water ponding on top of the B-C interbed, while simultaneously imbibing and infiltrating through it. In total, 28 elements were used to discretize the domain in the vertical direction.

Figure 9.3-3b also shows the steady-state water saturations in the fracture continuum calculated using a background infiltration rate of 0.01 m/yr (Cecil et al. 1992 [156256], p. 713). Simulation results indicate that the silt/clay-like nature of the surficial sediments and B-C interbed retain a higher water saturation than the basalt fracture continuum.

Unsaturated flow was simulated using iTOUGH2 with the EOS9 module, which solves Richards' equation, while ^{75}Se transport was simulated using the EOS7r module. The mesh was constructed using a dual-permeability representation for the basalt fracture and matrix continua, while the surficial sediments and B-C interbed were simulated as a single matrix continuum. The dual-permeability grid is used in an analogous manner to that used in simulating site-scale unsaturated flow at Yucca Mountain (Barenblatt et al. 1960 [156255]; Pruess and Narasimhan 1985 [101707]; Bandurraga and Bodvarsson 1999 [103949]). Within the context of the dual-permeability approach, various methods are proposed to reduce the interfacial area between the fracture and matrix continua, and hence the degree to which they interact. They range in complexity from a constant scaling factor (Bandurraga and Bodvarsson 1999 [103949]) to the "active fracture" model of Liu et al. (1998 [105729]). The constant scaling factor approach was adopted for this study to reduce the interfacial area between the basalt fracture and matrix continua. This simplification was adopted given the transient nature of the LPIT test and because the "active fracture" model has only been validated for steady-state flow within the site-scale Yucca Mountain model.

The background infiltration rate prescribed to all surface nodes inside the infiltration pond is shown on Figure 9.3-4. The rate was calculated as part of a water management system and water balance analysis by Starr and Rohe (1995 [156400]). Additional boundary conditions for simulating unsaturated flow within the LPIT model include the sides of the model, which were assigned to be impermeable boundaries, while the bottom of the model is prescribed as a constant-water-pressure condition. For the LPIT transport model, 2 Ci of ^{75}Se was added to the infiltration pond water (approximately 31,650 m^3) and allowed to infiltrate into the fractured basalt from Day 6 to Day 17. The mass fraction of ^{75}Se in the infiltrating water was normalized to 1×10^{-3}, given the linear nature of the advection-dispersion equation describing transport of the conservative ^{75}Se tracer and the lower limits on the convergence tolerance of the Newton and iterative sparse matrix solver schemes (approximately 1×10^{-6}). This scaling is evident in Figure 9.3-8.

9.3.4 Hydrological Parameter and Perched Water Hydrograph Data

Perched water hydrograph data were collected at 17 locations as presented in Burgess (1995 [156401]). These were collected in wells located primarily on the A, B, and C rings (see labeled symbols in Figure 9.3-3a) and with the screen located at the B basalt—B-C interbed interface. Hydrographs were not observed at all locations because of difficulties in completing the well at this interface. Of the 17 hydrographs, six were selected for the calibration effort. Results of numerical tests indicated that inversion using the full 3-D LPIT model containing all 17 hydrographs was too computationally intensive; therefore, a wedge of nodes on radial spokes of 342°–0°–18°–36° was extracted to calibrate simultaneously to hydrographs in wells B04N11, C04C11, B06N11, and C06C11. This set of hydrographs was chosen for calibration because it contained two of the three C–ring hydrographs and matched B– and C–ring wells on the same radial angle. Although well B05O11 contained an observed hydrograph and was within this

wedge, it was not used during the inversion in order to act as a control to test the predictive capability of the calibrated parameter set. The hydrograph at well B08N11 was also independently used as part of a separate calibration to yield a parameter set to test for significant differences between calibrated parameters across the region influenced by the LPIT. The six hydrographs introduced here will be presented in Section 9.3.6, along with calibration results. Selenium-75 breakthrough curves within the ponded water were collected at nine locations, as presented in Burgess (1995 [156401]). Of the nine breakthrough curves, the B04N11 and C04C11 data were selected for calibration because they were within the 342°–0°–18°–36° submodel described above. Furthermore, they have matching B and C ring wells on the same radial angle.

Hydrological parameters relevant to the fractured basalt and sedimentary interbed stratigraphy at the LPIT site were identified in a literature survey to constrain the calibration procedure. These parameters are listed in Table 9.3-2. Because none of the laboratory analysis was done on cores obtained specifically from the LPIT site, only the mean, maximum, and minimum values were used to cover the range over which they may be expected to vary for lithological units in the LPIT area. The relevant parameters include the basalt matrix continuum permeability, k_{BM}; and porosity, ϕ_{BM} (Knutson et al. 1990 [107839], p. 3-93); the B-C interbed matrix continuum permeability, k_{BCM}; porosity, ϕ_{BCM}; residual water saturation, S_{wrBCM}; and van Genuchten capillary pressure parameters α_{BCM} and m_{BCM} (McElroy and Hubbell 1990 [156433]). The properties of the B-C interbed vary significantly because this unit was observed to vary in lithology from a fine silt to clay (McElroy and Hubbell 1990 [156433]). Fracture spacing for the basalt was set to 2.6 m for the entire thickness of the basalt units (Grossenbacher and Faybishenko 1997 [107832]).

All relevant unsaturated flow parameters in the hydrological model are listed in Table 9.3-3. Flow parameters shown in Table 9.3-3 but not discussed in this section were not measured from cores taken at INEEL in the fractured basalt–sedimentary interbed stratigraphy, they were instead based on previous INEEL modeling work conducted by Unger et al. (2000 [156398]). Selenium-75 transport parameters such as the dispersivity and tortuosity of the basalt and B-C interbed were not measured as part of prior laboratory or field investigations. Therefore, it is assumed that ^{75}Se does not undergo either molecular or hydrodynamic dispersion over the 60–day time frame of the LPIT. Hydrodynamic dispersion of the ^{75}Se breakthrough curves will occur instead because of imbibition between the basalt fracture and matrix continua.

9.3.5   Hydrograph Calibration Results

Initial manual calibration indicated that the six most sensitive parameters controlling the calibration of the LPIT model to the hydrographs were the basalt fracture–matrix continua interfacial area constant-scaling factor A_{BFM}, the basalt fracture continuum permability k_{BF}, the basalt matrix continuum permeability k_{BM}, the B-C interbed matrix continuum permeability k_{BCM}, the B-C interbed van Genuchten capillary pressure parameters α_{BCM} and m_{BCM}. The basalt fracture and matrix continua porosities were not sensitive parameters controlling calibration. This is because imbibition of the infiltration front from the basalt fracture continuum to the matrix continuum controlled its downward advection rate rather than the porosity, because of the initial dry conditions present at the site. This is shown on Figure 9.3-5, which depicts the water saturation in the fracture and matrix continua at 35.5 days. At this point, ponding of water is well

developed on the B-C interbed and significant quantities of water have been imbibed into the matrix continua within the migration path of the infiltration front.

Parameter estimation during calibration was performed by iTOUGH2 using a Levenberg-Marquardt algorithm. Five parameters were included for estimation: k_{BF}, k_{BM}, k_{BCM}, α_{BCM} and m_{BCM}. Parameter A_{BFM} was manually adjusted because changes to this parameter required rebuilding the mesh. Initial manual adjustment indicated that a value of $A_{BFM} = 0.01$ provided the best fit to the data when using a Brooks-Corey relative permeability curve, which was also observed by Unger et al. (2000 [156398], p. 14). A van Genuchten relative permeability curve was not used in this study because it caused excessive numerical difficulties when simulating ponding because of its steep gradient at water saturations approaching unity.

Figure 9.3-6 shows simultaneous calibration results to hydrographs B04N11, C04C11, B06N11, and C06C11 using the 342°–0°–18°–36° submodel extracted from the full 3–D LPIT model. This model will be referred to hereafter as the "2–D model," while the entire LPIT model will be referred to as the "3–D model." The symbols in Figure 9.3-6 represent water pressure and indicate ponded-water elevation within the fracture continuum of the B basalt on top of the B-C interbed, where reference atmospheric gas–phase pressure is 85 kPa. Calibration was performed to a subset of the data points shown in Figure 9.3-5 that were chosen to be more evenly spaced in time to prevent biasing the calibration to regions where the data were collected more frequently. Calibration parameters were obtained by setting $A_{BFM} = 0.01$, while the sensitivity of the other five calibration parameters to A_{BFM} was determined by doubling it to $A_{BFM} = 0.02$ and then by halving it to $A_{BFM} = 0.005$. Parameters obtained from the iTOUGH2 calibration are provided in Table 9.3-3.

Comparison of calibrated parameters obtained with $A_{BFM} = 0.01$ indicates that the estimated basalt matrix permeability is almost equal to the mean shown in Table 9.3-2, the B-C interbed permeability is just above the minimum observed value, and the B-C interbed van Genuchten parameters are also near the mean of the values in Table 9.3-2. Although the data in Table 9.3-2 were not obtained from the LPIT site, their close correspondence to the estimated parameters does build confidence in the ability of the LPIT model to yield a spatially averaged set of hydrological parameters to fit the hydrographs. Comparison of calibrated parameters for the three different values of A_{BFM} indicates that the basalt fracture continuum permeability remains constant at $k_{BF} = 3 \times 10^{-10}$ m^2 and is insensitive to A_{BFM} over the range tested. The basalt matrix continuum permeability increases by a factor of 2.51 as A_{BFM} is halved, and decreases by a factor of 2.51 as A_{BFM} is doubled. This indicates that basalt fracture–matrix imbibition is an important process controlling calibration, with A_{BFM} and k_{BM} adjusting themselves proportionately to maintain the same amount of flow into the matrix continuum. Interpreting the response of the B-C interbed parameters to variations in A_{BFM} is considerably more difficult, except that m_{BCM} reaches (and was constrained during calibration by) the maximum observed value for $A_{BFM} = 0.005$, thereby reducing confidence in the physical relevance of the calibration values. In general, given the standard deviation of the estimated parameters, no significant difference exists within two standard deviations between the three parameter sets listed in Table 9.3-4.

The full 3–D LPIT model was used to determine the effect of having reduced the mesh size to the four radial angles of 342°–0°–18°–36° to calibrate to the four hydrographs shown in Figure 9.3-6. The greatest deviation occurs for hydrographs B06N11 and C06C11 because the former is

situated in a local depression, while the latter is situated on a local mound in the elevation of the B-C interbed, as shown on Figure 9.3-3a. Therefore, plan-view grid refinement is necessary to obtain increased numerical convergence for parameters listed in Table 9.3-4. The physical relevance of the converged parameters would still be limited by the sparse distribution of points providing information on the elevation of the B-C interbed.

The full 3–D LPIT model was also used to determine how well the calibrated parameters matched the control hydrograph B05O11 that was located within the 2–D submodel, as well as hydrograph B08N11 that was located outside of the 2–D submodel. Figure 9.3-7a shows that the 3–D model successfully modeled the control hydrograph, thus building confidence in the physical relevance of the estimated parameters. Figure 9.3-7b shows that when the 3–D model is used to simulate the B08N11 hydrograph using parameters from Table 9.3-4, the predictive capacity of the estimated parameters diminishes. B08N11 is the only hydrograph shown because it exhibited the worst fit of the hydrographs located outside of the 2–D submodel. An additional 2–D submodel at a radial angle of 288° was extracted from the 3–D LPIT model to calibrate to the B08N11 data. Calibration was performed with $A_{BFM} = 0.01$ only; the results are shown on Figure 10.3-7b, with the final calibrated parameters listed in Table 9.3-5. Analysis of the parameters in Tables 9.3-4 and 9.3-5 indicates that for $A_{BFM} = 0.01$, the mean estimated values for k_{BF} and k_{BM} are significantly different at two standard deviations, while values for k_{BCM}, α_{BCM} and m_{BCM} are not. This implies that at the field scale of the LPIT experiment there is greater heterogeneity in the hydrological properties of the basalt than of the B-C interbed.

9.3.6   Selenium (^{75}Se) Calibration Results

The six parameters identified for the hydrograph calibration were also used to perform a joint calibration on the hydrograph and ^{75}Se data for wells B04N11 and C04C11. The objective of this calibration effort was to determine whether parameters estimated using both flow and transport data are significantly different than those estimated using flow data alone.

Figure 9.3-8 shows joint hydrograph and ^{75}Se results for observation wells B04N11 and C04C11 using parameters estimated from the flow calibration (see Table 4, $A_{BFM} = 0.01$). Two numerical difficulties were identified during calibration that prevented completion of the iTOUGH2 calibration. First, iTOUGH2 with the EOS7r module did not provide a sufficiently robust flow simulation in comparison with the EOS9 module while simulating water ponding on the B-C interbed. Repeated failure of the Newton iteration caused an excessive number of timesteps, ultimately resulting in an accumulation of numerical mass-balance errors within the ^{75}Se mass conservation equation. This resulted in nonmonotonic behavior of the ^{75}Se mass-fraction curves (as shown on Figure 9.3-8a), making parameter estimation with iTOUGH2 impossible. These mass-accumulation errors are not evident in the water mass-conservation equation, as shown by Figure 9.3-8b.

Transport simulation results show that ^{75}Se mass fractions reached source values of 1×10^{-3}, which are fifteen times greater than peak values observed in the field for B04N11. The tail of the simulated ^{75}Se breakthrough declines much more rapidly than observed in the field. This discrepancy does not result from the omission of molecular diffusion between and within the fracture and matrix continua of the dual-permeability mesh, because upstream-weighting of the advective mass-fraction terms in the discretized mass-balance equations in iTOUGH2 will

introduce significantly more numerical dispersion than would be observed by molecular diffusion alone. Any numerical dispersion would be a product of the coarse grid discretization of the dual-permeability mesh, as well as the highly advective flow fields simulated during the infiltration tests. Given that the general shapes of the simulated breakthrough curves are incorrect, it is suggested that while the dual-permeability conceptual model can be used to simulate unsaturated flow, it may not adequately capture the physics of conservative transport in fractured basalt. Wu et al. (2001 [156399]) suggest that a triple-continuum conceptual model involving an interconnected matrix continuum, large-scale fracture continuum, and a small-scale fracture continuum may provide a better representation of transport. In this case, it is assumed that the small-scale fractures would retain sufficient ^{75}Se to retard its advection, decrease peak breakthrough values, and cause significant tailing of the breakthrough curves. Mass transfer of ^{75}Se from the large-scale fracture continuum into the small-scale fracture continuum would be primarily driven by molecular diffusion, which depends upon the concentration gradient of ^{75}Se (Liu et al. 2000 [154579]). Resolving the concentration gradient would require multiple interconnected nodes to represent the small-scale fracture continuum over a very fine (millimeter) scale. Although testing of the triple-continuum conceptual model would only require rebuilding a new mesh, successful calibration of this conceptual model in iTOUGH2 is contingent upon a more robust flow simulation and removal of the mass-accumulation errors seen in the radionuclide conservation equations.

9.3.7   Conclusions of LPIT Analogue Study

The study of UZ flow at the RWMC was chosen because INEEL is somewhat analogous to Yucca Mountain in hydrogeology. Average precipitation is similar at both sites, although infiltration is higher at INEEL. Perched water occurs in the UZ at both sites. Rock at both sites consists of a fractured porous media – basalt at INEEL and rhyolitic ash-flow tuff at Yucca Mountain. At both sites lateral flow plays a role in diverting flow, whereas the dominant flow paths are along fracture pathways. Fracture-filling minerals consist of clays and calcite at both sites. Although the two sites differ in significant ways (see Section 10.3.5), their similarities made it worthwhile to test modeling approaches of UZ flow (and also radionuclide transport in the UZ, as presented in Section 10) at Yucca Mountain with INEEL data.

Hydrographs of ponded water and ^{75}Se breakthrough curves measured during the LPIT test conducted at INEEL were analyzed to determine parameters controlling unsaturated flow and transport. Analysis of this data involved building a numerical model using iTOUGH2. The numerical model was constructed to conform to the lithological units at the LPIT site, which consisted of surficial clay-like sediments underlain by fractured basalt flows (the A, B, and C basalts) with a clay-like sedimentary interbed (B-C sediment layer) situated between the B and C basalts. The numerical model involved determining parameters controlling unsaturated and saturated flow and transport in fractured basalt, using a dual-permeability modeling approach that has been extensively employed to simulate flow and transport at Yucca Mountain.

Six parameters were identified to be most sensitive in controlling the calibration of the LPIT model to the observed hydrographs. These included the basalt fracture–matrix interfacial area, the basalt fracture and matrix continua permeabilities, the B-C interbed permeability, and van Genuchten capillary pressure α and m values. Simultaneous calibration to hydrographs B04N11, C04C11, B06N11, and C06C11 using iTOUGH2 yielded parameters that were consistent with

the range in values seen in data obtained from cores drilled near the LPIT site. Joint calibration to hydrograph and ^{75}Se data in wells B04N11 and C04C11 was unsuccessful because of numerical difficulties. Preliminary results indicated that while the dual-permeability conceptual model can be used to simulate unsaturated flow, it does not adequately simulate conservative transport in fractured basalt. This is because the matrix continuum needs to be significantly refined relative to the dual-permeability approach to resolve molecular diffusion caused by the concentration gradient between the fracture and matrix continua. This conclusion is especially significant to the site-scale Yucca Mountain model, in which, the dual-permeability approach is used extensively to simulate both unsaturated flow and transport in fractured tuff. The dual-permeability approach provides conservative estimates of peak concentrations and arrival times by underpredicting the mass transfer of conservative (i.e., nonsorbing) tracers from the fracture to the matrix continua.

Parameters estimated by the calibration are inherently spatially averaged over the region sampled by the downward-advecting infiltration front and laterally migrating ponded water. This region starts from directly beneath the infiltration pond and covers the radial area of the four hydrographs. These parameters were able to predict the control hydrograph that was located within the spatially averaged region, but were unable to predict hydrograph B08N11, located outside of this region. Independent calibration to hydrograph B08N11 indicated that the basalt properties showed significantly greater variability than the B-C interbed properties. This implies that the field-scale heterogeneity limits the volume to which the spatially averaged basalt parameters can be assigned relative to the B-C interbed parameters. This may in part result from the fractured–porous dual–continuum nature of the basalt in comparison to the porous single–continuum nature of the B-C interbed.

9.4   DRIFT SHADOW ANALOGUES

The phenomenon of flow diversion around a cavity was investigated for a general homogeneous porous medium by Philip et al. (1989 [105743]). The key feature of this phenomenon with respect to the transport of dissolved or colloidal material from the drift is that flow velocities in a zone beneath the drift are slower than unaffected flow velocities away from the drift (Figure 9.4-1). In particular, the flow velocity at the base of the drift is exactly zero. According to this conceptual model, the zone beneath the drift was also found to have lower water saturation than the undisturbed zone. This region of reduced flow velocity and water saturation beneath the drift is known as the drift shadow.

For a quasi-linear representation of the hydrogeologic properties, Philip et al. (1989 [105743], p. 18) found that the extent of the drift shadow is a function of a characteristic sorptive length scale and the drift radius. The shape of the drift shadow is governed by the ratio of the drift radius to the sorptive length scale. The ratio of the drift radius to the sorptive length scale is a measure of the relative importance of gravitational forces compared with the capillary forces that define flow patterns around the drift.

9.4.1 Caves

The drift shadow phenomenon cannot be accurately tested in the underground facility at Yucca Mountain because the natural system has been greatly perturbed by the heavy use of construction water for dust control and by the large volumes of air exhausted every day. Furthermore, the underground facility probably has not yet come to equilibrium with the undisturbed host rock. Complicating matters is the fact that detection of a drift shadow zone has never been documented for either natural or anthropogenic openings—conceivably ancient underground tombs and features could lie above a drift shadow zone. However, naturally occurring caves provide an opportunity to test for a drift shadow zone beneath an opening in the UZ. Limestone caves are hydrologically similar to the welded tuffs at Yucca Mountain because, in both cases, flow occurs primarily along fractures. Furthermore, caves have had sufficient time to establish hydrologic equilibrium. The Carlsbad, New Mexico, region is ideally suited for such a study because the large number of caves in the region allows for selection of a cave that closely matches the physical characteristics of a potential mined geologic repository. Caves that are known to receive direct surficial runoff should be eliminated from consideration. The cave chosen for study should be as large as or larger than proposed repository emplacement drift cross sections, currently approximately 5 m in diameter. The roof of the cave should be below the zone of surface influence, currently estimated as 6 m. Ideally, the cave should be readily accessible to light drilling equipment and should be sited so as to accommodate a small meteorological data station. The small cave approximately 800 m southeast of Boyd's Waterhole and northwest of Carlsbad, New Mexico (on the Azotea Peak 7½-minute topographic quadrangle map) appears to meet the necessary criteria.

The site should be amenable to standard tracer or infiltration tests. The infiltration tests would push the system out of hydrologic equilibrium by applying enough water to the surface above the cave to establish dripping into the cave. The tracers would be dyes or biodegradable tracers that would be used in an attempt to define flow paths.

9.4.2 Tunnels or Mine

Conceivably, an environmental tracer analysis could be used to demonstrate the presence of a drift shadow. An old mine in an arid region would be an ideal location, especially if its history dated back 100 years or so. Another possibility would be an old railroad tunnel or other tunnel, such as the Never-Sweat Tunnel (for ore haulage) at Apache Leap, Arizona, and the nearby mine. Chlorine-36 could be used as one possible example of an environmental tracer with a pulse input occurring ~50 years ago. If the mine drift is older than 50 years, it is possible that cores collected at present adjacent to the drift would contain the bomb-pulse signal, while cores collected below the drift would not. In a nearby, much younger drift, it would be expected that there would be essentially no difference in ^{36}Cl signal above and below the drift. Chlorine-36 is not the only possible tracer that could be used; the ideal tracer would be without background from the rock, such as an artificial environmental tracer.

9.5 CONCLUSIONS

Hydrographs of ponded water and ^{75}Se breakthrough curves measured during the LPIT test conducted at INEEL were analyzed to determine parameters controlling unsaturated flow and

transport. Analysis of this data involved building a numerical model using iTOUGH2 in a dual-permeability modeling approach, an approach that has been extensively used to simulate flow and transport at Yucca Mountain.

Six parameters were identified to be most sensitive in controlling the calibration of the LPIT model of unsaturated flow in fractured basalt. These included the basalt fracture–matrix interfacial area, the basalt fracture and matrix continua permeabilities, the B-C interbed permeability, and van Genuchten capillary pressure α and m values. Simultaneous calibration to hydrographs using iTOUGH2 yielded parameters that were consistent with the range in values seen in data obtained from cores drilled near the LPIT site. Preliminary results indicated that while the dual-permeability conceptual model can be used to simulate unsaturated flow, it may not adequately capture the physics of conservative transport in fractured basalt. This conclusion is relevant to the site-scale Yucca Mountain model, in which the dual-permeability approach is used extensively to simulate both unsaturated flow and transport in fractured tuff.

Parameters estimated by the calibration are inherently spatially averaged over the region sampled by the downward-advecting infiltration front and laterally migrating ponded water. The region starts from directly beneath the infiltration pond and covers the radial area of the four hydrographs. The basalt properties showed significantly greater variability than the B-C interbed properties. This implies that the field-scale heterogeneity limits the volume to which the spatially averaged basalt parameters can be attributed relative to the B-C interbed parameters. This may in part be due to the fractured-porous dual-continuum nature of the basalt in comparison to the porous single–continuum nature of the B-C interbed.

Finally, natural caves and man-made openings such as mines and tunnels may be suitable locations for testing the drift shadow concept, particularly if those sites have existed long enough to establish hydrologic equilibrium.

| Surficial Sediment |
| Clay Layer |
| A Basalt |
| A-B Sediment Layer |
| B Basalt |
| B-C Sediment Layer |
| C Basalt |
| C-D Sediment Layer |
| D Basalt |

Source: Simmons 2002 [157578], SN-LBNL-SCI-108-V2, p. 8

Figure 9.3-1.   Schematic Stratigraphic Sequence Illustrating the Relationship between Basalt Flows and Sediment Layers
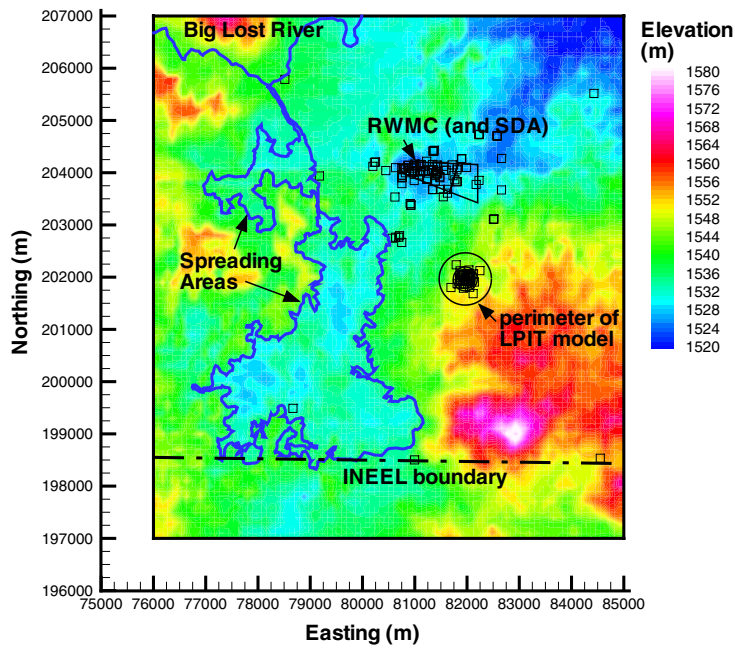
Source: Simmons 2002 [157578], SN-LBNL-SCI-186-V1, p. 58.

Figure 9.3-2.   Plan View of Regional Model with Contours of the Ground Surface Elevation
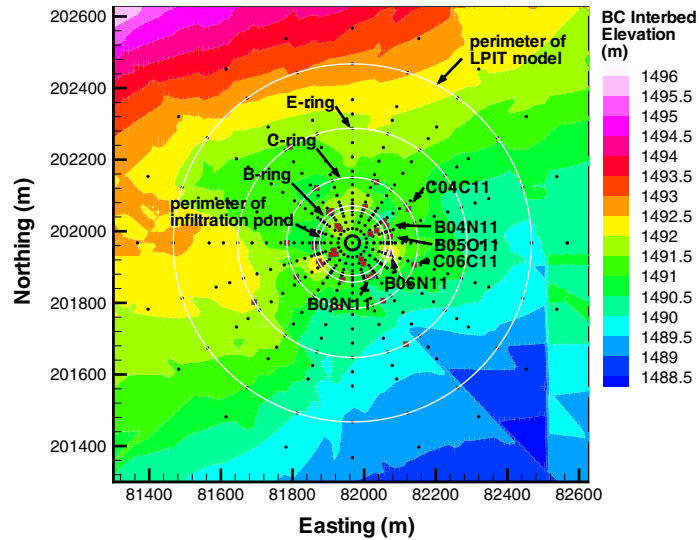
(a)
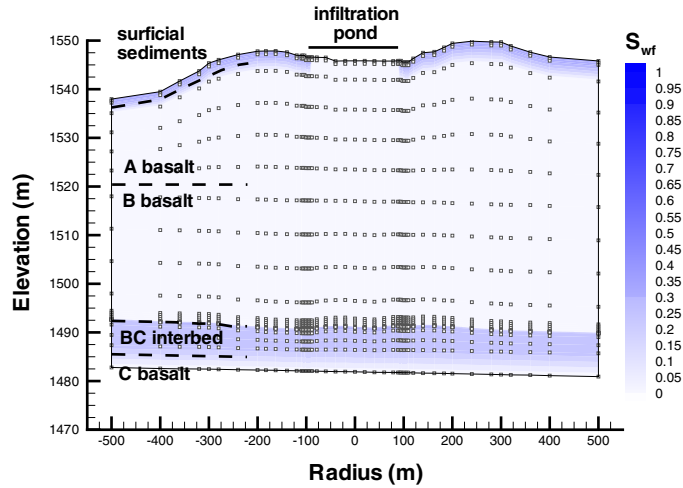
(b)

NOTE: In (a), the centroids of the elements are indicated as black dots and the wells by red dots

Source: Simmons 2002 [157578], SN-LBNL-SCI-186-V1, p. 59

Figure 9.3-3.   (a) Top of B-C Interbed Elevation with Centroids of Elements in Plan View As Well As the Location of All Hydrographs Used in this Analysis. (b) East-West Cross-Sectional View Showing the Steady-State Water Saturation in the Fracture Continuum
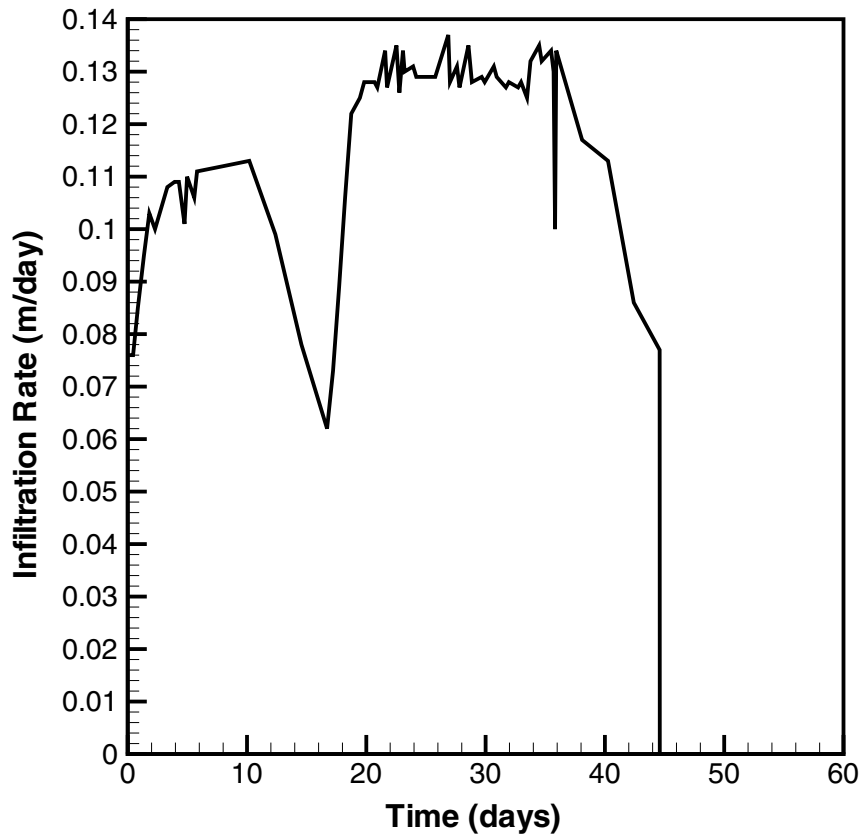
Source: Simmons 2002 [157578], SN-LBNL-SCI-186-V1, p. 60.

Figure 9.3-4.　Infiltration Rate Observed by Starr and Rohe (1995 [156400]) during the LPIT Using a Water Balance Analysis
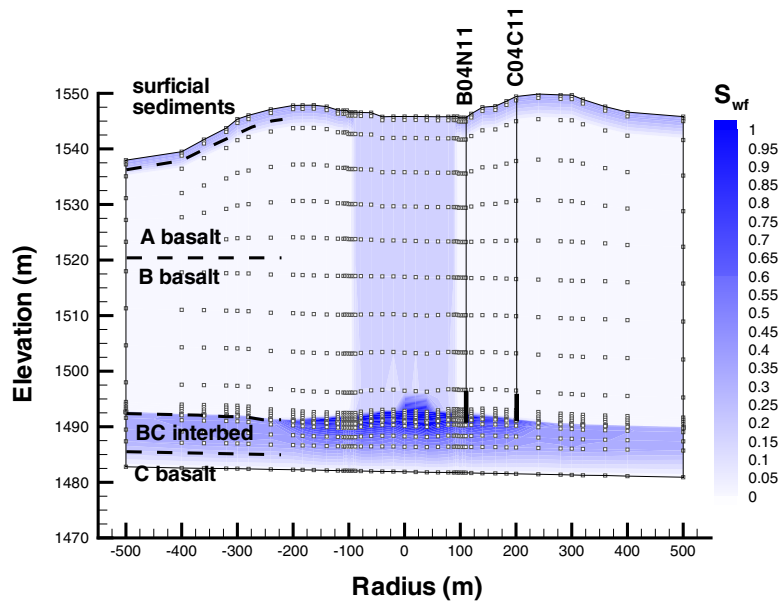
(a)
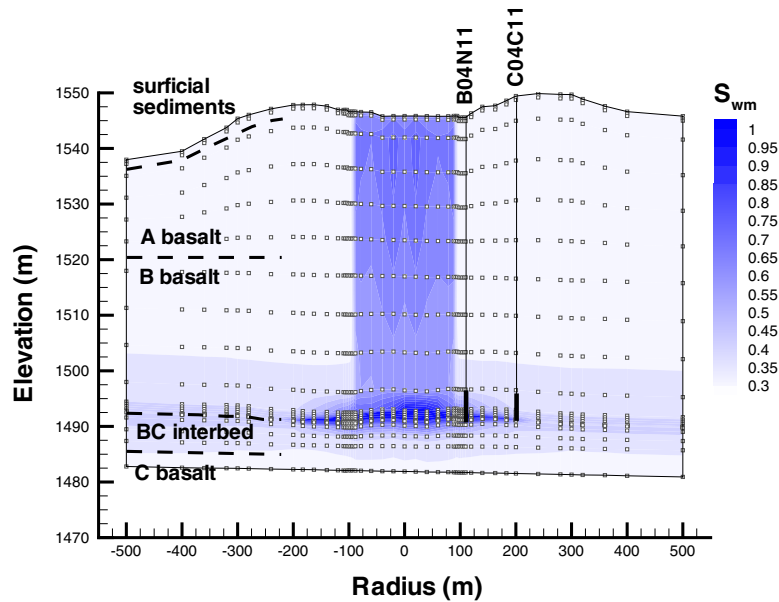
(b)

Source: Simmons 2002 [157578], SN-LBNL-SCI-186-V1, p. 61.

Figure 9.3-5.   Water Saturation in the (a) Fracture and (b) Matrix Continua at 35.5 Days after the Start of the LPIT
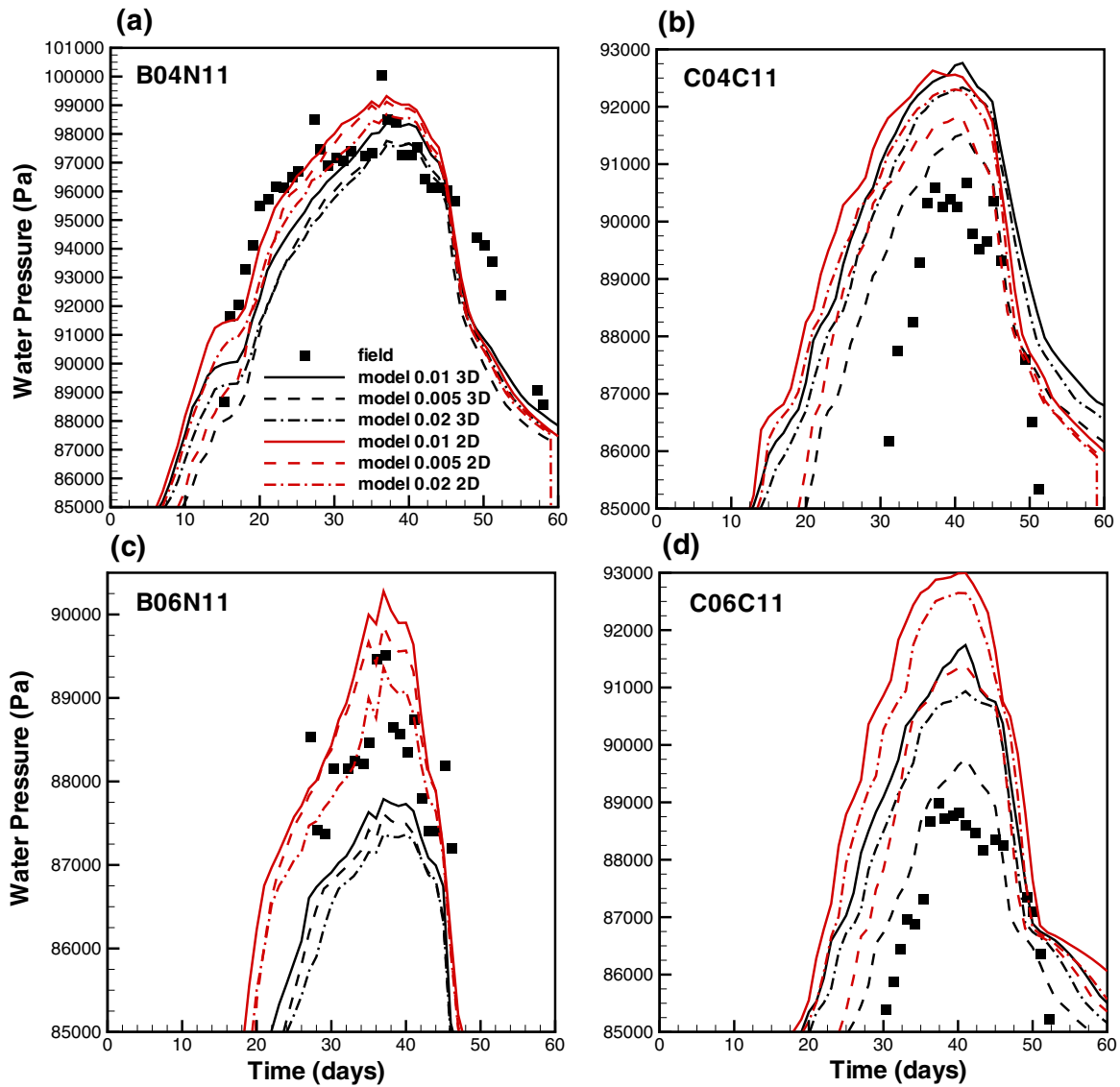
NOTE: Symbols represent field data with reference atmospheric gas phase pressure equal to 85 kPa. Lines represent calibration results using the 2–D submodel and the full 3–D LPIT model with varying A_{BFM} values (0.01, 0.005, 0.02).

Source: Simmons 2002 [157578], SN-LBNL-SCI-186-V1, p. 62.

Figure 9.3-6.   Ponded Water Hydrographs in Wells B04N11, C04C11, B06N11 and C06C11
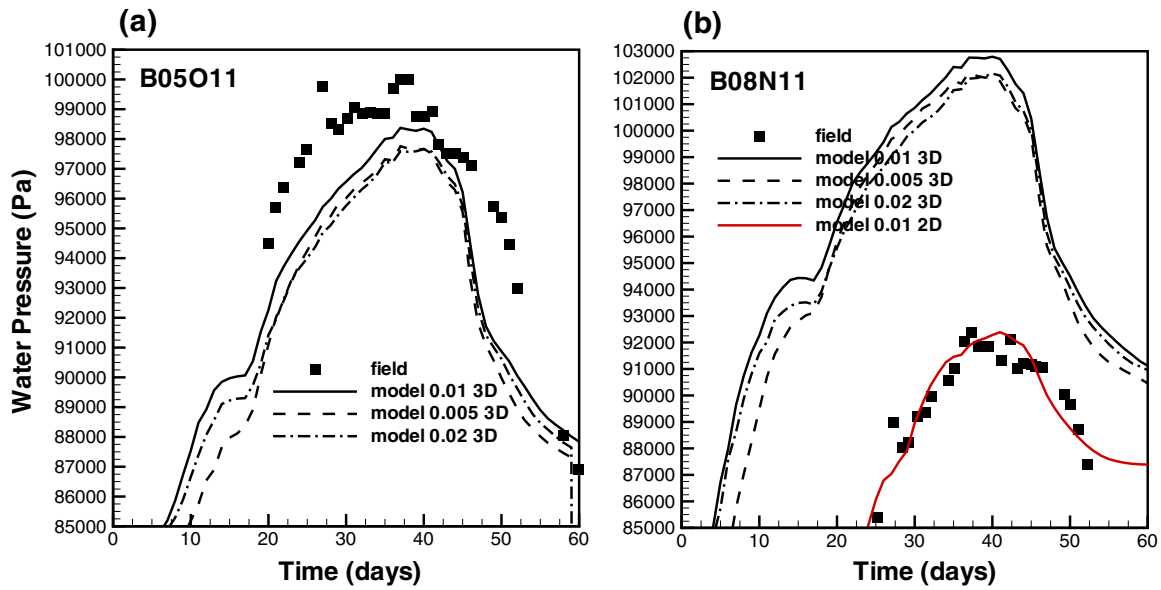
NOTE: Symbols represent hydrograph data while lines represent model results.

Source: Simmons 2002 [157578], SN-LBNL-SCI-186-V1, p. 63.

Figure 9.3-7. (a) Predictive Model Results for Control Hydrograph B05O11 and (b) Calibration Model Results for Hydrograph B08N11
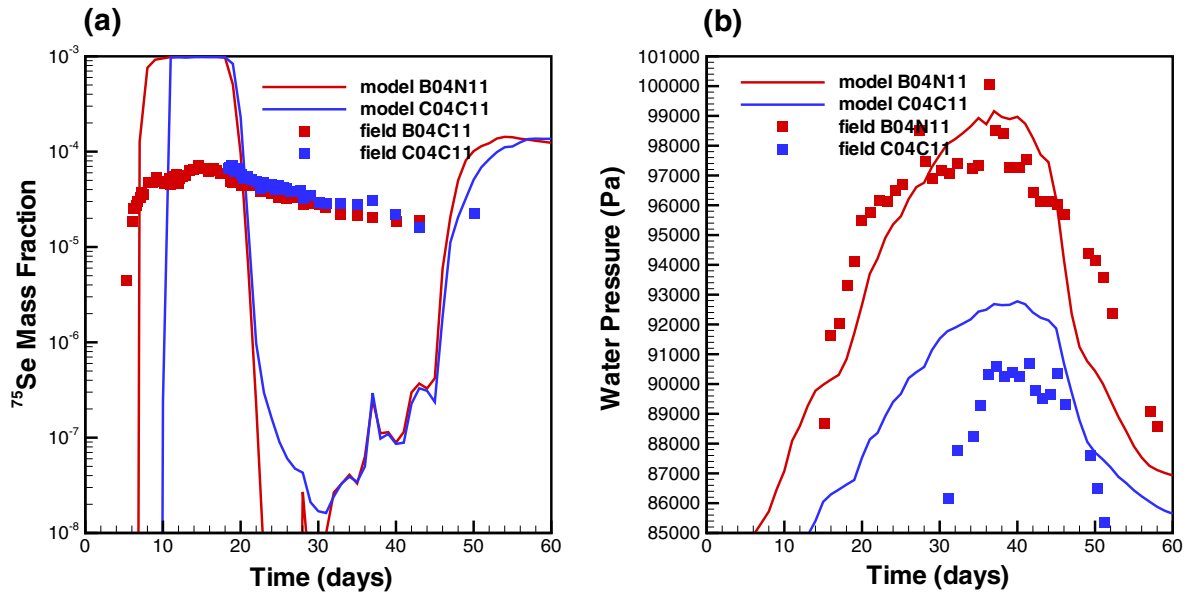
Source: Simmons 2002 [157578], SN-LBNL-SCI-186-V1, p. 63.

Figure 9.3-8. Joint (a) ^{75}Se Breakthrough and (b) Hydrograph Calibration Results for Wells B04N11 and C04C11
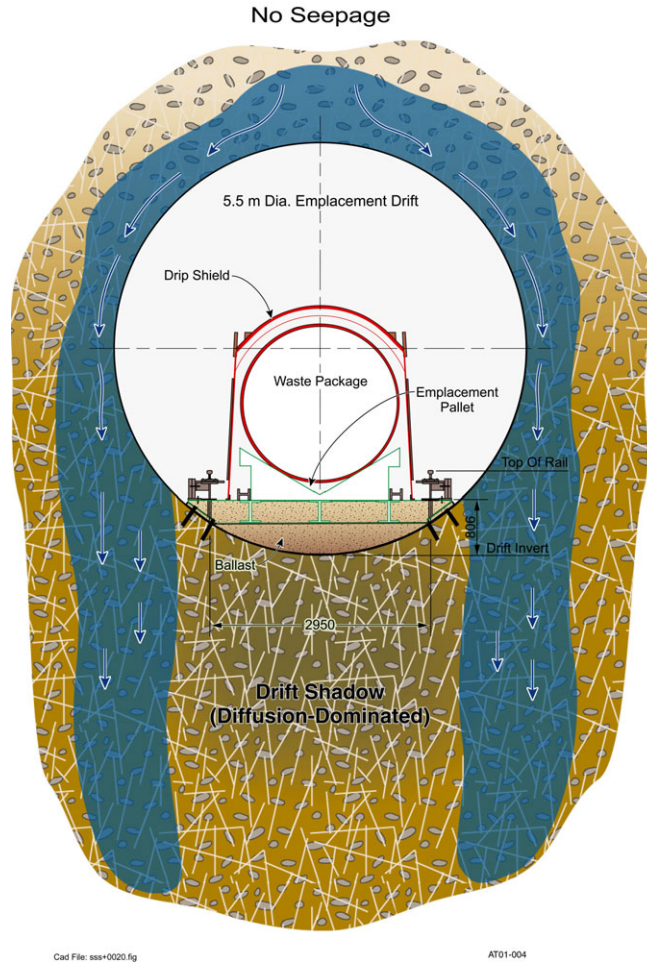
Source: DOE 2001 [153849], Figure 4-116.

Figure 9.4-1.   Schematic Diagram of Diffusion Barriers in Invert and Drift Shadow Zone

Table 9.3-1.   Distribution Coefficient (K_d) Values for Sorption of Contaminants on INEEL Sediments

Element	K_d Values (mL/g) and Range		
	Surficial Sediments	Interbeds	Basalt
Am	No data	450 (450 to 1,100)	70 (70 to 280)
Co	No data	1,148 (1,148 to 3,912)	11 (11 to 54)
Cs*	950 (589 to 1,253) (75 to 225)	2,228 (2,228 to 3,255)	39 (39 to 44)
Pu	7,800 (7,800 to 22,000)	5,100 (5,100 to 7,900)	70 (70 to 130)
Sr*	24 (23 to 26) (8.3 to 16.6) 50 (35 to 52)	42 (42 to 63) 155 (110 to 186)	6 (6 to 13) (1.1 to 2.7)
Tc	0	0	0
U	No data	3.4 (3.4 to 9)	0.2 (0.2 to 5.2)
Hg	972 (236 to 1,912)	176 (72 to 673)	(9.2 to 87)

NOTE: *Different K_d values for Cs and Sr are from different authors cited by Dicke (1997 [157410], Table 1).

Source: Dicke 1997 [157410], Table 1.

Table 9.3-2.   Basalt and B-C Interbed Parameters Collected by Laboratory Analysis of Core Samples

Property	Samples	Mean	Maximum	Minimum
k_{BM} [m^2]	43	†2.24×10^{-15}	9.48×10^{-14}	1×10^{-16}
ϕ_{BM} [−]	50	‡19.2	43.2	5.2
k_{BCM} [m^2]	15	†4.21×10^{-14}	6.86×10^{-12}	1.15×10^{-17}
ϕ_{BM} [−]	15	‡0.530	0.629	0.424
S_{wrBCM} [−]	15	‡0.183	0.376	0.038
α_{BCM} [Pa^{-1}]	15	†7.95×10^{-5}	5.025×10^{-4}	1.938×10^{-6}
m_{BCM} [−]	15	‡0.4	0.86	0.23

†geometric mean

‡arithmetic mean

Source: Simmons 2002 [157578], SN-LBNL-SCI-186-V1, p. 55.

Table 9.3-3.   Basalt and B-C Interbed Parameters Used in the LPIT Model

Parameter	Value		
	basalt fracture	basalt matrix	B-C interbed
$k_x = k_y = k_z$ [m^2]	From calibration	From calibration	From calibration
ϕ [–]	0.01	19.2	0.53
S_{wr} [–]	0.01	0.1	0.183
α [Pa^{-1}]	5×10^{-3}	5×10^{-4}	From calibration
m [–]	0.5	0.25	From calibration

Source: Simmons 2002 [157578], SN-LBNL-SCI-186-V1, p. 55.

Table 9.3-4.   Parameters Estimated during Calibration to Hydrographs B04N11, C04C11, B06N11 and C06C11

Param.	A_{BFM} = 0.01		A_{BFM} = 0.005		A_{BFM} = 0.02	
	Mean	std. dev.	Mean	std. dev.	Mean	Std. dev.
[†]k_{BF}	3.27×10^{-10}	0.0701	3.13×10^{-10}	0.0553	3.44×10^{-10}	0.0759
[†]k_{BM}	2.51×10^{-15}	0.395	6.31×10^{-15}	0.197	1×10^{-15}	0.381
[†]k_{BCM}	5.01×10^{-17}	1.51	6.31×10^{-17}	0.538	1.26×10^{-16}	0.848
[‡]α_{BCM}	1×10^{-4}	1.23	4.07×10^{-6}	0.465	1×10^{-4}	0.852
m_{BCM}	0.28	0.341	0.86	0.718	0.67	1.08

[†]mean permeability values are in [m^2] while standard deviation is in [log$_{10}$ m^2]

[‡]mean α_{BCM} values are in [Pa^{-1}] while standard deviation is in [log$_{10}$ Pa^{-1}]

Source: Simmons 2002 [157578], SN-LBNL-SCI-186-V1, p. 56.

Table 9.3-5.   Parameters Estimated during Calibration to Hydrograph B08N11

Parameter	Mean	std. dev.
k_{BF}	7.05×10^{-10} [m^2]	0.0553 [log$_{10}$ m^2]
k_{BM}	7.94×10^{-14} [m^2]	0.162 [log$_{10}$ m^2]
k_{BCM}	2.51×10^{-16} [m^2]	0.342 [log$_{10}$ m^2]
α_{BCM}	6.31×10^{-5} [Pa^{-1}]	0.690 [log$_{10}$ Pa^{-1}]
m_{BCM}	0.48	0.527

Source: Simmons 2002 [157578], SN-LBNL-SCI-186-V1, p. 56.

10. ANALOGUES TO UNSATURATED ZONE TRANSPORT

10.1 INTRODUCTION

This section presents updates on two recent studies examining transport of radionuclides in unsaturated zone (UZ) conditions. The first is a study of migration of radionuclides at the Idaho National Engineering and Environmental Laboratory (INEEL) with the objective of explaining mechanisms responsible for detection of concentrations of neptunium and uranium in monitoring wells below the water table. The second study presents results of analyses and modeling of uranium systematics at Peña Blanca, Mexico, based on water sampling campaigns in 2000 and 2001. Additional insights derived from natural analogues in Steenkampskraal, South Africa, and Koongarra, Australia, on the significance of colloid transport in the UZ are also presented.

Previous studies have indicated that fractures act as both transport pathways and places of retardation at a number of the analogue sites. This was shown in *Yucca Mountain Site Description* (CRWMS M&O 2000 [151945], Section 13) through analogues from Peña Blanca, Mexico; Akrotiri, Greece; and volcanic tuff-hosted uranium deposits in northern Nevada. At Nopal I (Peña Blanca), uranium has been transported relatively small distances, essentially completely along fractures, and has been sorbed or precipitated onto fracture-coating Fe-oxides and calcites. Colloidal transport of uranium was shown to be minimal at another analogue site in Koongarra, Australia, where filtration of colloids appears to be effective. The YMP total system performance assessment (TSPA) assumes no colloid filtration, an assumption that may be unnecessarily conservative. Data available for the *Yucca Mountain Site Description* also indicated that the geochemical system at Nopal I restricted actinide mobility in the UZ and that by analogy the tuffs at Yucca Mountain should have similar retentive properties and impede the mobility of oxidized uranium. Additionally, clays found in fractures and vitrophyres at Yucca Mountain may also be effective in retarding migration of radionuclides. This conclusion can be drawn from examination of the clay haloes (5–30 cm thick) surrounding ore deposits at Oklo, Gabon, and Cigar Lake, Canada, which have been shown to be effective in retarding the migration of uranium away from the source (CRWMS M&O 2000 [151945], Section 13.5).

Radionuclide migration experiments under unsaturated conditions have also been completed in a 30 cm block of Calico Hills nonwelded tuff from the Busted Butte test facility near Yucca Mountain. This type of study could be thought of as a self-analogue to migration in the Calico Hills nonwelded unit under Yucca Mountain. Elution profiles showed that relative to an ideal conservative tracer (tritiated water), transport of TcO_4^- was approximately 15% faster, but that NpO_2^+ was retarded by a factor of 3 (Vandergraaf et al. 2001 [155042]). These findings fall within the range of retardation coefficients determined from tuff column experiments (Triay et al. 1996 [101024], Appendix A). Retardation of ^{22}Na, ^{60}Co, and ^{137}Cs was higher than for neptunium in the Calico Hills block experiments, and this agreed qualitatively with experimentally determined batch sorption coefficients for these isotopes (BSC 2001 [155950], p. 11-46). The analogues discussed in this section focus primarily on processes occurring at INEEL and Peña Blanca as potential analogues for radionuclide transport in the UZ at Yucca Mountain. Information found in Sections 10.3, 10.4, and 10.5 may help to support arguments associated with Key Technical Issue (KTI) KUZ0407 listed in Table 1-1.

10.2 TRANSPORT IN THE UZ AT YUCCA MOUNTAIN

The evaluation of possible radionuclide transport from the potential repository to the groundwater in the saturated zone (SZ) is key to assessing the performance of the potential repository. In the event of such waste mobilization and migration away from the potential emplacement drifts at Yucca Mountain, the rate of radionuclide transport through the UZ is determined by the percolation flux and by the hydrologic properties and sorptive properties of the tuff units. Water carrying radionuclides may percolate vertically through fractured tuff units, or it may be laterally diverted around low-permeability horizons (particularly where perched water occurs) to fault zones. Diffusion, sorption, and dispersion processes would retard the movement of radionuclides. Each of these processes potentially affects the distribution and concentration of radionuclide particles at the water table.

The transport of aqueous and colloidal radionuclide species can occur in both fracture and matrix continua, with exchange between continua (fracture-matrix interaction) resulting from advective and/or diffusive processes, as well as sorption in the matrix. The flow pathways are determined by the characteristics of hydrogeologic units, faults, and perched water.

These characteristics control the extent of downward versus lateral flow, fracture-matrix interaction, and the partitioning of flow between fractures and the rock matrix. Fractures and faults can be fast flow paths, with diffusion into the matrix and sorption to the rock being the important processes for radionuclide retardation.

The concentration of radionuclides and their daughter products are diminished according to their radioactive decay rates, the extent of sorption onto the solid phase, and dilution as a result of mixing and dispersion. The effects of advective flow processes, sorption of solutes or filtration of colloids, matrix diffusion, hydrodynamic dispersion, and radioactive decay are important factors that play varying roles of significance in slowing the movement of radionuclides through the UZ.

10.3 INEEL AS A POTENTIAL ANALOGUE FOR RADIONUCLIDE TRANSPORT AT YUCCA MOUNTAIN

10.3.1   Background

Section 10.3 presents a preliminary hydrologic and geochemical transport model for americium (Am), cesium (Cs), neptunium (Np), plutonium (Pu), strontium (Sr), and uranium (U) in the UZ beneath the Subsurface Disposal Area (SDA) of the RWMC at INEEL. The geologic, hydrologic, and geochemical bases for the model were summarized in Section 9.3. Section 10.3 uses these bases to develop a conceptual model of flow and transport beneath the SDA. A series of numerical models have been developed that test various aspects of the conceptual model. The computer codes FLOTRAN and FEHM were used to develop models for flow and radionuclide movement in the surficial sediments in and beneath the waste pits. Measurements of radionuclide concentrations made during the drilling of shallow monitoring holes in and near the waste trenches (Humphrey and Tingey 1978 [157491]; Rightmire and Lewis 1988 [156442]) provide a basis for evaluating the model. Flow and radionuclide transport in the UZ beneath the SDA is simulated, and the results are compared to available field data.

10.3.2 Column Experiments

10.3.2.1 Description of Experiment

Column experiments and associated batch tests to measure values of the equilibrium distribution coefficients (K_d) and the reaction-rate coefficients for the sorption of americium-241 (^{241}Am), cesium-137 (^{137}Cs), cobalt-60 (^{60}Co), strontium-90 (^{90}Sr), uranium-233 (^{233}U), and plutonium-239 (^{239}Pu) were carried out at Clemson University and INEEL (Newman 1996 [156434]). The experiments included columns of crushed basalt (> 0.25 mm size fraction), mixed interbed sediments (< 0.25 mm size fraction), and intact basalt cores taken from the same boulder that provided the crushed basalt. In the first phase of the experiments, the steady, saturated flow of synthetic water with a composition (Table 10.3-1, Section 10.3.5.2) similar to groundwater at INEEL was established in the columns. A spiked solution containing tritium (^{3}H) and one or more of the radionuclides of interest was input with the synthetic water for a duration equivalent to about one pore volume and then was flushed with about 200 pore volumes of the unspiked synthetic water. The breakthrough curves of tritium (^{3}H) were fit with the advection-dispersion equation, as implemented in the computer code CXTFIT (Parker and van Genuchten 1984 [126526]), to demonstrate the absence of preferential flow during the experiments and estimate dispersion coefficients for the material in the columns (Newman 1996 [156434], Appendix E). CXTFIT also was used to fit the advection-dispersion equation to the breakthrough curves for each of the radionuclides. These fits provided estimates for the retardation coefficient R_t:

$$R_t = (1 + \frac{\rho_b K_d}{\phi})$$ (Eq. 10-1)

where ρ_b is bulk density (g/cm^3) and ϕ is porosity. The K_d values for each combination of radionuclide and column material were then calculated from fitted R values. CXTFIT also includes a variation of the equilibrium advection-dispersion model known as the two-site/two-region model that accounts either for (1) the presence of both equilibrium and nonequilibrium sorption sites or (2) the presence of mobile and immobile water. The advection-dispersion model and the two-site/two-region model were fitted to the radionuclide breakthrough curves, as appropriate, to estimate R and parameters that account for the transfer of radionuclides between the mobile and immobile water.

10.3.2.2 Results of Experiments

Results for the columns containing crushed basalt (Newman 1996 [156434], Table 6, Appendix F) showed that most of the radionuclide mass (except for ^{233}U) was substantially retarded compared to the water. Recovery of the input radionuclide mass was less than 100% for ^{60}Co (~69%), ^{90}Sr (~50%), ^{239}Pu (~33%), and ^{231}Am (~10%), indicating that the unrecovered fraction had a retardation factor greater than 200 (Newman 1996 [156434], p. 28). Two-site/two-region models fit to the breakthrough curves of ^{90}Sr, ^{137}Cs, and ^{233}U generally resulted in better fits to the data than the equilibrium advection-dispersion model; recovery was insufficient to apply the two-site/two-region model to the remaining radionuclides. A fraction of the ^{60}Co (~3%), ^{241}Am (9 to 13%), and ^{239}Pu (10 to 55%) in the column studies exhibited early breakthrough compared with most of the mass of these radionuclides. Fits of the equilibrium advection-dispersion

equation to the breakthrough curves for this so-called enhanced mobility fraction resulted in retardation factors of between 1.5 and 2 (Newman 1996 [156434], Table 6). Possible explanations for the existence of the enhanced mobility fraction included (1) the sorption and transport of these radionuclides on colloids such as SiO_2, (2) the formation of neutral or negatively charged complexes involving these radionuclides and carbonate, and (3) kinetically limited sorption. Related experiments demonstrated that the enhanced mobility fraction of ^{239}Pu increased with total alkalinity and the mobile fraction of ^{241}Am increased with flow rate (Newman 1996 [156434], Figures 15 and 16). However, no definite conclusions regarding the specific causes for the enhanced mobility fraction were made. Batch studies done to evaluate the equilibration time between various radionuclides and crushed basalt showed that the equilibration time for ^{60}Co was not longer than radionuclides lacking an enhanced mobility fraction (such as ^{90}Sr and ^{137}Cs) (Newman et al. 1996 [156434], Table 8). The data from the batch tests for ^{241}Am indicated equilibrium behavior, and data for ^{239}Pu were not reported.

Results from column studies of the interbed material (Newman 1996 [156434], Table 7, Appendix F) indicated much higher sorption of all radionuclides in the interbed material compared to the crushed basalt. The percent recovery for ^{233}U was over 90% but less than 4% for all other radionuclides. Although their retardation factors must be over 200, which is the number of eluted pore volumes following introduction of the spiked solution, exact retardation factors could not be calculated for radionuclides other than ^{233}U. In spite of the large retardation of most of the mass, a small (< 1%), highly mobile fraction of ^{60}Co, ^{241}Am, and ^{239}Pu was observed to break through within the first five displaced pore volumes (Newman 1996 [156434], Section 3.1.2, Figures 11, F-10 to F-13, and F-17 to F-19).

Other experiments conducted as part of the Clemson University and INEEL studies demonstrated that:

(1) 10 to 90% of the water in the intact basalt cores may be immobile, based on the fit of the two-site/two-region model to breakthrough curves of bromide (Newman 1996 [156434], Table 14);

(2) K_d values for ^{90}Sr estimated from column studies of crushed basalt were similar under saturated and unsaturated conditions (Newman 1996 [156434], pp. 68–69); and

(3) K_d values for ^{237}Cs, ^{60}Co, ^{90}Sr, and ^{233}U estimated from batch experiments and column experiments were generally similar, suggesting the applicability of Kd values measured from batch tests to field conditions with much different sediment/water ratios (Newman 1996 [156434], p. 62, Table 13).

10.3.3   Distribution of Radionuclides beneath the Surficial Sediments at the SDA

Several radionuclides, including ^{238}Pu, ^{239,240}Pu, ^{241}Am, ^{60}Co, ^{137}Cs, and ^{90}Sr, have been found sorbed to rocks and interbed sediments beneath the surficial sediments at the SDA. The locations where radionuclide activities were at least three times greater than the detection limits are noted on maps showing the locations of all deep wells in Figure 10.3-1. These maps are based on a recent data compilation by the USGS (2000 [157415], Tables 3-10a, b, and c), which itself is based on earlier work by Dames and Moore (1992 [157409]). Each map shows the radionuclides

present in different depth intervals, each of which contains either the 9 m, 34 m, or 73 m interbed (see Section 9.3.1.1). Note that not all of the wells shown in Figure 10.3-1 have been sampled, so that well locations with no indicated radionuclides are a mixture of true nondetections and unsampled wells.

The maps in Figure 10.3-1 locally have some lateral and vertical consistency with regard to radionuclide distributions. For instance, closely spaced wells DO-2, 79-2, and TW-1 contain ^{238}Pu, ^{239,240}Pu, and ^{241}Am at multiple depth intervals. Similarly, well 93 contains ^{241}Am and ^{90}Sr at two different depth intervals (Figures 10.3-2a and 10.3-2b). Elsewhere, however, different radionuclides are present at different depths in a given borehole or different radionuclides are present at the same depths in nearby boreholes, making simple interpretations of these radionuclide distributions difficult. The erratic distribution of these radionuclides may be related to complex flow and transport behavior, including preferential and lateral flow, or to cross contamination during drilling (USGS 2000 [157415]).

Because a complete list of sample locations is not available, it is not known whether the absence of radionuclide detections in Figure 10.3-1 reflects the true absence of radionuclides or simply the absence of samples from those locations. Therefore, although it can be stated confidently that radionuclides are present in the deep subsurface of the SDA, the exact distribution of these radionuclides is uncertain. Qualitatively, however, it is possible to anticipate some of the factors that would be expected to influence the distribution of sorbed radionuclide activities in the subsurface, even if these factors are poorly characterized at present. These factors are (1) the distribution and strength of contaminant sources within the SDA; (2) the distribution of infiltration within the SDA; (3) heterogeneity in fracture properties within the basalt layers; (4) the sorptive properties of the rocks and sediments themselves; (5) the thicknesses of the surficial sediment and sedimentary interbeds; and (6) the orientations of rock/sediment interfaces.

The distribution and strength of the radionuclide sources within the SDA are the subjects of ongoing study at INEEL, and it is likely to be an important control on the observed radionuclide distribution, based on models of nonradiological contaminants at the SDA (Magnuson and Sondrup 1998 [156431]). The models indicated that the observed distribution of these nonradiological contaminants was at least as sensitive to uncertainty in source-term strength as to uncertainty in hydrologic parameters, and a similar sensitivity to source strength could reasonably be expected for the radioactive contaminants as well.

Temporally averaged infiltration rates have been estimated within the SDA (Magnuson and Sondrup 1998 [156431]), based on a study by Martian (1995 [156432]) that used neutron probe moisture logs from 17 boreholes within the SDA and historic data on the nature of the spring thaw to calibrate surficial sediment properties and estimate time-varying drainage from the surficial sediments into the underlying basalts over a 42 yr period. Although there is uncertainty associated with these estimates, the analyses that generated the estimates were as complete as can be expected, and it is unlikely that future analyses will be able to reduce this uncertainty.

Heterogeneities within individual basalt flows are known to exist (Knutson et al. 1990 [107839]) and indicate that the brecciated upper and lower margins may be the most porous and permeable parts of the basalt flows. This conceptual model has suggested to some (Rightmire and Lewis 1987 [156441]) that the basalt permeability is highly anisotropic, with higher permeability in the

subhorizontal direction. Beyond this general conceptual model, however, very little is known about the details of the permeability distribution in the basalts beneath the SDA. It is unlikely that the permeability variations resulting from fractures in the basalts would ever be known in sufficient detail to be able to explain the contaminant distribution, if indeed these permeability variations are the controlling factor.

The thickness of the surficial sediments and the sedimentary interbeds is a possible control on the distribution of radionuclides, because flow through the sediments is through the porous matrix rather than the fractures and the sediments have a much higher porosity and water content than the basalts. Therefore, assuming that flow is primarily vertical, effective porosity between the land surface and any depth largely depends on the thickness of the sediments within that depth interval. Radionuclide migration is expected to be most rapid where the surficial sediments and sedimentary interbeds are thin or absent.

If contrasts in the hydrologic properties of rocks and sediments beneath the SDA cause water to flow laterally along the interfaces between these layers, the orientation of these interfaces may indicate the areas toward which water and contaminants are moving. Lateral flow is possible both when the vertical flux greatly exceeds the vertical hydraulic conductivity of the least permeable layers, and at lower fluxes, when capillary barriers delay or prevent the entry of water moving through fine-grained layers into underlying coarse-grained layers (Montazer and Wilson 1984 [100161]). As discussed below, contour maps of these interfaces exist and can be used to infer flow directions if lateral flow along these interfaces were to occur.

Of all the factors cited above that are likely to influence radionuclide transport at the SDA, perhaps the best known are the thickness and orientations of the major hydrostratigraphic units. Contour maps of the thickness of the sedimentary units and the orientations of the upper surfaces of each hydrostratigraphic layer, including the basalt groups, were created using SURFER (V. 7.0) and data from Magnuson and Sondrup (1998 [156431], Table 2-1) as shown in Figures 10.3-2 to 10.3-11. Unfortunately, the possible relation between the radionuclide distributions shown in Figure 10.3-1 and the layer thicknesses and orientations shown in Figures 10.3-2 to 10.3-11 have been difficult to identify because of uncertainty in the actual extent of the contamination and in other factors likely to influence transport.

10.3.4 Perched Water

The distribution of perched water within the SDA was examined to determine if it could provide some indication of flow paths and evidence for the possible stratigraphic and topographic controls on its occurrence. Perched water has been observed at many locations within the SDA along the surficial sediment/basalt interface, where seasonal water levels have been monitored in several wells and boreholes (Hubbell 1993 [157412], p. 2-6; 1995 [157413], p. 2). Hydrographs of this shallow perched water showed strong seasonal effects, with the highest perched water levels occurring after the spring snow melt. Perched water at the surficial sediment/basalt interface has been found in topographically low areas (MS-03, MS-04, pit 9 wells 1, 2, 3, and 6, and possibly W-06 and NAT-06; see Hubbell 1993 [157412], Figure 1; 1995 [157413], Figure 1 for well locations), but higher elevation areas were not monitored, so the role of topography is unclear. Perched water at the surficial-sediment/basalt interface has also been found in structurally low areas at the surficial sediment/basalt contact (Acid pit well 4 and NAT-16).

However, most of SDA is in a structurally low area along surficial sediment/basalt contact (Figure 10.3-4), so the SDA as a whole may be receiving subsurface lateral flow from the adjacent areas.

Deep perched water has been found consistently in a number of wells within the SDA (Hubbell 1993 [157412]; 1995 [157413]). The wells that contain perched water, the average depth to the top of the perched water, and the perched water elevations are shown in Figure 10.3-12. Wells in which perched water is found at or above the B-C interbed are listed in blue, whereas wells with deeper perched water are listed in red. A comparison of perched water locations shown in Figure 10.3-12 with the contour maps shown in Figures 10.3-2 to 10.3-11 indicates the following: (1) wells D-10, 92, 93-02D, and 8802D are in topographically low areas (Figure 10.3-2); (2) wells 92, 93-02D, and 78-1 are at structurally low areas in the surface of the uppermost (A) basalt (Figure 10.3-4); (3) wells with perched water at the B-C interbed (77-2 and 78-1) are at locations where the A-B interbed is absent (Figure 10.3-5); (4) only well 93-02D is at a structurally low point in the top of the B-C interbed (Figure 10.3-8); and (5) only well 93-02D is at a structurally low point in the top of the C-D interbed. These observations, summarized in Figure 10.3-12, suggest that the topography, the orientation of the surficial sediment/basalt interface, and, possibly, the absence of the A-B interbed may determine where perched water is found at the SDA.

10.3.5 On the Use of INEEL as a Potential Analogue for Radionuclide Transport at Yucca Mountain

The following sections discuss the similarities and differences between various facets of the hydrogeology and geochemistry at Yucca Mountain and the SDA of INEEL. The motivation for this comparison is to evaluate the potential use of the SDA as an analogue for radionuclide migration from a potential repository at Yucca Mountain through the UZ at some time in the distant future.

10.3.5.1 Comparison of Hydrogeologic Settings

There are several similarities in the general hydrogeologic settings that recommend the use of the SDA as an analogue for Yucca Mountain. First, both sites are presently relatively arid. Average annual precipitation is approximately 200 mm/yr at INEEL (Rawson et al. 1991 [156439], p. 478) and 190 mm/yr at Yucca Mountain (DOE 2001 [153849], Table 4.11). The relatively low precipitation rates and high evaporative demand result in estimated net infiltration rates of approximately 10 mm/yr for undisturbed soils near the SDA (Cecil et al. 1992 [156256], p. 711), whereas steady-state deep infiltration rates at Yucca Mountain are estimated to be between 1 and 12 mm/yr (Flint et al. 2002 [157411]), averaging 4.6 mm/yr (DOE 2001 [153849], Table 4.11), depending on the local topographic setting.

The second similarity exists in the hydrostratigraphic settings of the sites and their anticipated effect on water movement through fractures. In the UZ at INEEL, fractured basalts alternate with relatively thin, unconsolidated sedimentary layers (Rightmire and Lewis 1987 [156441]). At Yucca Mountain, relatively unfractured, nonwelded tuffs alternate with fractured, welded tuffs (Scott et al. 1983 [101156]). At both sites, water is expected to move from fractures into the porous matrix and back into fractures as it percolates downward through the fractured layers,

into the unconsolidated sedimentary material or nonwelded tuffs, and back into fractured layers (Montazer and Wilson 1984 [100161]; USGS 2000 [157415]). The details of water movement across the boundaries between these layers may have implications for the formation of perched water, lateral flow, fingering through the porous material, and flow focusing in fractures underlying the porous layers.

The third similarity is the presence of perched water at both sites, some of which may have migrated laterally beneath the present or proposed waste-disposal areas from adjacent areas. Perched water beneath the SDA may have resulted from the diversion of water from the Big Lost River during periods of high flow into spreading areas located 1 to 2 km southwest of the SDA (Rightmire and Lewis 1987 [156441], pp. 40–41, 60–65). At Yucca Mountain, perched water beneath the northern part of the proposed repository area may have originated, in part, from water that had infiltrated in the northern part of Yucca Mountain and moved southward along low-permeability layers at depth (Wu et al. 1999 [117167], pp. 163, 176). At both sites, an understanding of the source and cause of the perched water is important for what it may imply about the magnitude of recharge at the disposal areas and for predicting the pathways that waste may take to the SZ.

Finally, both sites have potential flow-focusing mechanisms. According to one possible conceptual model (USGS 2000 [157415], pp. 2.8–2.10), perched water flowing laterally above or through the sedimentary interbeds at the SDA may be funneled into areas where the interbeds are absent, resulting in the accelerated movement of water and waste compared to areas where the interbeds are present. Additionally, there is the potential for water in the interbeds to flow toward low points along the irregular lower contacts between the sedimentary interbeds and underlying basalts, thereby focusing flow into the basalts in these areas. At Yucca Mountain, lateral flow along stratigraphic contacts may divert water laterally until it is redirected downward by faults or by other discontinuities in the interface between the diverting layers (Montazer and Wilson 1984 [100161], pp. 47–52). Additionally, fault zones mapped at the surface narrow with depth through the PTn (Day et al. 1998 [101557], Plate 2), a factor that could tend to focus water flow through the PTn. In the deep subsurface at Yucca Mountain, most recharge may reach the water table along faults or by moving laterally along perched layers (Flint et al. 2002 [157411]). Both potential recharge mechanisms at Yucca Mountain would tend to concentrate flow and mix water that has flowed through different areas.

Certain dissimilarities that exist between the hydrogeologic settings at the SDA and Yucca Mountain must be taken into account when radionuclide migration in the UZ at the SDA is used as an analogue for how radionuclides could migrate in the UZ at Yucca Mountain. First, in spite of the similarity in precipitation rates and long-term recharge rates of the sites, recharge rates at the SDA site have increased considerably since the SDA was constructed. The drifting of snow within the SDA and its melting during subsequent spring thaws are estimated to cause a net infiltration at the SDA of between 60 and 100 mm/yr, with an estimated long-term spatial average of 85 mm/yr (Martian 1995 [156432], pp. 31–36). Additionally, the SDA has been flooded three times because of the collection of surface runoff in the topographically low areas formed, in part, by the compaction of backfill in the waste pits and trenches. The three flood events of 1962, 1969, and 1982 are estimated to have resulted in the infiltration of 365 mm of water, or the equivalent of about 36 yr of natural infiltration, over the site (Magnuson and Sondrup 1998 [156431], Table 2-3). Thus, a great deal more water has actually been available to

mobilize waste at the SDA than is estimated to be available at Yucca Mountain under present climate conditions or at the SDA under undisturbed conditions.

A second dissimilarity between the two sites is in the fracture patterns in the basalts at the SDA and the welded tuffs at Yucca Mountain. At the SDA, fracture densities are greatest along the brecciated margins and least in the dense interiors of the individual basalt flows (Knutson et al. 1990 [107839], p. 119; Rightmire and Lewis 1987 [156441], p. 41), suggesting that horizontal permeability may be much larger than the vertical permeability in the basalts. Anisotropy of this type in the basalts, like the presence of the sedimentary interbeds, would enhance lateral flow in the UZ. At Yucca Mountain, the generally steep dips of fractures in the Topopah Spring Tuff are likely to favor a high vertical to horizontal permeability ratio in that unit, a hypothesis supported by air-injection and pneumatic pressure-wave analysis (Rousseau et al. 1999 [102097], p. 76). High vertical to horizontal anisotropy in the Topopah Spring Tuff would tend to promote more vertical drainage than might be expected at INEEL. However, beneath the densely welded part of the Topopah Spring Tuff, welding changes and stratified mineral alteration zones also effectively create a high horizontal-to-vertical permeability ratio in the deeper units, so conditions at Yucca Mountain become more similar to those at the INEEL site at depth.

A third distinction between the hydrogeologic settings at Yucca Mountain and INEEL is that fractures in the basalts are often filled with sediments, including authigenic calcite and clay, and detrital clay, silt, and sand that probably washed into the fractures when individual flows were exposed at the land surface (Rightmire and Lewis 1987 [156441], pp. 22–24). Besides providing additional surface area for radionuclide sorption within fractures, the presence of sediment in the fractures at INEEL reduces the likelihood of sheet or film flow within the fractures. Sheet and film flow could be inferred to take place in some fractures at Yucca Mountain, based on the observation that mineral coatings have been deposited preferentially on the footwall of dipping fractures (Paces et al. 1998 [107408], p. 37)

10.3.5.2   Comparison of Geochemical Settings

This section compares the overall geochemical settings of Yucca Mountain and the SDA at INEEL, including mineralogy and water and gas compositions.

The rocks beneath the SDA are tholeiitic and alkali olivine basalts. The dominant minerals in the basalts are olivine (Fo_{50} to Fo_{90}), plagioclase (average An_{65}), clinopyroxene, minor magnetite, and illmenite (Rightmire and Lewis 1987 [156441], p. 10). The interbedded sedimentary material was deposited by rivers and streams draining the surrounding mountains, as well as in lakes that formed when lava flows dammed these streams (Rightmire and Lewis 1987 [156441], p. 11). Eolian deposits are also present. Mineralogically, the interbedded sedimentary material consists of quartz, plagioclase, potassium feldspar, clinopyroxene, olivine, chlorite, clays (illite, illite/smectite, and kaolinite, in order of abundance), and amorphous silica. Calcite-rich and iron-oxide coated horizons exist in the interbeds (Rightmire and Lewis 1987 [156441], pp. 11, 20–24). As mentioned previously, fractures are often filled with sediment and have deposits of calcareous clay.

In terms of their bulk composition, the rocks at Yucca Mountain are classified as rhyolitic and quartz-latitic tuffs. The vitric nonwelded tuffs are composed of sodium- and potassium-rich glass

(Broxton et al. 1987 [102004], Table 3; Vaniman et al. 1996 [105946], Table 1-7). The interiors of thick welded tuffs have devitrified to quartz and feldspar. Phenocrysts include plagioclase (An_{10} to An_{30}), potassium feldspar, biotite [Mg/(Mg+Fe) = 35 to 70%] (Vaniman et al. 1996 [105946], Figure 1.22), and quartz, with trace amounts of hornblende, pyroxene, and magnetite. Major alteration products include smectite, zeolites, silica, and calcite in the rock matrix (Vaniman et al. 1996 [105946], Section 4), and opal, calcite, smectite, zeolites, manganese oxide, and hematite deposited along fracture walls (Vaniman et al. 1996 [105946], Section 5.5).

One factor likely to influence the transport of actinides at the SDA, and potentially at Yucca Mountain, is the dissolved inorganic carbon (DIC) concentration of the groundwater. The DIC of the groundwater is a function of the carbon dioxide partial pressure of the gas in the recharge environment and of the extent to which calcite or other carbon-bearing minerals have been dissolved along the flow path. The DIC of groundwater affects the migration of radionuclides because of the tendency for U, Pu, and other actinides to form aqueous complexes with carbonate (CO_3^{2-}) ions (Langmuir 1997 [100051], pp. 495–530). The formation of neutral or negatively charged aqueous complexes reduces the proportion of the actinides that are present in solution (as positively charged ions that tend to sorb to the rock as a result of ion exchange or surface complexation reactions), thus enhancing the mobility of the radionuclide in groundwater (Langmuir 1997 [100051], pp. 537–538).

Calcite is present in the soils and along fractures in the UZ at Yucca Mountain (Paces et al. 1998 [107408]), and in the surficial sediments, sedimentary interbeds, and fractures in the basalts at INEEL (Rightmire and Lewis 1987 [156441], pp. 21, 31, 33). The natural background carbon dioxide partial pressures of gases in the UZ at Yucca Mountain (Yang et al. 1996 [100194], Figure 18) and at INEEL (Rightmire and Lewis 1987 [156441], p. 55) are similar (log $P_{CO_2\,(bar)}$ = –3.0), and the natural background oxygen partial pressures at the two sites are approximately at atmospheric levels (log $P_{O_2\,(bar)}$ = –0.7). However, the decomposition of buried organic wastes at the SDA may have caused local, and presumably temporary, increases in the carbon dioxide partial pressure, as indicated by calculated log P_{CO_2} for soil water that are much greater than –3.0 (see below). The same processes may have locally reduced log P_{O_2} at the SDA, but no measurements are presently available. In summary, although the background compositions of gases in the UZ at INEEL and Yucca Mountain are similar, the oxidation of buried organic matter at the SDA may have caused local unsaturated zone gas compositions to be substantially different than the gas compositions that exist at Yucca Mountain today.

The chemistry of selected unsaturated zone pore and perched water, and regional groundwater from Yucca Mountain and the SDA, is given in Table 10.3-1. The data for these wells show that the groundwater from the SDA has higher concentrations of most major species except for dissolved silica. Speciation calculations show that the water samples from Yucca Mountain are at or slightly below saturation with calcite and have values of log $P_{CO_2\,(bar)}$ between –3.17 (UZ-14 CHn) and –2.41 (WT-3); water samples from the SDA are all slightly supersaturated with calcite and have values of log $P_{CO_2\,(bar)}$ between –3.03 (well 92) and –2.52 (W02).

At Yucca Mountain, clays, zeolites, and iron- and manganese-oxide coatings that exist in rock pores and fracture walls could sorb radionuclides and slow their migration (Vaniman et al. 1996 [105946], Section 4). Clays and iron-oxide coatings are ubiquitous in the surficial sediments, sedimentary interbeds, and sediment-filled fractures in the basalts at INEEL (Rightmire and

Lewis 1987 [156441]). At both Yucca Mountain and INEEL, the dominant clays are smectites (Vaniman et al. 1996 [105946], Section 5.5.6) or mixed illite/smectite (Rightmire and Lewis 1987 [156441], Table 5); generally, the cation exchange capacity of the clays increases with the percentage of expandable smectitic clay layers. In terms of sorbing substrates, zeolites are more prevalent at Yucca Mountain (Bish and Chipera 1989 [101195]), and iron oxides more prevalent at INEEL, because of the presence of abundant iron in the basalts.

There appears to be more organic matter at the SDA than at Yucca Mountain. In addition to the organic matter mixed with the radioactive waste (Rawson et al. 1991 [156439], p. 478; Magnuson and Sondrup 1998 [156431], p. 4-48), the sedimentary interbeds at the SDA contain organic-rich paleosols (Rightmire and Lewis 1987 [156441], p. 27). Organic matter has the potential to facilitate the movement of radionuclides by forming anionic organic complexes with little tendency to sorb on rock surfaces (Langmuir 1997 [100051], pp. 523–524).

10.3.5.3 Other Challenges and Benefits of Using INEEL as an Analogue for Radionuclide Transport

Several challenges exist if the SDA is used as an analogue for radionuclide transport. The first challenge is that the source terms for various radionuclides are uncertain. The source term reflects the mass of the radionuclide buried in the SDA, its solubility in the existing hydrochemical environment, and its rate of release from any encapsulating medium. Recent attempts to model the observed movement of nonradioactive contaminants beneath the SDA have shown that model results are as sensitive to the assumptions about the poorly known source terms as they are to the expected uncertainty in subsurface transport parameters (Magnuson and Sondrup 1998 [156431], p. 6-2).

The second challenge that the SDA poses as an analogue site is that there has been a lack of consensus on the significance of low-level concentrations of radionuclides in pore and perched water and groundwater beneath the SDA. Many suspected detections of radionuclides have been either near the detection limit, found to be less than the detection limit when resampled, were irreproducible in samples that were split and analyzed by different laboratories, or deemed unlikely to be true detections because of the absence of other radionuclides that should have been present along with the "detected" radionuclide (USGS 2000 [157415], Chapter 4). Even when there has been agreement that the radionuclide is present at statistically nonzero concentrations in the subsurface, there have been questions as to whether or not the contamination was brought into the deeper subsurface during drilling. In summary, there is no well-defined distribution or plume of radionuclides in the deep subsurface that can be used to calibrate geochemical transport models of radionuclides at the field scale.

A third challenge for the potential use of the SDA as an analogue site is that it is hydrogeologically complex. As discussed above, flow through the basalts may depend on local fracture patterns or on details of the configuration of the basalt/interbed interface that may never be known in detail sufficient to make deterministic predictions with confidence. Also, there is uncertainty in the UZ percolation flux because of past flooding events at the SDA and possible lateral migration of water in the deep UZ from nearby water-spreading areas (Magnuson and Sondrup 1998 [156431], pp. 6-3, 6-4). Predictions of radionuclide transport are therefore subject not only to uncertainty in geochemical processes and parameters but also to a great deal of

complexity in hydrologic processes. Ideally, a site chosen as an analogue for geochemical processes at Yucca Mountain would exist in a very simple, well-understood hydrologic environment, so that the geochemical processes and parameters could be clearly identified.

In spite of these limitations as an analogue site, the SDA has produced a great deal of site data, and many analyses have been done of both the hydrologic and geochemical environment at the site. Moreover, INEEL as an institution is highly motivated to collect additional data and perform additional analyses, so that some of the uncertainty discussed in the preceding sections will undoubtedly be reduced at some time in the future. The SDA does not serve as a typical analogue in the sense that it can provide clear, unambiguous, and widely accepted explanations for radionuclide migration that indicate the expected behavior of radionuclides at Yucca Mountain. However, examination of the SDA site by the Yucca Mountain Site Characterization Project (YMP) is useful in that it provides additional opportunities to test models similar to those that have been or will be developed for Yucca Mountain. To better understand which lessons the scientific community (including regulatory agencies and oversight groups) have learned from the SDA is truly relevant to the YMP.

10.3.6 The SDA Modeling Study

The overall purpose of the models developed as part of this study is twofold. First, it is important for INEEL to understand the processes that resulted in the apparent migration of radionuclides to the deep UZ. Only then can they determine if the causes for mobilization and transport of radionuclides continue to exist, or if recent improvements at the site have eliminated the conditions that led to the earlier mobilization of the waste. In particular, if the radionuclides present in the deep subsurface could have been transported there only because of past flooding (and the potential for future flooding has been eliminated by berm construction, drains, or other mechanisms), then the likelihood for continued or renewed mobilization of radionuclides at the SDA may be small. Conversely, if radionuclide migration has resulted from flow-focusing processes that are caused by permanent geologic features of the site, or from geochemical conditions that are likely to persist for a long time, the continued or renewed transport of radionuclides becomes more likely.

For the YMP, it is important to understand if the processes that resulted in the apparent migration of radionuclides at the SDA are present or will be present at Yucca Mountain in the future. If radionuclide transport at the SDA has been facilitated by flooding events or geochemical conditions at the SDA (such as the co-burial of radionuclides and chelate-forming organic chemicals) that are unlikely to exist at Yucca Mountain, then radionuclide migration at the SDA becomes no more than a cautionary warning to "do no harm" to Yucca Mountain by inadvertently altering its natural hydrologic or geochemical state. Alternatively, if radionuclide migration at the SDA is the result of hydrologic or geochemical processes that are or will be common to both sites, numerical transport models of the SDA may have substantial transfer value to the YMP in terms of experience and understanding gained. In any case, modeling radionuclide transport at the SDA provides the possibility to actually test model predictions against reality, a possibility that is lacking at Yucca Mountain.

10.3.6.1 General Strategy for the Calibration of Radionuclide Transport Models at the SDA

In view of the uncertainties in the hydrologic system, the radionuclide source term, and even in the distribution of radionuclides in the field environment at the SDA, two radionuclide transport models were developed: (1) a shallow one-dimensional model extending a few meters from the waste burial pits to the top of the underlying basalt and (2) a deep two-dimensional model extending from the ground surface to the water table beneath the SDA. The purpose of the shallow model is to identify the transport parameters of the sediments through trial-and-error matches of the model to the measured radionuclide concentrations beneath the waste burial pits. This model requires assumptions about the local infiltration rate as well as other transport parameters, but because the measured profile does not extend into the fractured basalts, it is relatively simple hydrologically. The first model was used to simulate the transport of radionuclides in the surficial sediments beneath the waste-disposal pits. Field studies (Humphrey and Tingey 1978 [157491]; Rightmire and Lewis 1988 [156442]; Rawson et al. 1991 [156439]), provided measurements of radionuclide concentrations in a relatively simple hydrologic setting that did not directly involve flow in the fractured basalts. The effects of assumptions regarding source-term inventory and of hydrologic property contrasts were explored in this group of simulations.

The deeper two-dimensional model is restricted to transport of a single tracer. The results of the model were qualitatively compared to measurements of matric potential, observations of perched water, and the distributions of radionuclides and other contaminants in the interbed sediments, perched water, and the Snake River Plain Aquifer. The overall purpose of the two-dimensional model is to identify combinations of rock hydrologic and geochemical properties that could have allowed the deep migration of radionuclides through the basalt layers and interbedded sediments. The fully coupled, nonisothermal, two-phase flow and reactive transport computer codes FLOTRAN (Lichtner 2001 [156429]) and FEHM (Zyvoloski et al. 1997 [100615]) were used for the modeling studies.

10.3.6.2 Numerical Simulations of Water Flow and Conservative Tracer Transport

Single- and dual-permeability models of water flow and conservative tracer transport were based on a highly schematic representation of the UZ beneath the SDA. The purpose of these schematic models was to investigate the conditions under which radionuclides might have reached the B-C and C-D interbeds at depths of approximately 34 and 73 m, respectively. The flow domain for these models extends 60 m in the horizontal direction and from land surface to slightly below the water table at a depth of approximately 180 m. A background infiltration rate of 1 cm/yr (Cecil et al. 1992 [156256], p. 711) was used to establish steady flow conditions in these models and was maintained at land surface outside the waste-disposal area throughout the transient period, assumed to span the last 50 years. Within the 12 m wide waste disposal area, the flux was increased to 8 cm/yr at the start of the transient part of the simulations, reflecting the increase in infiltration rates that are estimated to have occurred at the SDA because of disturbances to the natural conditions following construction of the SDA in 1952 (Magnuson and Sondrup 1998 [156431], pp. 1-5, 1-7). Additional amounts of water (Table 10.3-2) were applied over ten-day periods 10, 17, and 30 yr into the transient part to represent flood events that occurred at the SDA in 1962, 1969, and 1982 (Magnuson and Sondrup 1998 [156431], Table 2-3).

10.3.6.3   Results of Single-Continuum Models

In the single-continuum models, only the fracture-continuum properties of the basalts and the matrix-continuum properties of the surficial sediments and sedimentary interbeds are represented (Table 10.3-3). Shown in Figure 10.3-13 is a comparison of the saturation profile for the single continuum obtained using the computer codes FLOTRAN and FEHM with a numerical solution of Richards equation obtained from Mathematica (Wolfram 1991 [157417]). As can be seen from the figure, excellent agreement is obtained for the two codes, as well as good agreement with the Mathematica solution. The slight offset between FEHM and FLOTRAN can be attributed to differences in the discretization approach used in the codes.

The saturation calculated using the single-continuum model at the end of the 50 yr transient period (2002) is shown in Figure 10.3-14. No significant lateral changes in simulated saturation are present resulting from the higher infiltration rates associated with the waste disposal area in the central part of the model domain. McElroy and Hubbell (1990 [156433], p. 362) reported capillary pressures of 0.2–1.3 bars in the surficial sediments and 0.3–1.3 bars in the 9 m, 34 m, and 73 m interbeds. McElroy and Hubbell (1990 [156433], p. 363) also reported that conditions were wetter at the tops of the sedimentary interbeds than at the bottoms, a condition that is also present across the interbeds in the simulation results (see also Figure 10.3-13).

The relative tracer concentrations (concentration relative to input concentration) at the end of the 50 yr transient period are shown for the upper 80 m of the model domain in Figures 10.3-15a and b for constant and pulse infiltration, the latter representing the flooding events listed in Table 10.3-2. Shown in Figure 10.3-16 is the tracer concentration for both FLOTRAN and FEHM for constant infiltration and pulsed infiltration using FLOTRAN along the centerline of the computation domain. The tracer is applied with unit concentration within the waste-disposal area in the central part of the model domain. Outside this region, a concentration of 10^{-3} is applied. An initial concentration of 10^{-8} is assumed. The model results indicate that a small fraction of a conservative solute could migrate from shallow waste-disposal pits to the 73 m interbed within 50 years, given the infiltration rates and rock properties assumed in this model. The pulse release leads to a somewhat greater penetration depth.

10.3.6.4   Results of Dual-Permeability Models

In the dual-permeability models, the basalt fracture-continuum properties and the sediment matrix-continuum properties are the same as in the single-continuum models and, additionally, the basalt matrix-continuum properties and sediment fracture-continuum properties are included. The FLOTRAN code requires that dual-permeability models have a fracture continuum throughout the model domain, but it is unlikely that the unconsolidated sedimentary layers actually contain fractures. Ideally, then, the fracture continuum in the sedimentary layers would be defined in such a way that it transmits negligibly small amounts of water and does not affect the saturations or capillary pressures in the matrix continuum of the same sedimentary layer or in the fracture continuum of the adjacent basalts. Therefore, the fracture-continuum properties and fracture-matrix interaction terms in the sedimentary layers (see note to Table 10.3-3) were chosen to ensure that the water flow rates, saturations, and capillary pressures of the sedimentary layers in the dual-permeability models were nearly identical to the flow rates, saturations, and capillary pressures of the sedimentary layers in the single-continuum models. This was done by

assigning a low volume to the fracture continuum in the sedimentary layers and making the fracture-matrix interaction term large enough to result in the equivalent continuum limit of the dual-continuum model. Hydrodynamic equilibrium between the fracture and matrix continua in the sedimentary layers is maintained and dominated by the properties of the matrix continuum. The approach was verified by comparing the saturation of the matrix continuum in the dual-permeability model with the saturation of the sedimentary layers of the single-continuum model, in a one-dimensional steady-state model with infiltration rate of 1 cm/yr (Figure 10.3-17). Also shown is the numerical solution to Richards equation obtained using the software code Mathematica (Wolfram 1991 [157417]) for the single-continuum case. Saturation of the sedimentary layers in the two models is nearly identical. As expected, saturation of the fracture continuum of the basalt layers in the dual-permeability model is slightly less than that of the basalt layers in the single-continuum model, because a small part of the flux in the dual-permeability model moves through the basalt matrix. In the upper parts of the individual basalt flow units, the fracture continuum and matrix continuum are not in capillary-pressure equilibrium, probably because the large reduction in the fracture-matrix surface area (0.01) limits water flow from the fractures into the matrix. However, capillary-pressure equilibrium is re-established with depth within the flow unit as water flows from the fractures into the matrix.

The simulated saturation profiles for the fracture and matrix continua of the dual-permeability model are shown in Figure 10.3-18 after an elapsed time of 50 years for constant infiltration. Matrix saturations in the basalts are much higher than fracture saturations throughout the model domain because the assumed moisture retention characteristics allow the matrix to retain more water at high capillary pressures than the fractures. The fracture and matrix continua are in approximate capillary-pressure equilibrium above the 73 m interbed, but, similar to the results of the one-dimensional steady-state dual-permeability model (Figure 10.3-17), the matrix capillary pressures just below the 73 m interbed correspond to drier conditions (have higher capillary pressures) than in the adjacent fractures. Gradually, as water flows from the fractures into the matrix, capillary-pressure equilibrium between the two continua is re-established with increasing depth below the 73 m interbed.

The relative tracer concentrations at the end of the 50 yr transient period are shown for the upper 80 m of the fracture and matrix continua in Figure 10.3-19 for the case of constant infiltration. The fracture-continuum relative concentrations (Figure 10.3-19a) are slightly less than the concentrations of the single-continuum model at the same location (Figure 10.3-15a) because some of the tracer has moved into the basalt matrix in the dual-permeability model. The additional storage provided by the basalt matrix prevents the tracer from arriving at the 73 m interbed in the dual-permeability model. However, tracer is present in the 9 m interbed at a relative concentration of 0.06 and in the 34 m interbed at a relative concentration of 0.03, despite the much lower concentrations or absence of the tracer in the overlying basalt matrix (Figure 10.3-19b). Clearly, the tracer distribution in the matrix continuum of the A-B and B-C interbeds reflects the transport of tracer almost exclusively through the fractures of the basalt units.

It should be noted that in the single-continuum models, the basalt layers used the properties listed for the A-, B-, C-, and D-basalts. In the dual-permeability models, these property values were used for the fracture continuum in the appropriate layer, and "basalt matrix" properties were used for the matrix in all basalt layers. All layers (including sedimentary layers) in the dual-permeability model were assumed to have cubic matrix blocks 1 m on a side and a bulk fracture

porosity of 0.01. Fracture-continuum properties of the sedimentary layers were assumed to be the same as those given for the matrix in Table 10.3-2. In the basalt layers, the effective fracture-matrix area calculated from the block dimensions was reduced by a factor of 0.01 based on model calibration results of the large-scale infiltration test (Section 9.3). In the sedimentary layer, the fracture-matrix area was increased by a factor of 100 to ensure hydrodynamic equilibrium between the fracture and matrix continua. The equivalent continuum permeability was twice that given for the interbed matrix permeability.

10.3.6.5   Flow and Transport Simulations with Dipping, Discontinuous Layers

The previous simulations in Sections 10.3.6.3 and 10.3.6.4 have considered an idealized hydrostratigraphy for the SDA in which layers are horizontal and of uniform thickness. In contrast, structural contour and isopach maps (see Section 10.3.3) indicate that the SDA is located in an area where the surficial-sediment/basalt interface is relatively low and where the interbeds have variable thicknesses and dips. To examine the effect that departures from the idealized stratigraphy of the previous case might have on flow and transport beneath the SDA, investigators created a model with the computer code FEHM that considers the structural depression in the A-basalt beneath the SDA and treats the 9 m and 34 m interbeds as dipping discontinuous layers (Figure 10.3-20). The C-D interbed is horizontal with uniform thickness, as in the previous calculations.

The FEHM model is based on a single-continuum representation with the same hydrologic properties as used in the previous single-continuum models (Table 10.3-3). The FEHM model has a constant vertical node spacing of 0.5 m and horizontal node spacing of 1.0 m. In this model, the pulses of water associated with flooding events are not used; instead, the flux in the central 12 m of the model domain was increased to 10 cm/yr during the 50 yr transient period to implicitly account for these events. This led to slightly more water being introduced into the UZ than in the previous models for the last 50 yrs (5 m for this model compared with the 4.61 m of water introduced for the cases with flood events).

For a steady-state uniform infiltration rate of 1 cm/yr, flow-lines calculated by particle tracking in FEHM indicate that the clay layer at the base of the surficial sediment strongly focuses flow toward low areas in this layer beneath the hypothetical SDA, at the center of the model domain (Figure 10.3-21). The interbeds also divert water laterally along their upper surface, but the amount of offset for the flow lines is less than 5 m at any interbed. Because water flow is focused by the slope of these layers, wetter conditions exist at low points in the clay layers and where the interbeds terminate, even when infiltration rates are uniform. (Note that water potentials were calculated by subtracting a uniform air pressure of 1 bar from the calculated water pressure; a water potential of 0 bars indicates saturated conditions.)

Saturations calculated at the end of the 50 yr transient period, in which 10 cm/yr of infiltration was applied in the central 12 m of the flow domain, indicate that the basalts are wettest below the ends of the overlying interbeds (Figure 10.3-22). Tracer concentrations near the water table at the end of the 50 yr transient period are highest where the 34 m interbed has focused water flow (Figure 10.3-3). Peak tracer concentrations at the water table are about 0.12 compared to peak concentrations of about 0.05 for the case with uniform, horizontal layers. Although slightly more water was applied in the case with discontinuous layers, the pattern of saturation (Figure 10.3-

22) and tracer concentrations (Figure 10.3-23) suggests that part of the early breakthrough is caused by some water flowing around rather than through the high-porosity interbeds. Also, flow rates are relatively high where flow is focused by the dipping, discontinuous layers.

10.3.6.6   Reactive Transport Calculations

In this section, vertical radionuclide transport through the surficial sediment zone in the SDA is investigated. Using representative soil-zone water and P_{CO_2}, along with surface site density, cation exchange capacity, and mineralogy of the soil zone, sorption profiles for ^{241}Am, ^{238}Pu, ^{137}Cs, and ^{90}Sr were calculated and compared with field observations. The resulting model calibration predicts a high retardation factor for Np and essentially no retardation for U.

10.3.6.6.1   Sorption Reactions: Surface Complexation and Ion Exchange

Both surface complexation reactions and ion exchange are included in the description of sorption. The radionuclides americium and plutonium take part in surface complexation reactions, and cesium takes part in ion exchange. Strontium is involved in both sorption processes. The generic form of surface complexation reactions can be written as

$$X_m^\alpha + \sum_j \nu_{jk}^{m\alpha} A_j \Leftrightarrow A_k^{m\alpha} \qquad\qquad \text{(Eq. 10-2)}$$

where X_m^α denotes the surface site of type α, A_j an aqueous primary species, $A_k^{m\alpha}$ the sorbed surface complex, and $\nu_{jk}^{m\alpha}$ the stoichiometric coefficient matrix. This description neglects the role played by the counter ion and therefore does not conserve charge separately within the aqueous and solid phases whenever the surface complex is charged. It is presently unknown what effect this inconsistency may have on predicting retardation and changes in solution chemistry, such as pH (Lichtner 1996 [101409], pp. 57–59). Ion exchange reactions have the form

$$z_j X_{z_i} A_i + z_i A_j \Leftrightarrow z_i X_{z_j} A_j + z_j A_i, \qquad\qquad \text{(Eq. 10-3)}$$
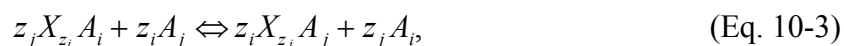
where $X_{z_i} A_i$ refers to the sorbed cation. These reactions conserve charge rigorously in both aqueous and solid phases, unlike the representation used for surface complexation reactions. Sorption reactions for surface complexation included in the model calculations are listed in Table 10.3-4 along with corresponding selectivity coefficients. The data were taken from Zavarin and Bruton (2000 [156443] and 2000 [156444]). Cations taking part in ion exchange reactions are listed in Table 10.3-5, along with their selectivity coefficients. The data were adapted from generic values given in Appelo (1996 [156425]).

Generally, sorption reactions involve multiple sorption sites associated with different mineral surfaces. Two distinct philosophies have been articulated in the literature (Davis et al. 1998 [154436]) for modeling sorption reactions. One approach is to develop a detailed model based on the specific minerals present in the sorbing medium. This approach has the advantage of being more mechanistically based and having the potential capability of incorporating changes in mineral abundances on sorption. Its primary disadvantage is the extensive amount of data required as input parameters to the sorption model. An alternative approach is based on the bulk properties of the porous medium. This approach is more phenomenological, but has fewer data

requirements. It is based on direct measurements of bulk properties such as cation exchange capacity (CEC) and surface site densities. In this report, the bulk approach is used, employing a multisite description of surface complexation reactions and a single-site representation of ion exchange reactions.

For a dilute aqueous solution, retardation of a particular primary species is derived from the distribution coefficient K_j^D, defined as the ratio of total sorbed to total aqueous concentration of that species

$$R_j = 1 + K_j^D \qquad \text{(Eq. 10-4)}$$

The distribution coefficient is given by the expression

$$K_j^D = \frac{1}{\phi \Psi_j} \left[\sum_{km\alpha} v_{jk}^{m\alpha} \Xi_k^{m\alpha} + \Xi_j^{ex} \right] \qquad \text{(Eq. 10-5)}$$

involving a sum over surface complexation and ion exchange isotherms, where $\Xi_k^{m\alpha}$ refers to the sorbed concentration of surface complex $A_k^{m\alpha}$, and Ξ_j^{ex} refers to the ion exchange isotherm. The quantity Ψ_j represents the total aqueous concentration of the subscripted species.

Sorption reactions used for surface complexation include the surface sites: >FeOH, >SiOH, >AlOH, and >Ca^{2+}. Unknown is the appropriate site density to use in the calculations. The site concentration associated with the mth mineral, denoted by n_α^m [mol/dm^3], can be expressed as a product of a number of factors involving the intrinsic mineral site density (η_α^m [# sites/nm^2]), mineral concentration ($\rho_m \phi_m$ [kg/dm^3]), and mineral specific surface area (A_m [m^2/kg]). Thus, the site concentration can be calculated from

$$n_\alpha^m = \frac{1}{N_A} \eta_\alpha^m A_m \rho_m \phi_m \qquad \text{(Eq. 10-6)}$$

where N_A denotes Avogradro's number, the intrinsic site density is denoted by η_α^m, and the specific surface area is represented by A_m.

Retardation caused by ion exchange is proportional to the CEC of the exchanging medium and the bulk rock density. The conventional definition of the CEC is in units of meq/100 g solid. A more useful quantity is mole equivalents of exchange sites per bulk volume of porous medium, denoted by the symbol ω. The two quantities are related by the porosity and grain density of the porous medium

$$\omega = (1 - \phi) \rho_s \text{CEC} \qquad \text{(Eq. 10-7)}$$

where ρ_s denotes the grain density and ϕ the porosity. Retardation is proportional to ω and, thus, to the product of the bulk density and the CEC.

10.3.6.6.2   Model Simulations

Calculations were performed in one dimension with a constant infiltration Darcy flow rate of 10 cm/yr, a porosity of 50%, and an average saturation of 0.58 (Magnuson and Sondrup 1998 [156431], p. 4-8, Table 4-2). Radioactive decay was not included in the simulations. An aqueous diffusion coefficient of 10^{-5} cm^2/s with a tortuosity of 0.294 taken from Magnuson and Sondrup (1998 [156431], Table 4-2, p. 4-8) for the surficial sediment layer was used in the simulations.

The injection fluid composition is listed in Table 10.3-6. The fluid composition is taken from Well 99 corresponding to perched water as listed in Table 10.3-1. The pH was adjusted to give equilibrium with calcite, which otherwise would have been supersaturated by one log unit. This adjustment resulted in a reduction in the reported pH of 8.4 to 7.59. The redox state of the fluid is not given in Table 10.3-1. As discussed below, to obtain a simultaneous fit to the concentration profiles for plutonium and americium, it was necessary to invoke reducing conditions. The initial fluid composition was set to be the same as the injection fluid, with the exception of the radionuclide concentrations: plutonium, americium, cesium, uranium, and neptunium, which were set to small values (10^{-20} mol/L) and strontium, which was given the value of 5×10^{-16} mol/L to fit the minimum observed strontium value. It was not determined how much of the strontium profile resulted from nonradioactive strontium that was naturally occurring. The calculated $log\ P_{CO2}$ = -2.18, which is quite high, presumably resulted from decomposition of organic matter in the waste and soil zones. As can be seen by inspection of Table 10.3-6, carbonate complexes play an important role in speciation of americium and uranium and less so for neptunium. Plutonium exists primarily in the IV oxidation state in the form of the complex Pu(OH)$_4$.

The observed sorbed concentration profiles were fit by adjusting the surface site densities and the injected radionuclide concentrations. Site densities >FeOH, >AlOH, and >SiOH were adjusted to fit the observed profiles. The >Ca^{2+} site density was arbitrarily set to 10^{-4} mol/L. The resulting site densities used in the simulations are listed in Table 10.3-7.

Speciation results of the injection fluid for the amount sorbed for different radionuclides participating in surface complexation are presented in Table 10.3-8, in which the contribution to the distribution coefficient is listed for each surface site. It can be seen that plutonium contains contributions from sorption sites >FeOH and >AlOH, whereas americium is primarily sensitive to site >AlOH and to a lesser extent site >Ca. There were no data available for uranium and neptunium. The distribution coefficients are much smaller than those reported by Dicke (1997 [157410]) as listed in Table 9.3-1.

An entirely different result is obtained under oxidizing conditions. In this case, both plutonium and americium are strongly sorbed to >FeOH, with americium several orders of magnitude greater compared to plutonium. Because under oxidizing conditions plutonium is not sorbed to any other sites, it is not possible to fit the plutonium and americium profiles simultaneously under these conditions.

Generic values for the ion exchange selectivity coefficients (see Table 10.3-5) were taken from Appelo (1996 [156425]). The CEC was varied to fit the cesium profile. A value of 0.02 mol/kg was obtained. This value is at the lower limit of the reported CEC range for the surficial

sediments of 0.27 to 0.02 mol/kg (Rightmire and Lewis 1987 [156441], Table 5). The strontium profile was predicted by the model without any additional fitting.

The resulting fit to the data is shown in Figure 10.3-24, corresponding to advection and diffusion. The obtained fit does not capture the observed decrease in plutonium concentration at depth of approximately 1 m. This discrepancy could be a result of several factors, including heterogeneity, lateral flow, and the possibility of the presence of the contact between the clay and basalt layer that occurs at this depth. Other species also indicate a slight increase in concentration at this depth.

10.3.7 Discussion

Several interpretations of radionuclide transport in the surficial sediment zone are possible. One is that lateral flow occurred, sweeping out part of the radionuclide plume. The thickness of the stratigraphic layers is highly irregular, and the possibility exists that flow occurred along the interface between the clay layer and the surficial sediment layer. Another possibility is that a catastrophic or sudden release of a pulse of fluid, caused by a flooding event, released a pulse of radionuclides that propagated downward with reduced retardation, due to kinetic effects caused by fast flow rates. For this situation, the data are interpreted as background flow (or diffusion) producing the upper monotonically decreasing profile with depth. The lower portion of the profile, where the concentration is increasing was the result of a sudden flow event. Presumably, according to this interpretation, the peak lies at a still greater depth below that at which the data were collected.

The model calculations predict retardation factors for neptunium and uranium that are seen to be orders of magnitude higher compared to the other radionuclides. This result would indicate that very little movement of neptunium and uranium should be observed. No values for these radionuclides were reported that could be taken as consistent with their predicted high retardation.

Finally, although it was necessary to assume reducing conditions for fluid coming from the SDA, it is not expected that such conditions would persist at greater depths because of the partially saturated conditions that are present there, leading to oxidizing water.

10.3.8 Conclusion

The main conclusion to be drawn from this study is that INEEL presents a far wetter environment than that of Yucca Mountain. This increase in infiltration is manifested in higher infiltration at the SDA and flooding events that could have resulted in enhanced radionuclide migration beneath the SDA. Focused flow resulting from the undulating topography of the basalt flows and sedimentary interbeds would be expected to exacerbate the situation, leading to even greater distances of radionuclide migration, as demonstrated in the modeling exercises.

It was found that to fit observed radionuclide concentrations in the surficial sediment layer, reducing conditions were required. Otherwise, it was not possible to fit the observed profiles of both americium and plutonium simultaneously. Note that although detailed waste compositions are not currently known, there is significant organic matter in the waste that is not inconsistent with the assumption of reducing conditions. However, as noted above, such conditions are not

expected to prevail at greater depths, where the system would be expected to be oxidizing. The calculated profiles did not capture the increase in concentration observed at greater depth near the base of the surficial sediment layer. To further test and validate model predictions, continuity of data at greater depths beneath the SDA would be needed along with site-specific data for surface complexation site densities.

10.4 RADIONUCLIDE FLOW AND TRANSPORT STUDIES AT PEÑA BLANCA, MEXICO

10.4.1 Objectives

The goal of these studies is to construct a three-dimensional conceptual model of the transport of uranium and radiogenic daughter products at Peña Blanca, Mexico (*Technical Work Plan for Natural Analogue Studies for License Application* (BSC 2001 [157535], p. 4)). A three-dimensional model will extend the previous work at Peña Blanca that was limited to collection of data for exposed planar surfaces. The model will also address whether there has been preferential flow/drainage downward through fractures or if there has been a net flux of uranium off-site. To accomplish this, three wells will be drilled at the site to obtain core samples from within and beneath the uranium ore body and to collect water samples from beneath the ore body. The core and water samples will be analyzed using a variety of techniques to support development of the conceptual model of transport at Peña Blanca. The conceptual model will then be tested using numerical methods employed by the UZ Flow and Transport Model to build confidence in understanding UZ transport at a potential Yucca Mountain repository.

10.4.2 Background

In the 1970s, the Peña Blanca region, approximately 50 km north of Chihuahua City, was a major target of uranium exploration and mining by the Mexican government. Since that time the Nopal I uranium deposit has been studied extensively because it is a good analogue for evaluating the fate of spent fuel, associated actinides, and fission products at a geologic repository in unsaturated volcanic tuff. Previous studies associated with Peña Blanca as well as a geologic description of the site were reviewed in *Natural Analogs for the Unsaturated Zone* (CRWMS M&O 2000 [141407]). Briefly, the Nopal I uranium deposit at Peña Blanca represents an environment that closely approximates that of the potential high-level radioactive waste repository at Yucca Mountain, Nevada, in the following ways:

- Climatologically: both are located in semi-arid to arid regions

- Structurally: both are parts of a basin-and-range horst structure composed of Tertiary rhyolitic tuffs overlying carbonate rocks

- Hydrologically: both are located in a chemically oxidizing, UZ 100 m or more above the water table

- Chemically: the alteration of uraninite to secondary uranium minerals at Nopal I may be similar to the eventual fate of uranium fuel rods in a potential geologic repository like Yucca Mountain.

10.4.3   Previous Radionuclide Transport Studies at Peña Blanca

Studies of uranium-series disequilibria within and around uranium deposits can provide valuable information on the timing of actinide mobility and hence the undisturbed stability of a potential repository over the geologic time scales associated with the required lifetime of the facility. Previous studies at Peña Blanca dealing with bulk samples and fractures have focused on the extent and timing of uranium-series mobility or transport at this site, and have been summarized in *Natural Analogs for the Unsaturated Zone* (CRWMS M&O 2000 [141407]). Some of these studies reported open-system behavior, suggesting mobility of uranium and its daughter products. In contrast, previous uranium-series thermal ionization mass spectrometry (TIMS) work at Nopal I (CRWMS M&O 2000 [141407], pp. 89–90) found closed-system behavior, suggesting very limited mobility in fracture-filling material for uranium. Briefly, the TIMS results indicated that the uranium (235, 238), thorium, and protactinium in the fracture-filling minerals have remained stable for more than 300 ka at Nopal I.

Pickett and Murphy (1999 [110009]) presented measurements of U-Th isotopic composition and concentration in various water samples collected near the Nopal I uranium deposit during relatively wet conditions (see 1995 collections in Table 10.4-1). The observed uranium and thorium concentrations generally correlate with concentrations of major cations and anions and total conductivity, which may reflect evaporation-dilution or rock dissolution effects on all of these species. Thorium and uranium concentrations also correlate strongly with each other, which is surprising given the expected differences in solution chemistry and potential solubility controls for these two elements. Pickett and Murphy (1999 [110009], p. 812) interpreted these concentrations in the context of solubility control by various uranium silicate minerals (haiweeite, soddyite) and thorianite. They found that the perched water is close to solubility for haiweeite, a calcium uranyl silicate mineral. All of the other waters are undersaturated with respect to uranium mineral phases. However, all of the waters are supersaturated with respect to thorianite, which is attributed to the presence of colloidal thorium in the <0.2 μm fraction of these samples. The occurrence of undersaturation for uranium and supersaturation for thorium indicates that radionuclide transport in the UZ may be controlled by kinetic factors such as evaporation, rock dissolution, and colloid formation, which complicate the interpretations based on thermodynamic (solubility) considerations. The incorporation of kinetic factors will be discussed below with respect to the generalized radioisotope transport model of Ku et al. (1992 [109939]).

10.4.4   Ongoing Work at Nopal I

As previously summarized, prior work at Peña Blanca contrasts the long-term stability of uranium and thorium in fractures against the ongoing dissolution of uranium by surface waters, as evidenced by elevated uranium concentrations and $^{234}U/^{238}U$ in adit seepage waters. The net flux off-site is not well constrained other than by the 8 ± 5 m.y. age of the primary uranium mineralization at Nopal 1 (Pearcy et al. 1994 [100486], p. 729). Current (2002) work is discussed in the following subsections.

10.4.4.1 Drilling

The goal of current work (BSC 2001 [157535], p. 4) is to extend geochemical studies to the third dimension by drilling wells at Nopal I. Work is now underway to drill one borehole through the uranium ore deposit to a depth of approximately 200 m. The borehole is planned to penetrate the SZ to at least 20 m, and core will be collected during drilling. In addition, two additional wells will be drilled at approximately +50 m and –50 m from the borehole. Monitoring wells will be installed to sample ground water on a quarterly basis.

10.4.4.2 Surface Water Sampling

The work of Pickett and Murphy (1999 [110009]) has been extended to include water samples collected at Nopal I during the dry season. Samples were collected in February 2000 and March 2001 (Simmons 2002 [157544], pp. 86–87). These data provide new information on temporal and seasonal variations at the site (see Section 10.4.4.4). As with the previous work, samples are of three different types: (1) perched water trapped in an old borehole about 20 m outside the deposit, (2) seep water obtained from an old adit approximately 8 m below the +10 m surface (see Figure 10.4-1), and (3) a groundwater sample located in the regional carbonate aquifer 1.3 km southeast of the deposit. In addition, data has been collected from an old mining camp well located about 0.6 km southeast of the deposit.

These new data, along with the 1995 data from Pickett and Murphy (1999 [110009]), are detailed in Table 10.4-1. In many cases, the new data show higher uranium concentrations ratios than the results from Pickett and Murphy for samples collected during the wet season. This could result from longer fluid/rock interaction times or from greater evaporation. A portion of the collection system is shown in Figure 10.4-2. The water is collected in plastic sheets, in which it remains until sampled. Although the adit is comparatively cool and damp, evaporation could greatly influence the uranium concentrations.

Stable isotope data were obtained for some of these adit samples to evaluate the effects of evaporation on the uranium concentrations. These data are shown in Figure 10.4-3. When water evaporates, the isotopic composition of the resulting vapor will be shifted to lower values of $\delta^{18}O$, and the residual water will be shifted to higher values on a plot of δD versus $\delta^{18}O$. The stable isotope data for AS-5 (from a water well) and AS-6 (from a drill hole into a perched water horizon) have significantly lower values than other samples. They fall on the Global Meteoric Water Line (GMWL) and probably represent the average composition for the precipitation at the site. The adit samples all lie much higher on this plot. Of these, AS-2, AS-3, and AS-4 all fall significantly to the left of the GWML and may represent atmospheric water vapor that has diffused into the adit and condensed in the cooler, underground environment, followed by some period of evaporation in the collection system. AS-1 lies on the GMWL, but probably does not represent a rainwater sample, because it is relatively high for meteoric water at this latitude; it is closer to the opening of the adit and may represent a more evaporated version of cluster AS-2, AS-3, and AS-4. The evolution of stable isotopes for the adit samples appears to have at least three components: (1) evolution of vapor from GMWL, (2) modification by water/rock interaction, and (3) evaporation in the adit collection system. A simpler approach planned for evaluation is to normalize the uranium data to chloride or bromide concentrations.

10.4.4.3 Radioisotope Transport Modeling

A model based on naturally occurring uranium- and thorium-series disequilibria is being tested for characterization of the *in situ* migration of actinide nuclides in and around the Nopal I uranium deposit. Estimates can then be made of the rates of sorption-desorption, hence retardation factors, and dissolution-precipitation of the isotopes over a range of time scales, in both the SZ and UZ. Such information is vital to testing or validating performance assessment models for geologic nuclear waste disposal.

Current models utilizing uranium- and thorium-series disequilibria for radioisotope transport in geologic systems are primarily based on the steady-state flow assumption (Ku et al. 1992 [109939], pp. 639,640). These models, while elucidating the behavior of radioisotopes in the phreatic zone, may not sufficiently constrain the isotope transport in unsaturated vadose layers where the concentration and transport behavior of radioisotopes are often governed by nonsteady conditions. During the past year, the uranium-series transport model of Ku et al. (1992 [109939]) has been extended to include the nonsteady-state situations. Free of the steady-state assumption, this new, generalized radioisotope transport model has the two important features of being applicable to both the SZ and UZ, and providing simultaneous constraints on the behavior of radioisotopes in dissolved, colloidal, sorbed, and solid pools of a groundwater system.

The model makes the following assumptions: (1) in natural water-rock systems, radionuclides reside in four "pools"—dissolved, colloidal, sorbed, and solid—with the colloidal pool being treated as a mobile particle pool; (2) radionuclides in the sorbed and colloidal pools are in first-order sorption equilibrium with those in the dissolved pool; (3) radionuclides in the solid pool are transferred to the dissolved pool through dissolution and α-recoil, whereas those in the dissolved pool are incorporated into the solid pool through precipitation.

The data in Table 10.4-1 have been analyzed using this model. In contrast to the thermodynamic modeling of Pickett and Murphy (1999 [110009]), this model provides a means to characterize kinetically controlled radionuclide transport at Peña Blanca. The uranium data from the 1995 wet-period measurements are shown in Figure 10.4-4.

As predicted by the model, a linear relationship exists between $^{234}U/^{238}U$ and $1/^{238}U$ in waters collected from the vadose zone near the Nopal I uranium deposit (Figure 10.4-4a), due to α-recoil-induced ^{234}U enrichment in the water. The one sample from the carbonate aquifer (SZ) shows a much lower $^{234}U/^{238}U$ ratio, perhaps caused by prolonged interaction with old calcites in the aquifer, allowing uranium exchange between rock and solution to mask the effect of ^{234}U enrichment in the water. Using the model as well as the slope and intercept from Figure 10.4-4a, the relative input rates of uranium from solids to the solution through dissolution and α-recoil can be derived. The ^{234}U α-recoil rate for the adit fluids is calculated to be ~9 dpm/L/yr. The dissolution rates are ~8.3 dpm/L/yr for ^{238}U and ^{234}U (or 47×10^{-9} mol/L/yr for ^{238}U and 2.6×10^{-12} mol/L/yr for ^{234}U).

The model also allows determination of the fluid transit time (τ_w) in the UZ. Because of the short transit time of water in the UZ, ^{238}U concentrations increase linearly with increasing τ_w (Fig. 10.4-4b). Meanwhile, the $^{234}U/^{238}U$ ratio decreases rapidly with increasing τ_w and very high $^{234}U/^{238}U$ ratios can occur when the water has a very short transit time in the UZ. It is estimated

that the transit time for the seep water that infiltrated into the Level +00 adit 8 m below the surface is about 6–29 days; for the perched water at 10.7 m depth in an old borehole, the transit time is about 0.4–0.5 years. The large values of τ_w for the perched water may reflect the long residence time of water in the borehole. Note that because water at different sites may have different pathways, the value of τ_w itself does not provide information on possible connections between the perched and seep waters sampled. In conclusion, although the water transit time in the UZ is quite short, significant dissolution of uranium may have occurred in a low-water flux, high-uranium concentration setting near the Nopal I uranium deposit.

10.4.4.4 Seasonal Variability of Uranium Dissolution Rate in UZ

To assess temporal variations in the transport of uranium in the UZ, samples of perched and adit seep waters were collected during the dry winter season in late February 2000 and again in early March 2001. The results are plotted in Figure 10.4-5a. Compared with samples collected during the September wet season of 1995, many of these new measurements show much higher ^{238}U concentration and lower ^{234}U/^{238}U, suggesting increased uranium dissolution and/or lower α-recoil associated ^{234}U enrichment rates during the dry season. The low humidity during the dry season may have also enhanced evaporation, causing higher uranium concentrations in the waters sampled.

The data collected during the winter dry season depart considerably from the linear relationship between ^{234}U/^{238}U and $1/^{238}$U predicted by the model for the wet season of 1995 (Figure 10.4-5a). Such a departure could result from: (1) high and variable evaporation under low humidity conditions and (2) incomplete flushing associated with low rainfall during the dry season. Linear regressions on data for the perched and adit seep waters collected during March 2001 give a ^{234}U α-recoil rate (λP_r) of ~5.7 dpm/L/yr. Compared to the ~9 dpm/L/yr for the wet season, this lower α-recoil rate estimate may reflect incomplete flushing of waters through the vadose layers during the dry season. Dissolution rates of uranium are estimated to be about 24 dpm/L/yr for ^{238}U and ^{234}U (or 136×10^{-9} mol/L/yr for ^{238}U and 7.5×10^{-12} mol/L/yr for ^{234}U). These rates are about three times higher than those in the wet season, possibly suggesting a favorable physiochemical condition (e.g., increased oxygenation) for uranium dissolution during dry periods. In this context, it should be noted that the samples collected 15 m from the adit entrance show ^{234}U/^{238}U values lower than secular equilibrium, which suggests dissolution of material previously preferentially depleted in ^{234}U by α-recoil effects.

Note in addition that large variations in the ^{238}U concentration and ^{234}U/^{238}U ratio were also found in samples collected from the SZ during the dry season (Figure 10.4-5b). While no clear correlation between ^{238}U and ^{234}U/^{238}U is seen, the plots suggest that both the decreased water infiltration flux and the increased uranium dissolution rates in the vadose zone may contribute to the higher dry-season uranium concentrations in the SZ. Observations such at these may have important implications for the effects of climate change on the long-term stability of uranium in the environment.

10.4.5 Work in FY02

Although the data and modeling discussed above provide useful preliminary data for uranium transport at Peña Blanca, spatial dependence and the net flux of uranium transport from the

deposit via groundwater cannot be thoroughly evaluated without higher resolution sampling of any potential groundwater uranium plume in the vicinity of the deposit. This will be accomplished through the drilling program at Nopal I (BSC 2001 [157535], pp. 4–5).

In addition to the core and fluid samples from the borehole and wells, the perched, seep, and aquifer waters from the sites previously sampled will be resampled (see above). Where adequate samples can be obtained, isotopes will be measured of uranium (^{234}U and ^{238}U), thorium (^{232}Th, ^{230}Th, ^{228}Th, and ^{234}Th), radium (^{226}Ra, ^{228}Ra), polonium (^{210}Po) and lead (^{210}Pb) in the fluid samples. Radioactive disequilibria in sorbed phases will also be studied, using leaching methods on the core samples. Since it may be difficult to collect enough fluids from the UZ for all of the proposed measurements, data on the sorbed phases should provide an alternative way to assess the radionuclide transport in the UZ.

The U-series modeling effort will be extended to the thorium and radium isotopes. Measurements of polonium and lead isotopes will be applied to the Th model to further evaluate the role of colloids in the transport of these nuclides. Modeled results on uranium transport may be affected by the evaporative concentration in UZ fluids. To correct for this possible effect, the chloride or stable isotope measurements made on water samples from the UZ will be compared with those on rainwater. Model sensitivity and validity will be tested, and ways to evaluate the uncertainties of model parameters will be sought. Results from the Peña Blanca analogue study will be provided for testing the UZ process model.

10.5 OTHER TRANSPORT ANALOGUES

10.5.1 Steenkampskraal

The Steenkampskraal monazite mine, located about 100 km south of Vaalputs, South Africa, provides an example of colloidal transport of radionuclides in the UZ (Figure 10.5-1). Steenkampskraal is a licensed low-level waste radioactive-waste disposal site in South Africa that is being considered as a potential high-level waste disposal site. Steenkampskraal is the richest monazite ore body in the world. From 1952 to 1963 it was the world's leading producer of thorium and rare earth elements (REE), with total production estimated at 50,000 metric tons of monazite concentrate, containing 45 wt % REE oxides, 4% thorium oxide, and 600 ppm uranium oxide (Jarvis et al. 1997 [157489], p. 12). Monazite and fluorapatite together constitute approximately 80% of the ore mass, along with minor sulfides, oxides, and silicates. Locally, the ore shows enrichment of Fe/Ti oxides. The mine is situated within the granulite facies high-temperature zone of the Namaqualand Metamorphic Complex, where model U-Pb ages of the mineralization are given as 1180 $\pm$40 Ma (Jarvis et al 1997 [157489], p. 12).

A characterization study was undertaken to investigate the degradation of monazite and apatite and to assess the extent of uranium, thorium, and REE transport away from the primary ore body under *in situ* conditions. One of the main objectives of the study was to evaluate the role of colloids in promoting the mobilization and retardation of trace metals. The average rainfall in the area is 70 mm/yr (Jarvis et al. 1997 [157489], p. 15). Upper sections of the mine experience permanently unsaturated conditions. The steady-state level of the water table is 50 m below the surface when pumping is stopped. The pH of the waters ranges from 7.3 to 8.4 (Jarvis et al. 1997

[157489], p. 21). Analyses of waters collected from boreholes indicate supersaturation by 2 to 3 orders of magnitude with respect to amorphous uranium (UO_2) and thorium (ThO_2) phases.

There is a marked fractionation between light and heavy REEs, with the heavier elements strongly enriched in the aqueous phase (Figure 10.5-2). The heavy REEs show a greater tendency for complexation and a greater affinity for mineral surfaces (Jarvis et al. 1997 [157489]), suggesting association with colloidal particles. Given the degree of fractionation exhibited by the lanthanide series elements (REEs), finely comminuted monazite cannot represent the dominant colloidal phase. Extensive leaching and alteration of the original mineralogy must have occurred and has resulted in a phase or phases containing proportionally more uranium, thorium, and REE than the parent. A similar phenomenon has been observed at other localities where monazite weathering is accompanied by preferential loss of uranium and thorium (Jarvis et al. 1997 [157489], p. 16).

Results of the study indicate that the monazite deposit behaves as a partly open system, especially where monazite disseminated in its silicate matrix is exposed to oxidizing surface and groundwaters along fractures and stratigraphic discontinuities, such as the contact between overburden and bedrock. Under these conditions, there is evidence that colloids in the infiltrating water act as vectors for the transport of thorium, uranium, and REE. This evidence includes very high concentrations of uranium and thorium and fractionation between the heavy and light REE in samples taken from boreholes. Final results of this study are not yet available, but the information to date indicates that both the Steenskampskraal and Nopal I sites are open systems with respect to thorium, with colloidal transport being the main transport mechanism. Both sites are similar to Yucca Mountain with respect to unsaturated, oxidizing conditions. This suggests that should thorium escape waste packages emplaced at Yucca Mountain, it would likely be transported by colloids, unless attenuated by filtration.

10.5.2 Koongarra

The Koongarra uranium deposit at Alligator Rivers, Australia is found at the steeply tilted contact between Proterozoic sandstone and schist (CRWMS M&O 2000 [151945], Section 13). The ore body is located in a shallow unsaturated environment that is subject to seasonal fluctuations of monsoons. Payne et al. (1992 [124812]) investigated the role of colloids in transport of uranium in the dispersion fan of the weathered zone above the ore body. The colloids and particles included clay minerals, particularly kaolinite, and chlorite, along with fine quartz grains. Iron was present as particle coatings, and in a separate colloidal form. The amount of ^{238}U associated with colloids ranged up to 6.5%, whereas the amount of ^{230}Th associated with colloids ranged from 10% to 85%. However, ^{230}Th was associated to a much greater extent with larger particles, which are unlikely to be mobile in natural groundwaters. The high $^{227}Th/^{230}Th$ ratio was high in some fractions, indicating that ^{227}Ac could be present as colloids. Overall, however, there was little colloidal material in these groundwaters, with only iron, uranium, thorium, and actinium showing a significant association with colloids (Payne et al. 1992 [124812], p. 481).

10.6 CONCLUSIONS

The hydrogeologic and geochemical setting at Peña Blanca is closely analogous to that at Yucca Mountain, as described in Section 10.4.2 and in CRWMS M&O 2000 [141407]. While the

hydrogeologic and geochemical features at INEEL are less similar to Yucca Mountain, of the contaminated anthropogenic sites initially considered for study, INEEL provided the closest similarity in that it occurs in a fractured porous medium with perched water zones and units of varying permeability. It provided the additional advantage of data sets that included radionuclides, which strengthen model testing aspects of the analogue study. Radionuclide transport in the surficial sediment zone at the RWMC can be interpreted in a number of ways. One is that lateral flow occurred, sweeping out part of the radionuclide plume. The thickness of the stratigraphic layers is highly irregular, and the possibility exists that flow occurred along the interface between the clay layer and the surficial sediment layer. This would be in keeping with the hypothesis of Nimmo et al. 2001 [154458]). Another possibility is that a catastrophic or sudden release of a pulse of fluid caused by a flooding event released a pulse of radionuclides that propagated downward with reduced retardation, owing to kinetic effects in turn caused by fast flow rates. Presumably, according to this interpretation, the concentration peak lies at a still greater depth below that at which the data were collected.

The model calculations predict retardation factors for neptunium and uranium that are seen to be orders of magnitude higher compared to the other radionuclides. This result would indicate that very little movement of neptunium and uranium should be observed. No values for these radionuclides were reported that could be taken as consistent with their predicted high retardation.

In comparison to Yucca Mountain, the wetter environment at INEEL is manifested in higher infiltration at the SDA and flooding events that could have resulted in enhanced radionuclide migration beneath the SDA. Focused flow, resulting from the undulating topography of the basalt flows and sedimentary interbeds, would be expected to exacerbate the situation, leading to even greater distances of radionuclide migration, as demonstrated in the modeling exercises. The UZ Flow and Transport Model at Yucca Mountain considers a range of infiltration rates that are then used to bound the range of percolation flux. Because the PTn has a damping effect on flow to the TSw, it is unlikely that the enhanced transport scenario proposed in the INEEL modeling study would occur at Yucca Mountain.

At Nopal I, the evolution of stable isotopes for the adit samples appears to have at least three components: (1) evolution of vapor from the GMWL, (2) modification by water/rock interaction, and (3) evaporation in the adit collection system. A simpler approach planned for evaluation shortly is to normalize the uranium data to chloride or bromide concentrations. It is estimated that the transit time for the seep water that infiltrated into the Nopal I Level +00 adit 8 m below surface is about 6–29 days, and for the perched water at 10.7 m depth in an old borehole, the transit time is about 0.4–0.5 years. The large values of τ_W for the perched water may reflect the long residence time of water in the borehole. It should be noted that as water at different sites may have different pathways, the value of τ_W itself does not provide information on possible connections between the perched and seep waters sampled. In conclusion, although the water transit time in the UZ is quite short, significant dissolution of uranium may have occurred in a low-water flux, high-uranium concentration setting near the Nopal I uranium deposit. If analyses from future sampling campaigns confirm that transit time is short in the UZ at Nopal I, then the implications would need to be considered for the similar low-water flux environment at Yucca Mountain.

Compared with samples collected during the September wet season of 1995, many of the new measurements in late February 2000, and again in early March 2001, show much higher ^{238}U concentration and lower ^{234}U/^{238}U, suggesting increased uranium dissolution and/or lower α-recoil-associated ^{234}U enrichment rates during the dry seasons. The low humidity during dry seasons may have also enhanced evaporation, causing higher uranium concentrations in the waters sampled.

The data collected during the winter dry seasons of 2000 and 2001 depart considerably from the linear relationship between ^{234}U/^{238}U and $1/^{238}$U predicted by the model for the wet season of 1995 (Figure 10.4-5a). Such a departure could be caused by: (1) high and variable evaporation under low humidity conditions, and (2) incomplete flushing associated with low rainfall during the dry season. The uranium dissolution rates are about three times higher than those in the wet season, possibly suggesting a favorable physiochemical condition (e.g., increased oxygenation) for uranium dissolution during dry periods.

Large variations in the ^{238}U concentration and ^{234}U/^{238}U ratio were also found in samples collected from the SZ during the dry season. Both the decreased water infiltration flux and the increased uranium dissolution rates in the vadose zone may contribute to the higher dry-season uranium concentrations in the SZ. Observations such at these may have important implications for the effects of climate change on the long-term stability of uranium in the environment.

As a final point, colloid transport appears to be an important factor for migration of thorium in one open unsaturated system, Steenkampskraal, but not in another, Nopal I. Both systems have similar hydrologic conditions to those at Yucca Mountain, although the rock type is different at Steenkampskraal. At Koongarra, another unsaturated but seasonally fluctuating system, colloid transport takes place but is a minor mechanism of uranium transport. Because seasonal fluctuations in uranium dissolution have been discovered at Nopal I, it would be useful to investigate the possibility of colloid transport in that system. A more informed understanding of the implication for colloid transport in the UZ at Yucca Mountain could then be had and could be used to evaluate whether TSPA assumptions that disregard colloid filtration are appropriately conservative.
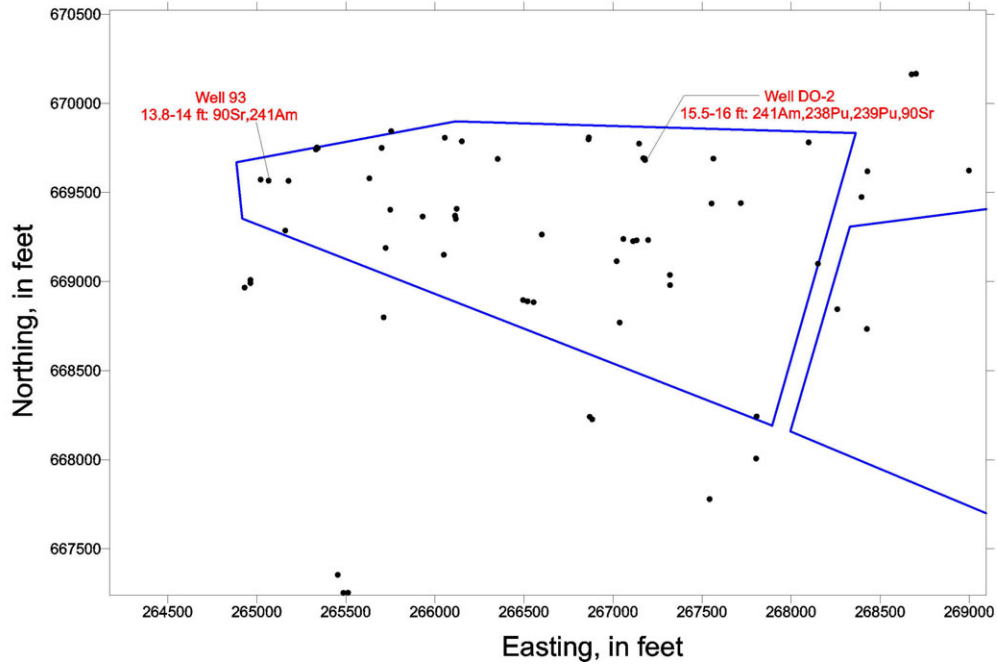
Source: Simmons 2002 [157578], SN-LANL-SCI-234-V1, p. 61.

Figure 10.3-1a. Map of SDA and Deep Wells Showing Location of Radionuclide Concentrations Greater Than Three Times Detection for Depth Intervals to the 9 m Interbed
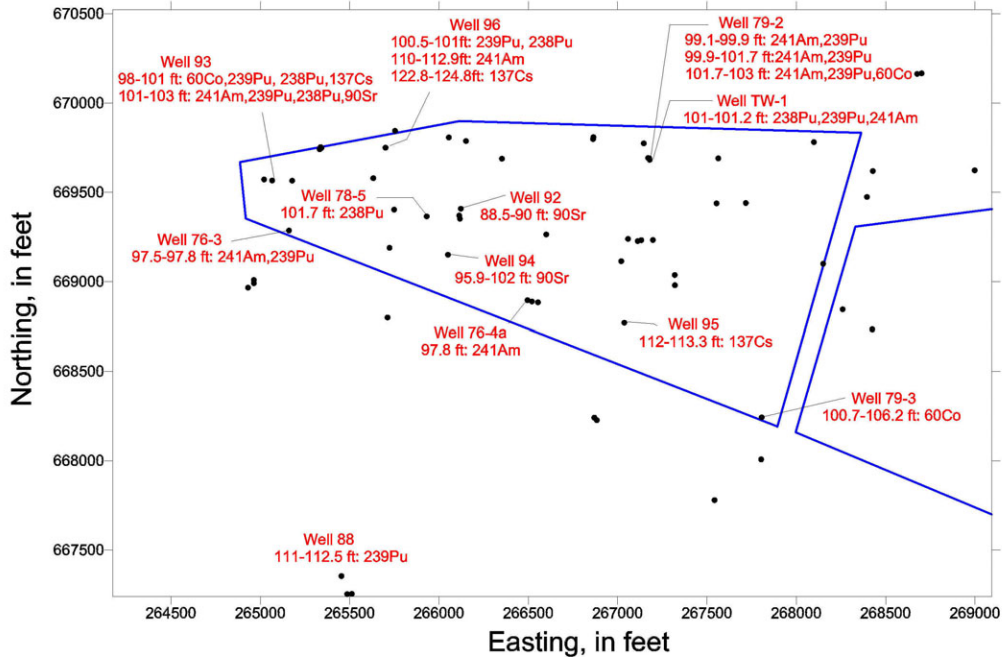
Source: Simmons 2002 [157578], SN-LANL-SCI-234-V1, p. 61.

Figure 10.3-1b. Map of SDA and Deep Wells Showing Location of Radionuclide Concentrations Greater Than Three Times Detection for Depth Intervals to the 34 m Interbed
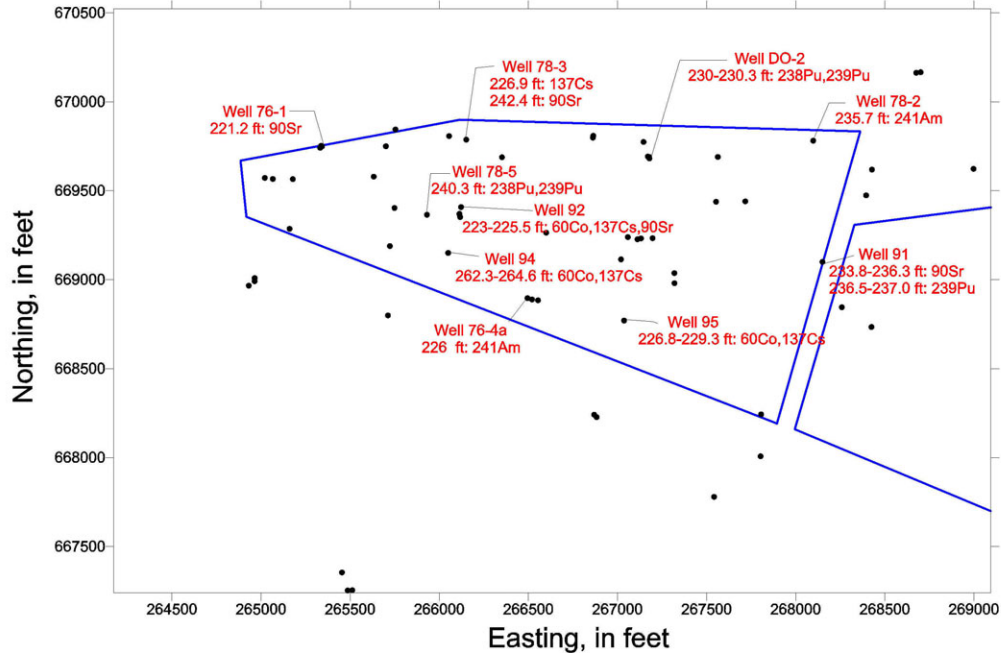
Source: Simmons 2002 [157578], SN-LANL-SCI-234-V1, p. 62.

Figure 10.3-1c. Map of SDA and Deep Wells Showing Location of Radionuclide Concentrations Greater Than Three Times Detection for Depth Intervals to the 73 m Interbed
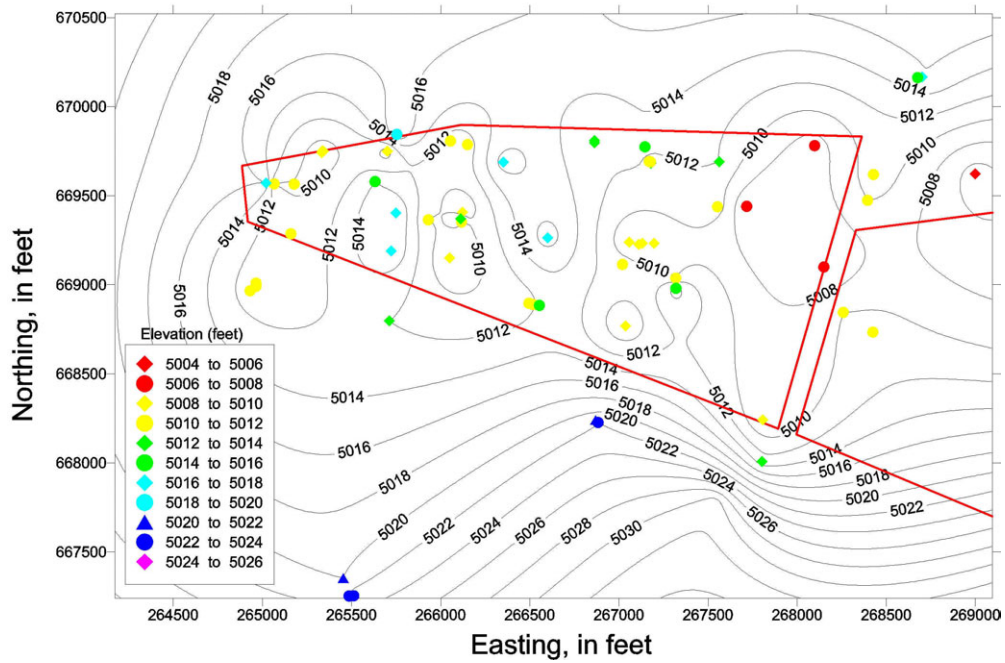
Source: Simmons 2002 [157578], SN-LANL-SCI-234-V1, p. 63.

Figure 10.3-2. Ground Surface Elevation in the Vicinity of the SDA
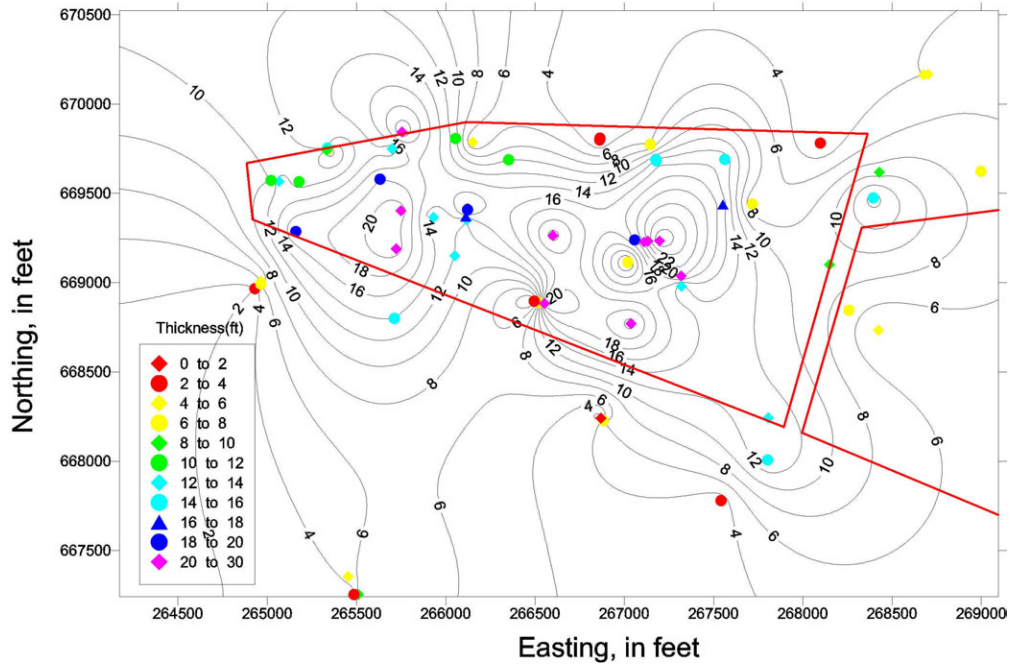
Source: Simmons 2002 [157578], SN-LANL-SCI-234-V1, p. 64.

Figure 10.3-3.   Surficial Sediment Thickness in the Vicinity of the SDA
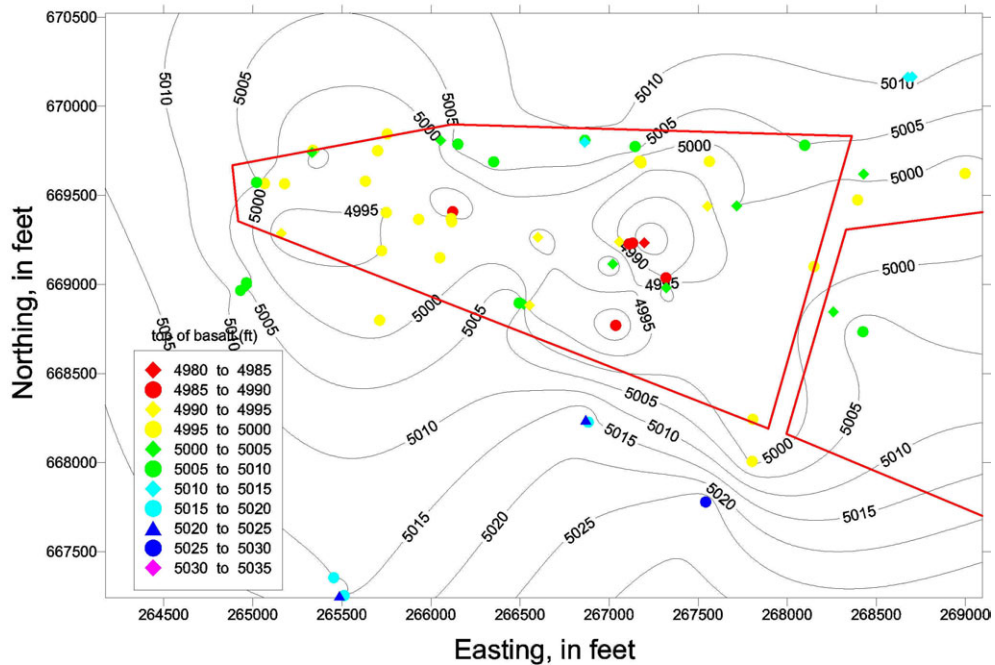
Source: Simmons 2002 [157578], SN-LANL-SCI-234-V1, p. 64.

Figure 10.3-4. Elevation of Top of Basalt Flow A in the Vicinity of the SDA
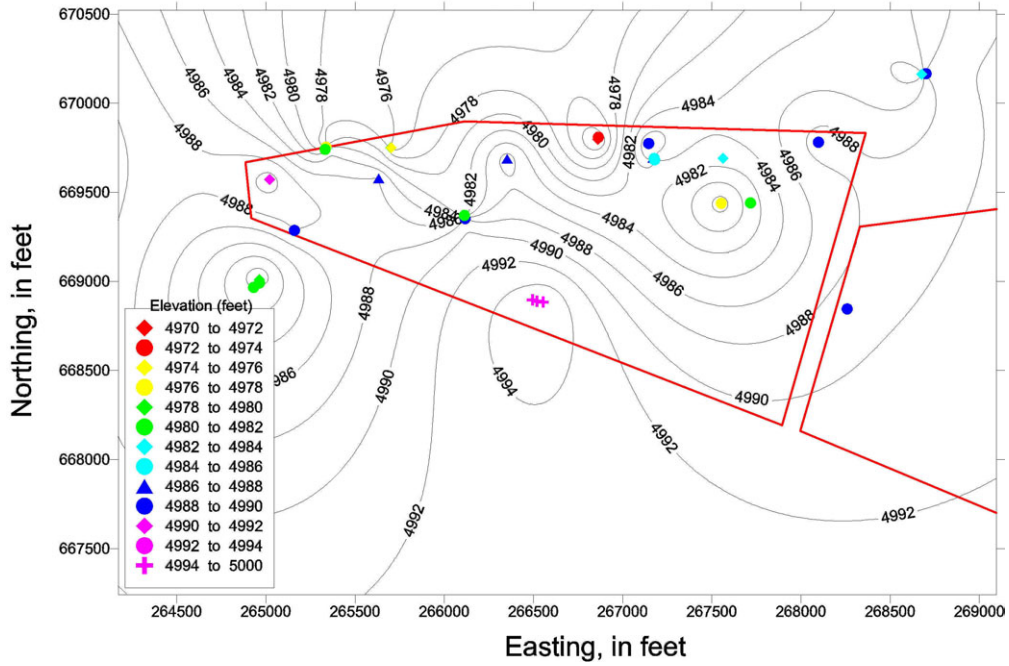
Source: Simmons 2002 [157578], SN-LANL-SCI-234-V1, p. 65.

Figure 10.3-5. Elevation of Top of AB Interbed in the Vicinity of the SDA
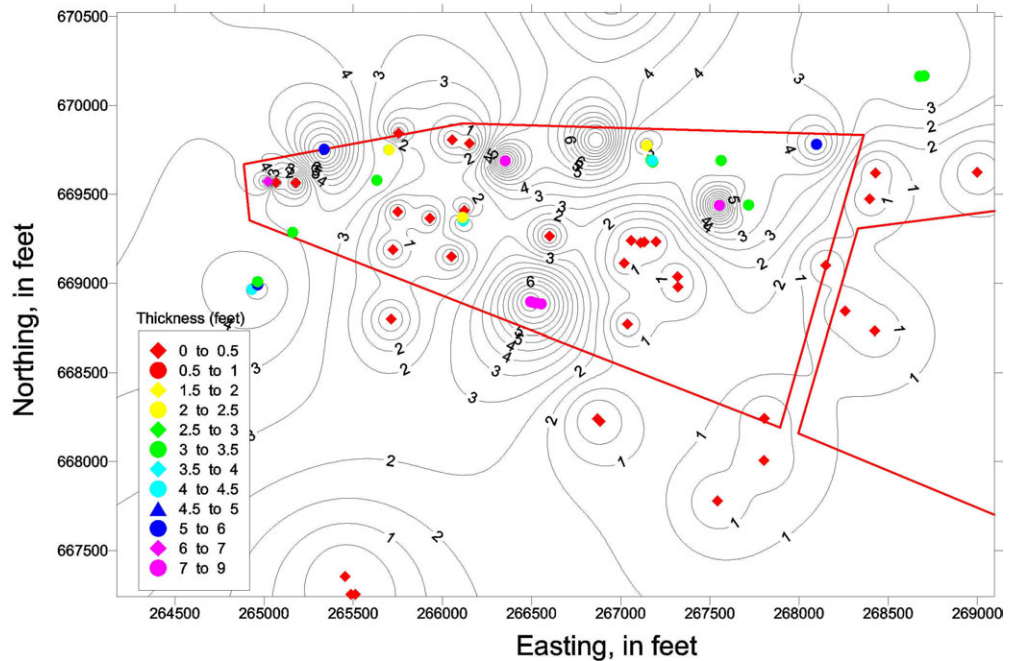
Source: Simmons 2002 [157578], SN-LANL-SCI-234-V1, p. 65.

Figure 10.3-6. Thickness of AB Interbed in the Vicinity of the SDA
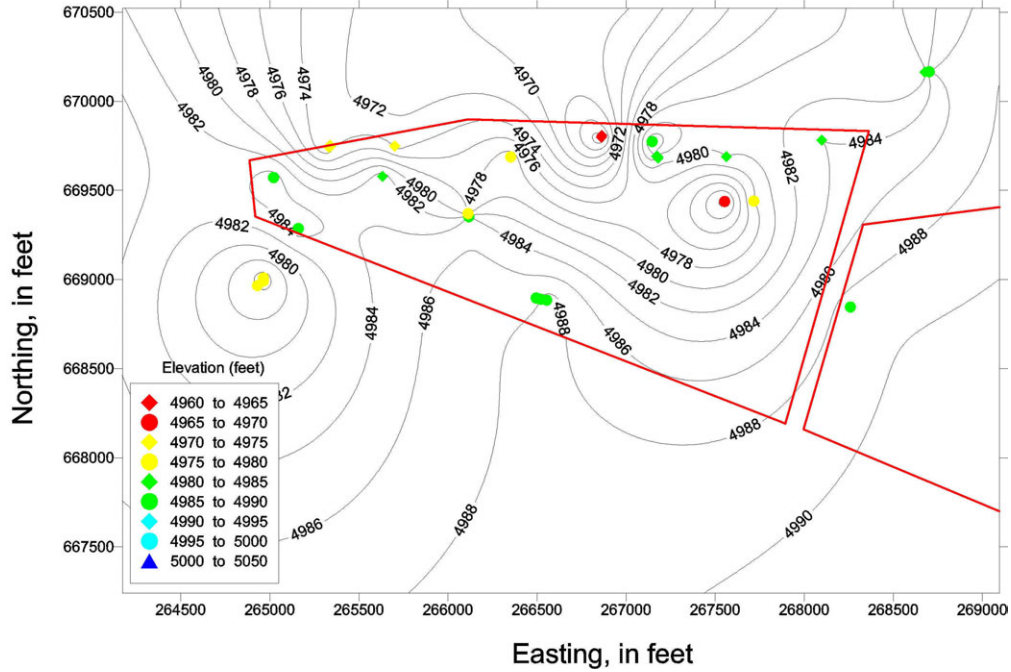
Source: Simmons 2002 [157578], SN-LANL-SCI-234-V1, p. 66.

Figure 10.3-7. Elevation of Top of B Basalt in the Vicinity of the SDA
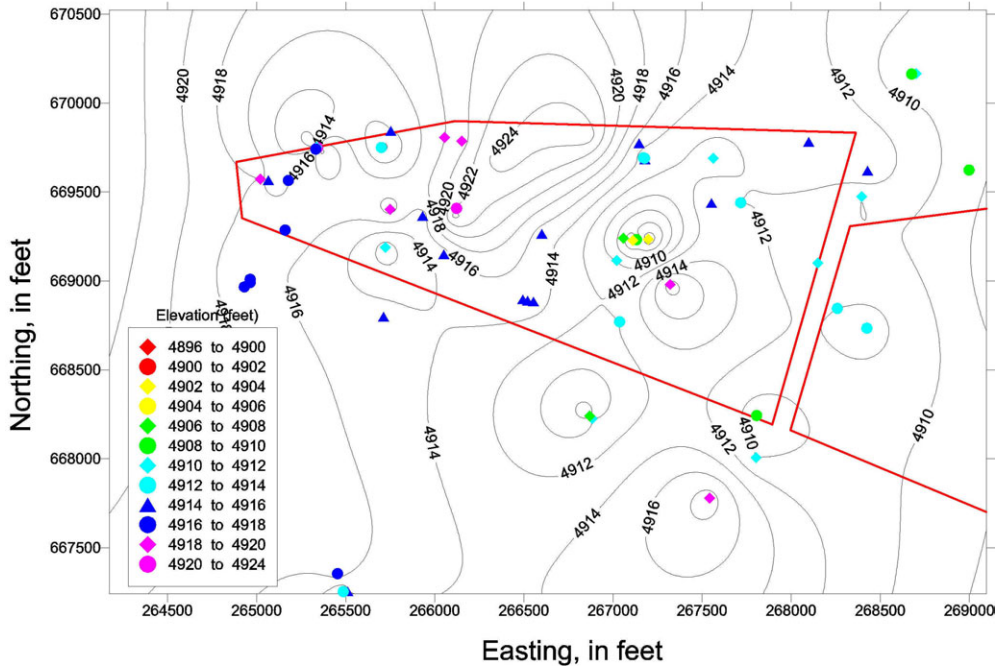
Source: Simmons 2002 [157578], SN-LANL-SCI-234-V1, p. 66.

Figure 10.3-8. Elevation of Top of BC Interbed in the Vicinity of the SDA
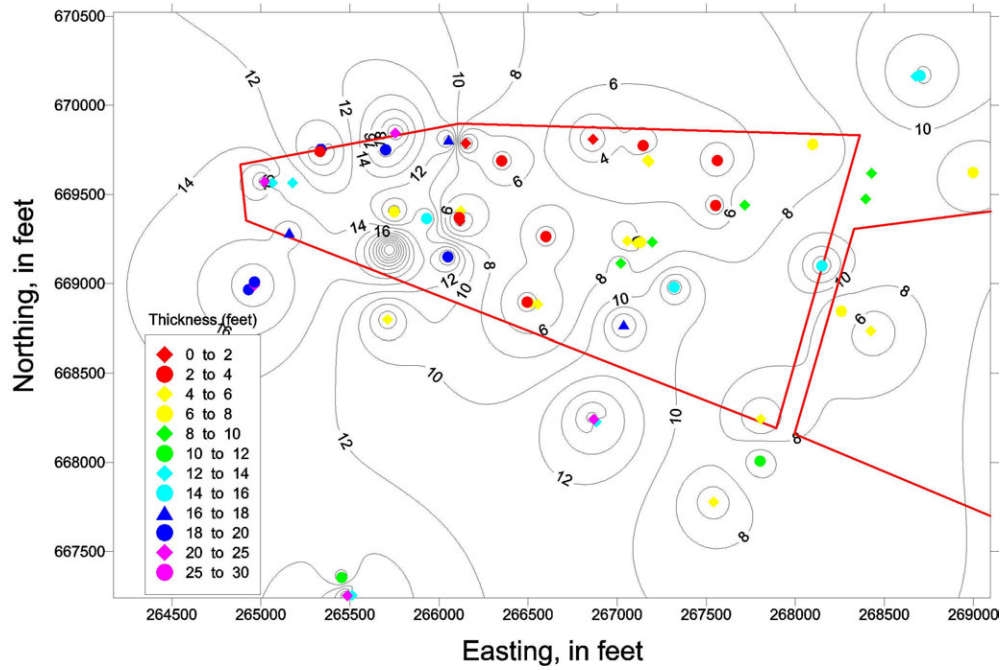
Source: Simmons 2002 [157578], SN-LANL-SCI-234-V1, p. 67.

Figure 10.3-9. Thickness of BC Interbed in the Vicinity of the SDA
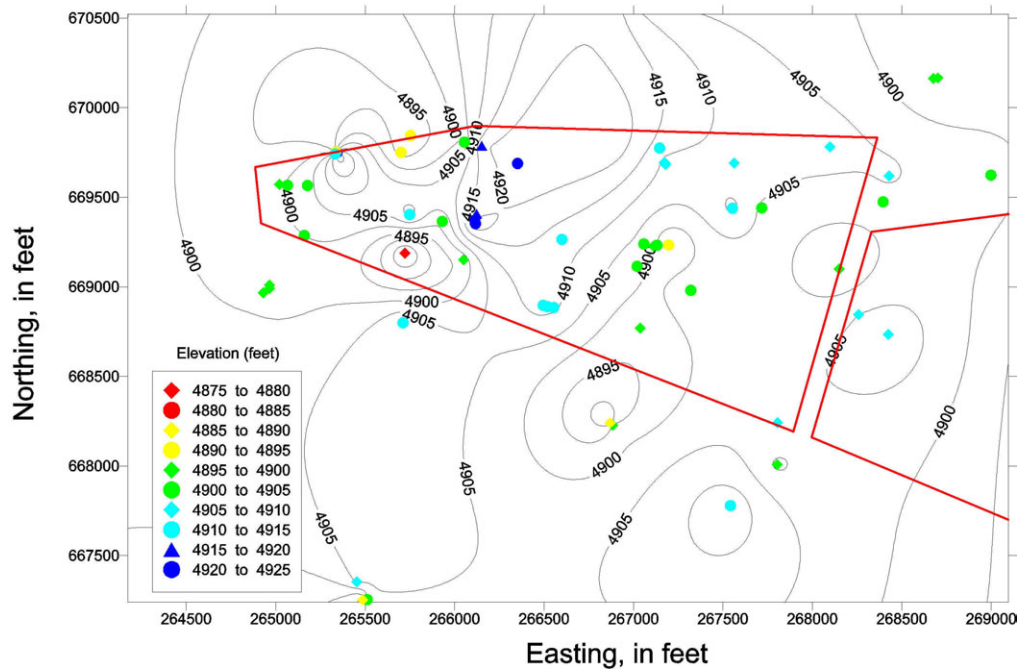
Source: Simmons 2002 [157578], SN-LANL-SCI-234-V1, p. 67.

Figure 10.3-10. Elevation of Top of C Basalt in the Vicinity of the SDA
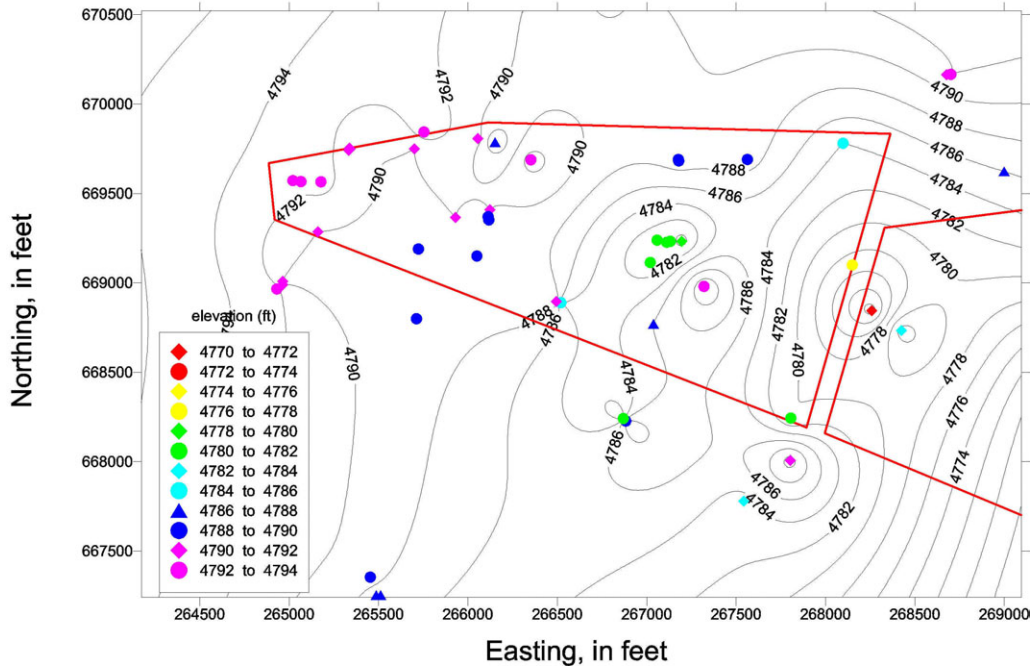
Source: Simmons 2002 [157578], SN-LANL-SCI-234-V1, p. 68.

Figure 10.3-11. Elevation of Top of CD Interbed in the Vicinity of the SDA
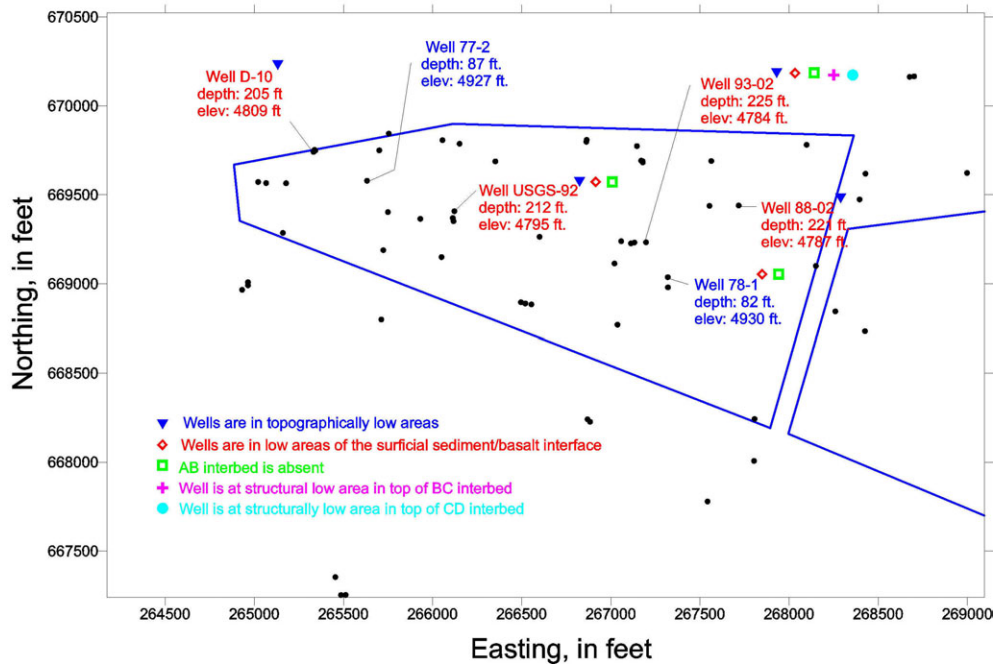
Source: Simmons 2002 [157578], SN-LANL-SCI-234-V1, p. 75.

Figure 10.3-12. Depths and Elevations of Perched Water in the Vicinity of the SDA
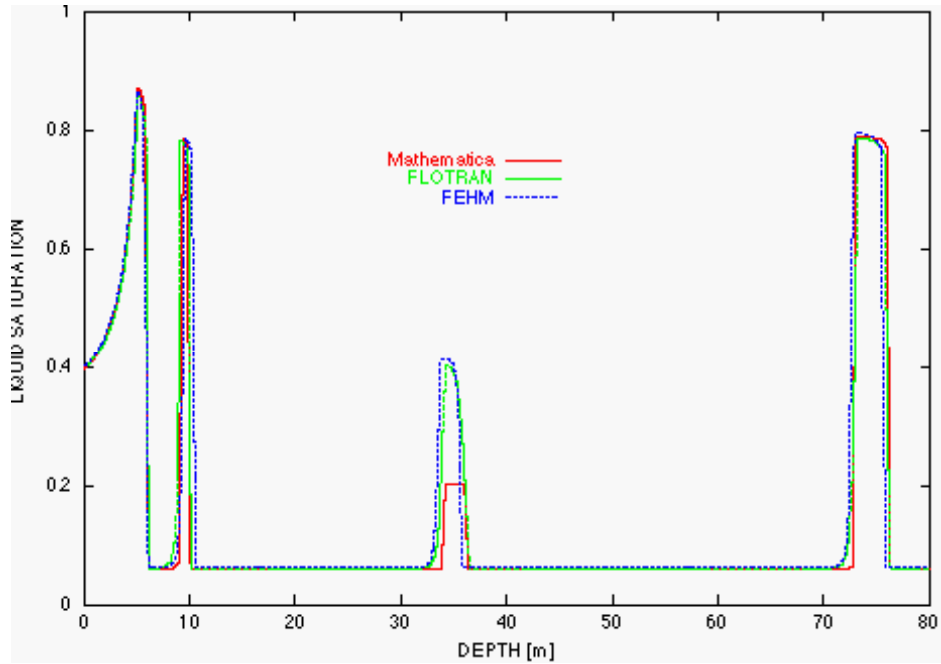
Source: Simmons 2002 [157578], SN-LANL-SCI-234-V1, p. 16.

Figure 10.3-13. Comparison of Steady-State Saturation Profiles for FEHM and FLOTRAN for Single-Continuum Simulation
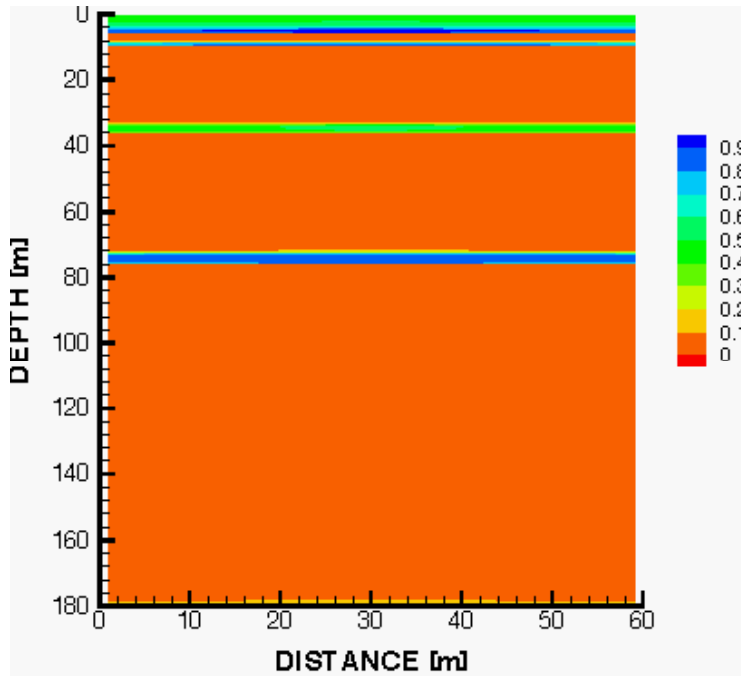
Source: Simmons 2002 [157578], SN-LANL-SCI-234-V1, p. 20.

Figure 10.3-14. Liquid Saturation for the Single-Continuum Simulation
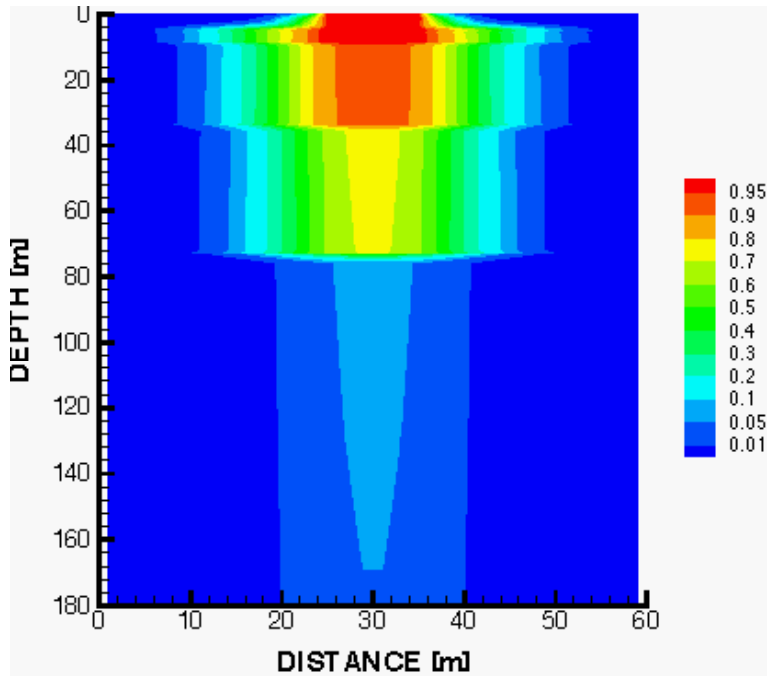
Source: Simmons 2002 [157578], SN-LANL-SCI-234-V1, p. 23.

Figure 10.3-15a. Normalized Tracer Concentration after 50 Years for the Single-Continuum Model with Constant Release
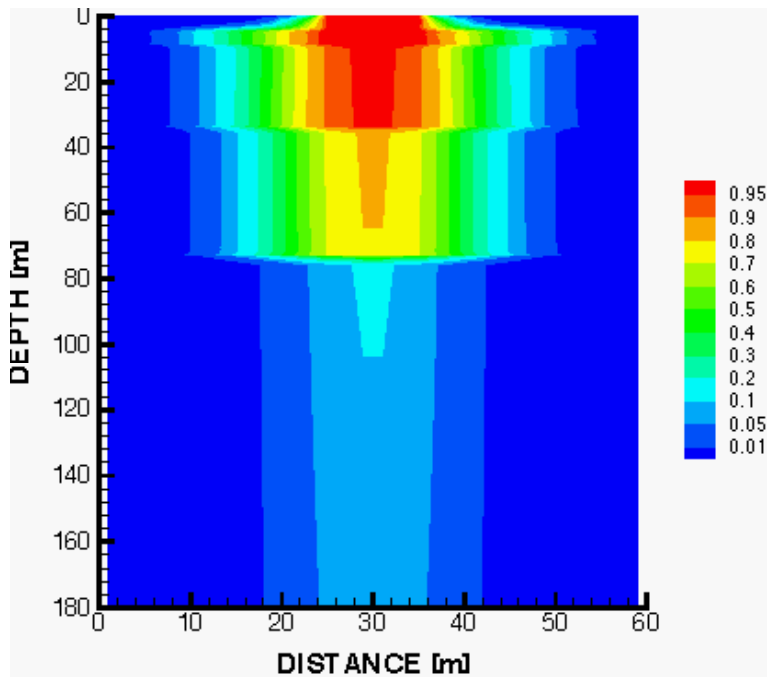
Source: Simmons 2002 [157578], SN-LANL-SCI-234-V1, p. 23.

Figure 10.3-15b. Normalized Tracer Concentration after 50 years for the Single-Continuum Model with Pulse Release
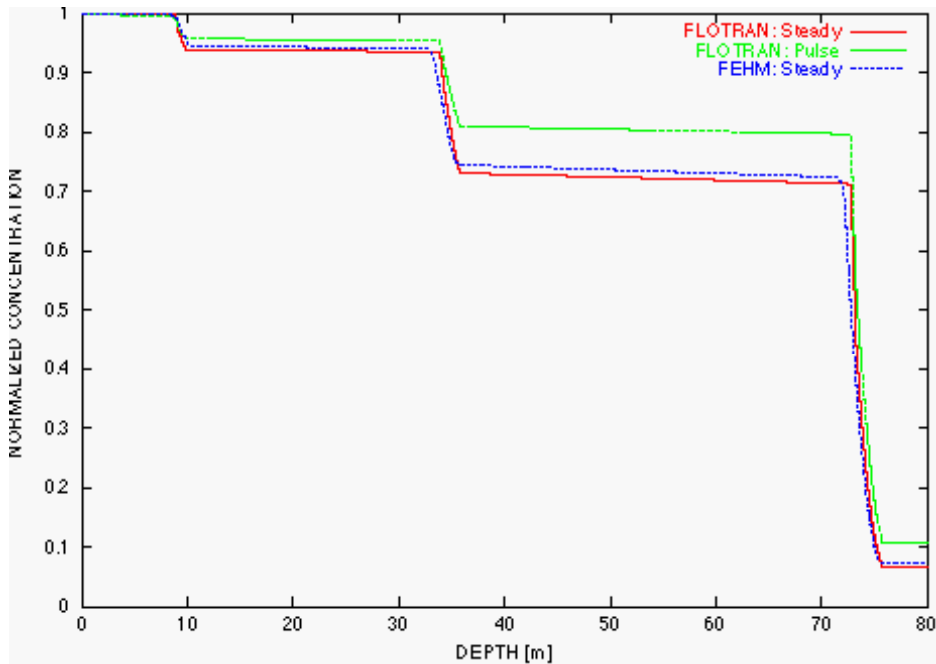
NOTE: Also Shown is the Pulse Release using FLOTRAN.

Source: Simmons 2002 [157578], SN-LANL-SCI-234-V1, p. 24.

Figure 10.3-16. Comparison of FEHM and FLOTRAN for Normalized Tracer Concentration after 50 Years for the Single-Continuum Model with Steady Release at the Center of the Injection Region
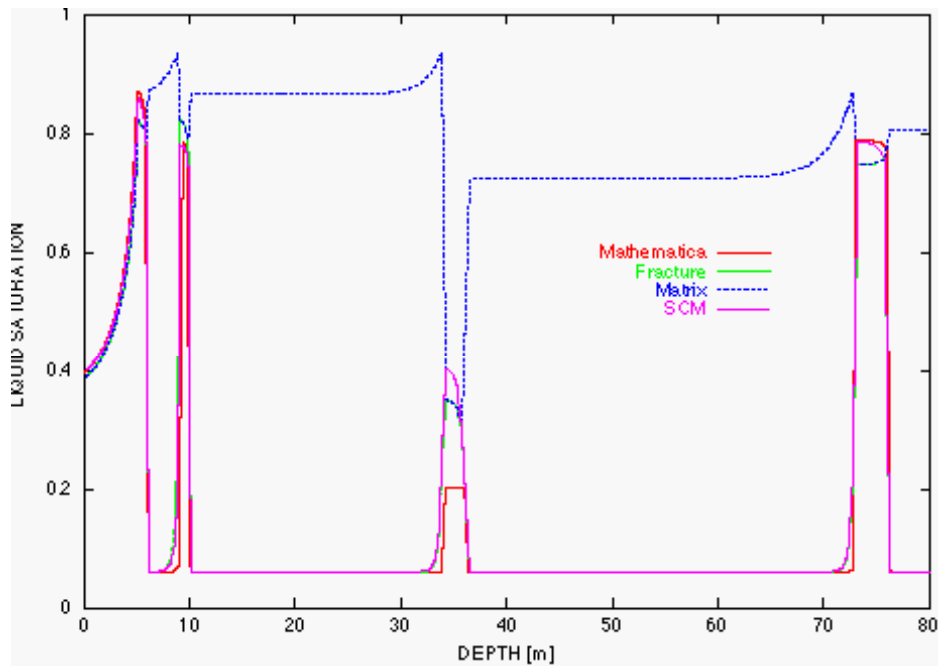
Source: Simmons 2002 [157578], SN-LANL-SCI-234-V1, p. 24.

Figure 10.3-17. Comparison of Steady-State Saturation Profiles for Single- and Dual-Continuum Simulations
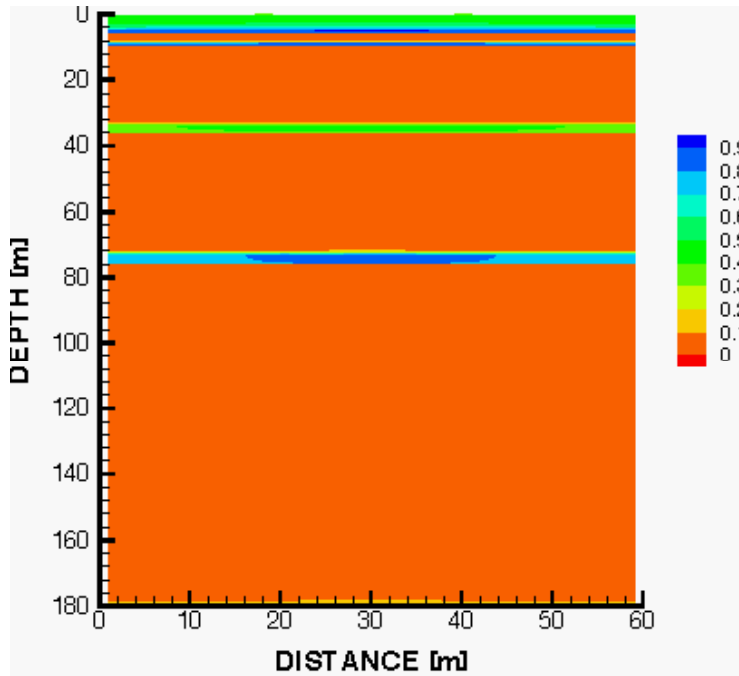
Source: Simmons 2002 [157578], SN-LANL-SCI-234-V1, p. 26.

Figure 10.3-18a. Liquid Saturation for Fracture Continuum
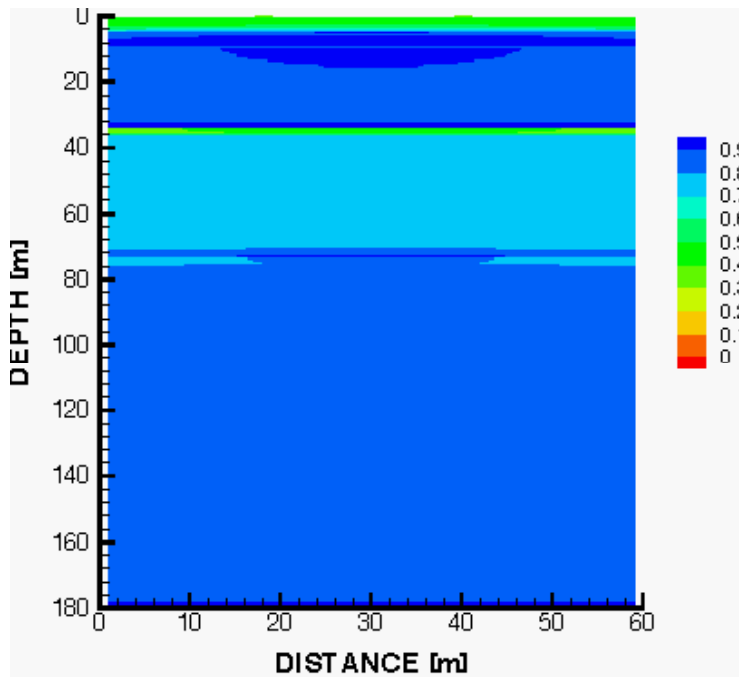
Source: Simmons 2002 [157578], SN-LANL-SCI-234-V1, p. 26.

Figure 10.3-18b. Liquid Saturation for Matrix Continuum
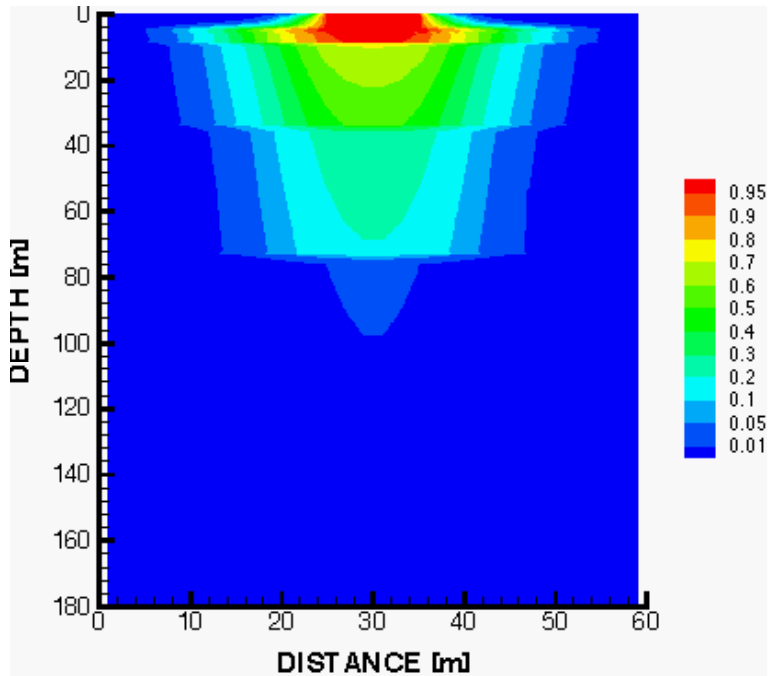
Source: Simmons 2002 [157578], SN-LANL-SCI-234-V1, p. 27.

Figure 10.3-19a. Normalized Tracer Concentration for Fracture Continuum
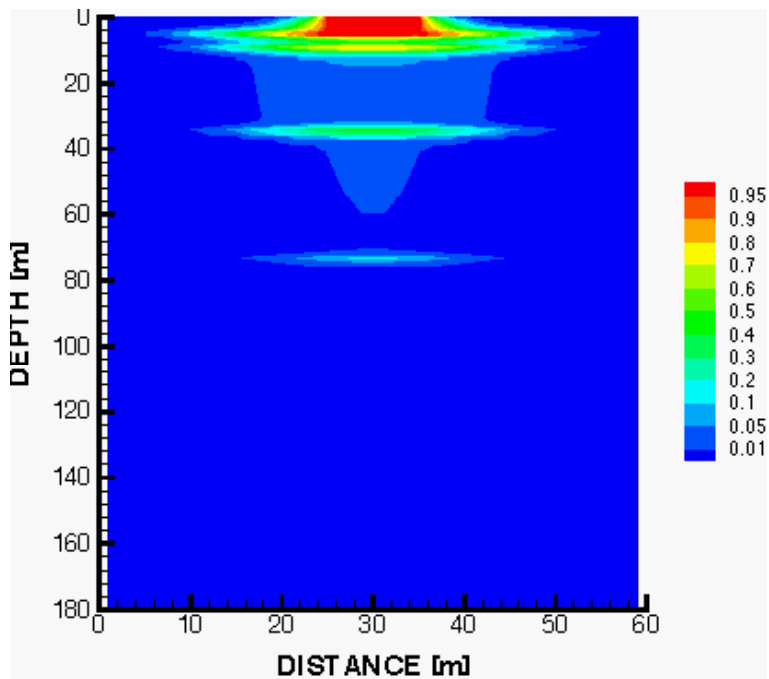
Source: Simmons 2002 [157578], SN-LANL-SCI-234-V1, p. 27.

Figure 10.3-19b. Normalized Tracer Concentration for Matrix Continuum
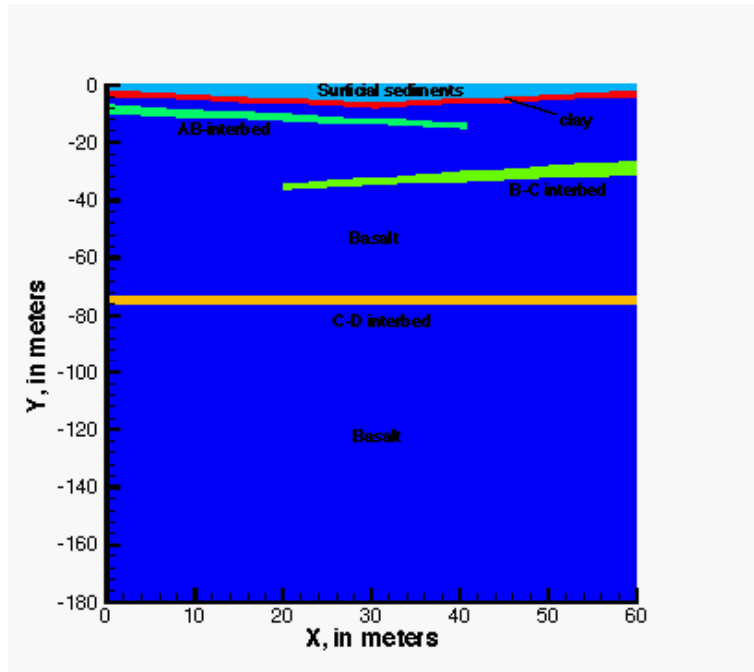
Source: Simmons 2002 [157578], SN-LANL-SCI-234-V1, p. 76.

Figure 10.3-20. Hydrostratigraphy
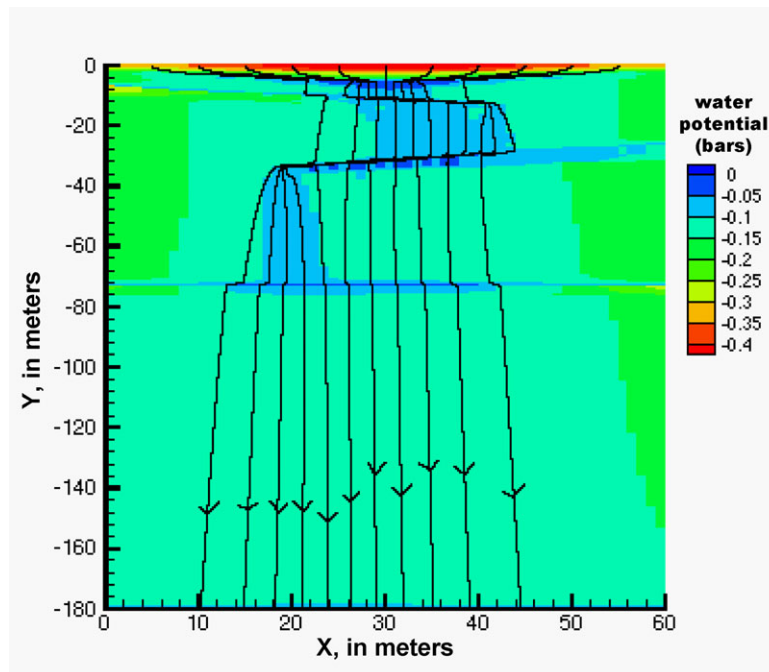
NOTE: Arrows indicate particle-tracking flow lines.

Source: Simmons 2002 [157578], SN-LANL-SCI-234-V1, p. 83.

Figure 10.3-21. Steady-State Water Potentials
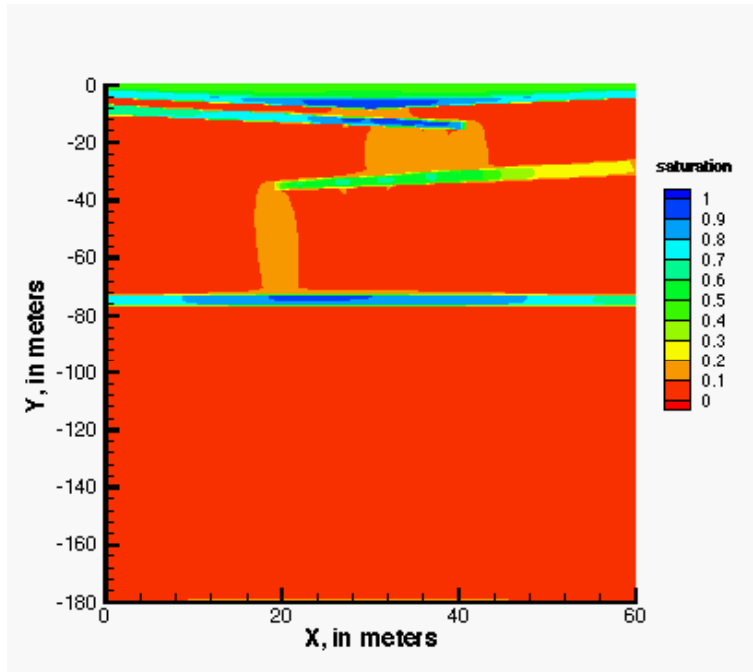
Source: Simmons 2002 [157578], SN-LANL-SCI-234-V1, p. 88.

Figure 10.3-22. Liquid Saturation at 50 Years
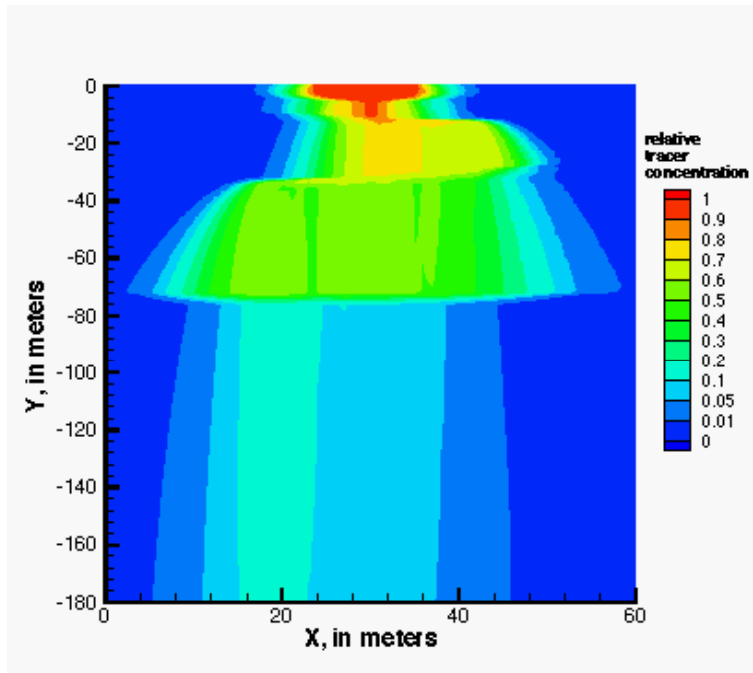
Source: Simmons 2002 [157578], SN-LANL-SCI-234-V1, p. 89.

Figure 10.3-23. Normalized Tracer Concentration at 50 Years
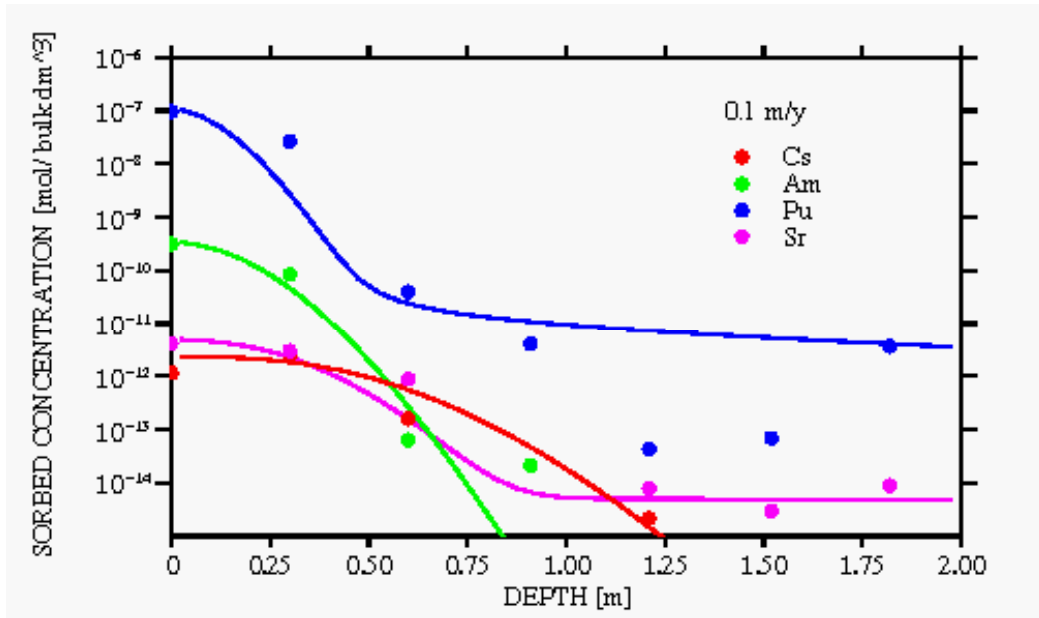
Source: Simmons 2002 [157578], SN-LANL-SCI-234-V1, p. 30.

Figure 10.3-24.   Comparison of Field Data for Sorption of Cs, Pu, Am, and Sr for a Flow Velocity of 0.1 m/yr through the Surficial Sediment
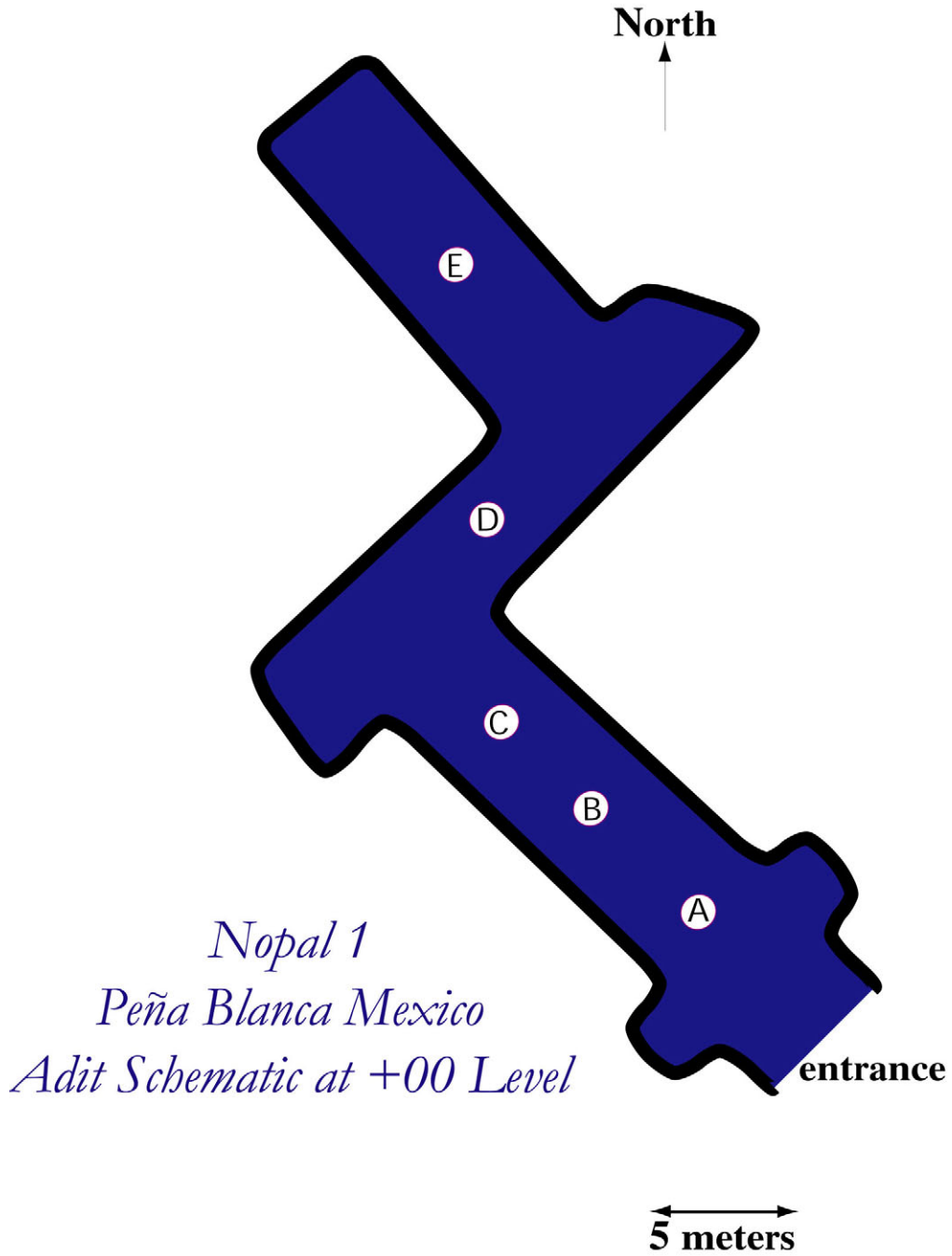
DTN: LB0202PBANALOG.001 [157610]

Figure 10.4-1. Schematic of Level +00 Adit Sampling Locations

DTN: LB0202PBANALOG.001 [157610]

Figure 10.4-2. Photo of Sampling Locations A, B, and C in the Nopal I +00 Adit
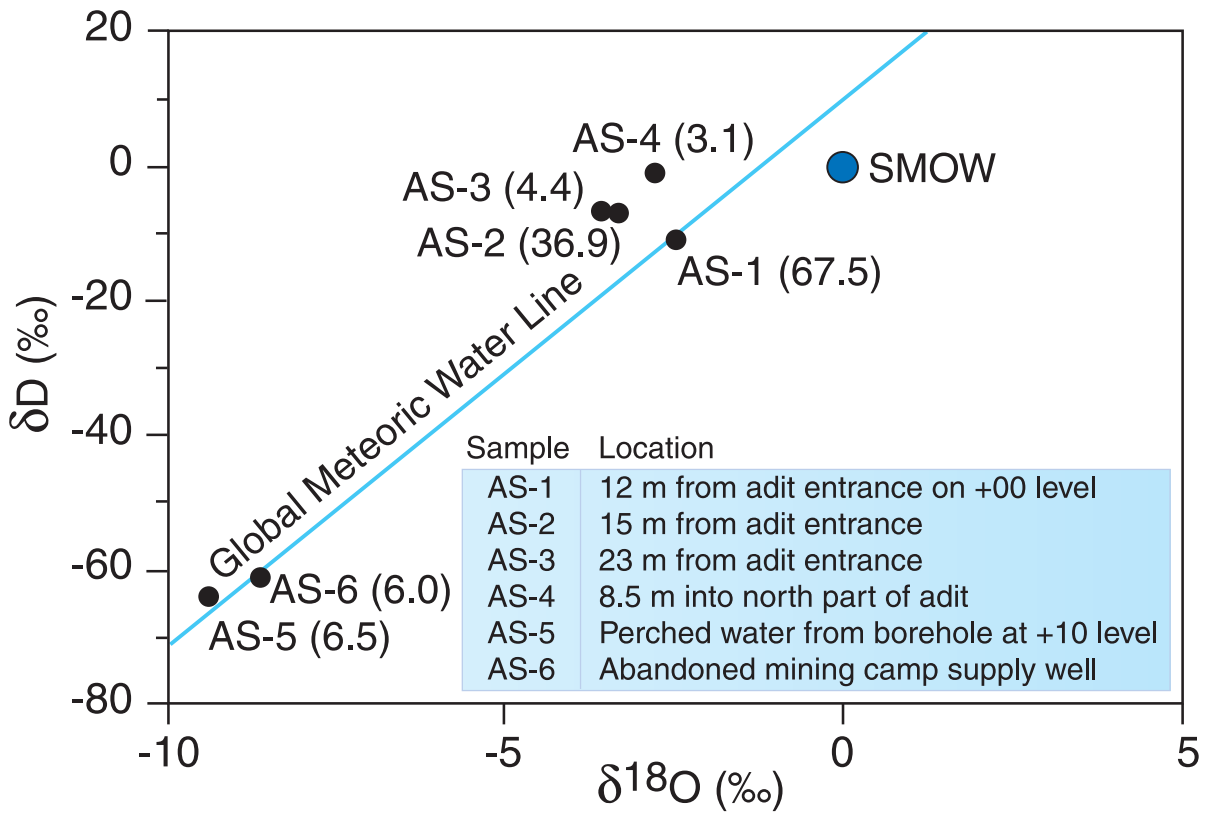
DTN: LB0202PBANALOG.001 [157610]

NOTE: Also shown is the position of the global meteoric water line and SMOW (Standard Mean Ocean Water).

Figure 10.4-3. Plot of δD versus δ¹⁸O for water samples collected (black circles) from Peña Blanca during February 2000
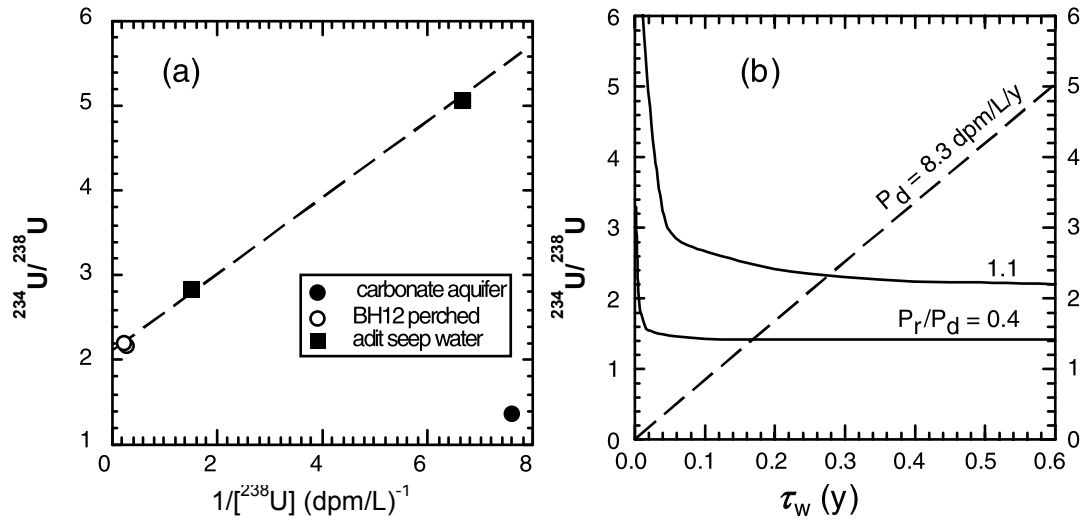
NOTE: The dashed line in (a) delineates the positive linear correlation for waters sampled from the UZ. Its slope and intercept can be used to derive P_r (input from recoil) and P_d (input from dissolution) by the model. (b) shows a rapid decrease of $^{234}U/^{238}U$ to a relatively constant level within a couple of weeks after the water enters the UZ. The low $^{234}U/^{238}U$ activity ratio of 1.39 in the carbonate aquifer as shown in (a) requires a P_r/P_d ratio of about 0.4, about three times smaller than that in the UZ.

$(dpm/L)^{-1}$ values calculated from data in Table 10.4-1, using half-lives of ^{234}U and ^{238}U.

Source: Modified from Pickett and Murphy 1999 [110009], Figure 15.

Figure 10.4-4. (a) $^{234}U/^{238}U$ Activity Ratio vs. Reciprocal ^{238}U Activity in Nopal I Waters and (b) $^{234}U/^{238}U$ Activity Ratio (solid lines) and ^{238}U Concentration (dashed line) as a Function of Water Transit Time (τ_w) in the UZ
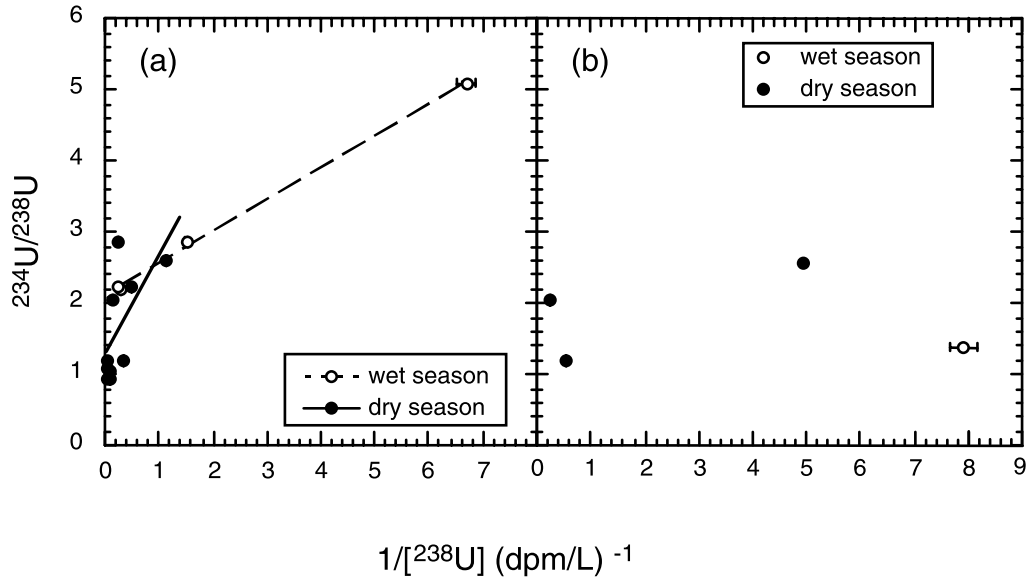
NOTE: Solid and dashed lines in (a) are linear regressions for samples collected during the dry (February 2000 and March 2001 collections) and wet (August - September of 1995) seasons, respectively. Dissolution of uranium is higher during the dry periods.

Source: Data values calculated from data in Table 10.4-1, using half-lives of ^{234}U and ^{238}U.

Figure 10.4-5. ^{234}U/^{238}U Activity Ratio vs. Reciprocal ^{238}U Activity in Nopal I Waters from (a) UZ and (b) SZ

Source: Jarvis et al. 1997 [157489], Figure 1.

Figure 10.5-1. Location of Steenkampskraal, South Africa
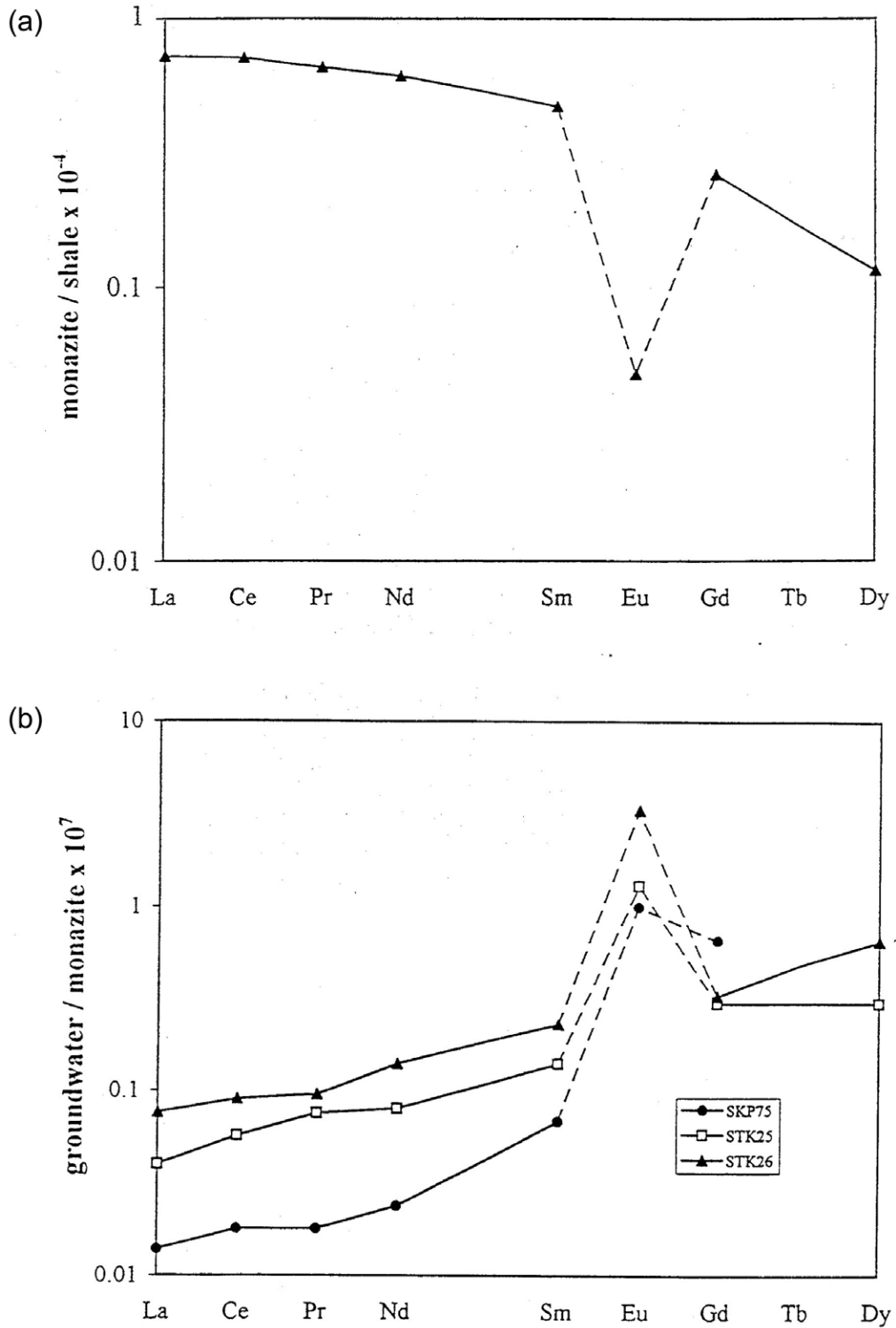
Source: Jarvis et al. 1997 [157489], Figures 3 and 4.

Figure 10.5-2.   (a) Shale-normalized REE Pattern for Steenkampskraal Monazites and (b) REE
               Distribution for Groundwater Samples Normalized to Average Steenkampskraal Monazite

Table 10.3-1. Chemical Characteristics of Selected Samples of Pore Water, Perched Water, and Groundwater from Yucca Mountain and the Subsurface Disposal Area of INEEL

	Location	Temp. (°C)	pH	Ca (mg/L)	Mg (mg/L)	Na (mg/L)	K (mg/L)	Cl (mg/L)	SO$_4$ (mg/L)	HCO$_3$ (mg/L)	SiO$_2$ (mg/L)	F (mg/L)	NO$_3$ (mg/L)	Data Source
Yucca Mountain	UZ-14 pore water (CHn)	28*	8.7	1.2	0.2	155	—	16	14	160	72.0	—	4	A
	UZ-14 perched water	25*	7.8	31	2.5	35	4.1	7.0	24.2	146.4	40.7	—	17.1	B
	WT-3 saturated zone	31.8	7.6	11.2	1.0	49.0	3.9	6.0	18.3	138.5	56.0	2.3	5.7	C
INEEL	Borehole W02 Lysimeter W0L01	5 to 10*	8.1	46.1	15	188	1.5	27	133	508	—	0.2	—	D
	Well 92 perched water (10/29/76)	13.5	8.4	29	17	120	12	81	64	290	22	0.4	—	E
	RWMC production well saturated zone	13	8.1	45	15	9.0	2.8	13	27	180.4	28	0.2	3.0	F

NOTE: *estimated temperature

Sources: A = Yang et al. 1996 [100194], Table 3, sample UZ-14/1563.6–1563.8/up1,2,3.
B = Yang et al. 1996 [100194], Table 6, sample UZ-14D.
C = DTN: GS980908312322.008 [145412].
D = Dicke 1997 [157410], Table 5.
E = Rightmire and Lewis 1987 [156441], Table 13, sample of 10/29/1976.
F = USGS 2000 [157415], Table 4-2.

Table 10.3-2.   Additional Water Inputs to the Waste-Disposal Area Due to Flooding

Year	Infiltration Rate (m/day)	Total Equivalent Depth of Infiltrating Water (m)
1962	1.66×10^{-2}	0.166
1969	1.24×10^{-2}	0.124
1982	7.49×10^{-3}	0.075

Source: Magnuson and Sondrup 1998 [156431], Table 2-3.

Table 10.3-3.   Hydrologic Properties Used in the One- and Two-Dimensional Single-Continuum and Dual-Permeability Models

Layer	Depth (m)	Porosity	Permeability (m^2)	Residual Saturation, S_{wr}	Pore-size Distribution, λ	Air Entry Parameter, α (Pa^{-1})
Surficial sediments	0-5	0.50	6.8×10^{-13}	0.194	0.401	1.642×10^{-4}
Clay layer	5-6	0.05	1.0×10^{-15}	0.246	0.273	1.817×10^{-4}
A-basalt	6-9	0.01	2.5×10^{-12}	0.010	0.500	4.094×10^{-4}
AB (9 m) interbed	9-10	0.57	1.0×10^{-15}	0.246	0.273	1.817×10^{-4}
B-basalt	10-34	0.01	2.5×10^{-12}	0.010	0.500	4.094×10^{-4}
BC (34 m) interbed	34-36	0.48	4.0×10^{-15}	0.083	0.273	3.270×10^{-4}
C-basalt	36-73	0.01	2.5×10^{-12}	0.010	0.500	4.094×10^{-4}
CD (73 m) interbed	73-76	0.57	4.0×10^{-15}	0.246	0.273	1.817×10^{-4}
D-basalt	76-180	0.01	2.5×10^{-12}	0.010	0.500	4.094×10^{-4}
Basalt matrix		0.14	5.0×10^{-17}	0.066	0.322	3.917×10^{-5}

NOTE: λ and α are pore-size distribution and air-entry parameters in the van Genuchten (1980 [100610]) moisture characteristic functions (see Lichtner 2001 [156429]).

Source: Simmons 2002 [157578], SN-LANL-SCI-234-V1, p. 22.

Table 10.3-4. Sorption Reaction Stoichiometry and Parameter Values for a Nonelectrostatic Description of Surface Complexation Reactions

Surface Complex Reaction					log K	z
Iron oxide						
>FeO$^-$	1 >FeOH	-1 H$^+$			8.930	-1
>FeOH$_2^+$	1 >FeOH	1 H$^+$			-7.290	1
>FeOAm^{++}	1 >FeOH	-1 H$^+$	1 Am^{+++}		-1.240	2
>FeOAm(OH)$_2$	1 >FeOH	-3 H$^+$	1 Am^{+++}	2 H$_2$O	15.29	0
>FeOHPuO^{++}	1 >FeOH	1 H$^+$	1 PuO$_2^+$	-0.25 O$_2$(aq) -0.5 H$_2$O	-2.010	2
>FeOHPuO$_2$	1 >FeOH	-1 H$^+$	1 PuO$_2^+$	-0.25 O$_2$(aq) 0.5 H$_2$O	6.210	0
>FeOHPuO$_2^+$	1 >FeOH	1 PuO$_2^+$			-4.790	1
>FeOHPuO$_3^-$	1 >FeOH	-2 H$^+$	1 PuO$_2^+$	1 H$_2$O	10.66	-1
>FeOHUO$_3$	1 >FeOH	-2 H$^+$	1 UO$_2^{++}$	1 H$_2$O	3.050	0
>FeOHUO$_2^{++}$	1 >FeOH	1 UO$_2$++			-6.630	2
>FeOHNpO$_2^+$	1 >FeOH	1 NpO$_2^+$			-4.320	1
>FeOHNpO$_3^-$	1 >FeOH	-2 H$^+$	1 NpO$_2^+$	1 H$_2$O	11.26	-1
>FeOSr$^+$	1 >FeOH	-1 H$^+$	1 Sr^{++}		5.3	-1
>FeOSrOH	1 >FeOH	-2 H$^+$	1 Sr^{++}	1 H$_2$O	14.14	-1
Aluminosilicate						
>SiO$^-$	1 >SiOH	-1 H$^+$			7.200	-1
>SiOPuO$^+$	1 >SiOH	2 H$^+$	1 PuO$_2^+$	-0.25 O$_2$(aq) -0.5 H$_2$O	2.600	1
>SiOPuO$_2$	1 >SiOH	-1 H$^+$	1 PuO$_2^+$		6.430	0
>SiOPuO$_3$H$^-$	1 >SiOH	-2 H$^+$	1 PuO$_2^+$	1 H$_2$O	14.80	-1
>SiOUO$_3$H	1 >SiOH	-2 H$^+$	1 UO$_2^{++}$	1 H$_2$O	5.180	0
>SiOUO$_3^-$	1 >SiOH	-3 H$^+$	1 UO$_2^{++}$		12.35	-1
>SiONpO$_2$	1 >SiOH	-1 H$^+$	1 NpO$_2^+$		3.720	0
>SiONpO$_3$H$^-$	1 >SiOH	-2 H$^+$	1 NpO$_2^+$	1 H$_2$O	12.16	-1
>SiOAm^{++}	1 >SiOH	-1 H$^+$	1 Am^{+++}		-0.7	2
>SiOAmO	1 >SiOH	-3 H$^+$	1 Am^{+++}	1 H$_2$O	14.20	0
>AlO$^-$	1 >AlOH	-1 H$^+$			9.730	-1
>AlOH$^+$	1 >AlOH	1 H$^+$			-8.330	1
>AlOPuO$^+$	1 >AlOH	1 PuO$_2^+$	-0.25 O$_2$(aq) -0.5 H$_2$O		-1.03	1
>AlOPuO$_2^-$	1 >AlOH	-2 H$^+$	1 PuO$_2^+$	-0.25 O$_2$(aq) 0.5 H$_2$O	16.85	-1
>AlOPuO$_2$	1 >AlOH	1 PuO$_2^+$			3.090	0
>AlOUO$_2^+$	1 >AlOH	-1 H$^+$	1 UO$_2^{++}$		-3.130	1
>AlONpO$_2$	1 >AlOH	-1 H$^+$	1 NpO$_2^+$		4.670	0
>AlONpO$_3$H$^-$	1 >AlOH	-2 H$^+$	1 NpO$_2^+$	1 H$_2$O	14.26	-1
>AlOAm^{++}	1 >AlOH	-1 H$^+$	1 Am^{+++}		-2.490	2
Calcite						
>PuO$_2^+$	1 >Ca^{++}	-1 Ca^{++}	1 PuO$_2^+$		-1.850	1
>UO$_2^{++}$	1 >Ca^{++}	-1 Ca^{++}	1 UO$_2^{++}$		-5.120	2
>NpO$_2^+$	1 >Ca^{++}	-1 Ca^{++}	1 NpO$_2^+$		-2.350	1
>AmCO$_3^+$	1 >Ca^{++}	-1 Ca^{++}	1 HCO$_3^-$ -1 H$^+$ 1 Am^{+++}		-1.587	1
>Sr^{++}	1 >Ca^{++}	-1 Ca^{++}	1 Sr^{++}		1.750	1

Source: Simmons 2002 [157578], SN-LANL-SCI-234-VI, p.29.

Table 10.3-5.   Ion Exchange Selectivity Coefficients and Fitted Cation Exchange Capacity (CEC)

Cation	Selectivity Coefficient
Na^+	1.
Cs^+	12.5
Sr^{++}	2.857
K^+	5.
Mg^{++}	2.
Ca^{++}	2.5
	CEC (mol/kg solid)
	0.02

NOTE: Selectivity coefficients modified from
Appelo 1996 [156425], pp. 197.

Source: Simmons 2002 [157578], SN-LANL-SCI-
234-V1, p. 28.

Table 10.3-6.   Composition of Injected Fluid

Table 10.3-6a. Primary Species Properties					
Species	Molality	Total Concentration	Activity Coeff.	Species Activity Ratio/H$^+$	Constraint
Ca^{++}	6.7143×10^{-4}	7.2355×10^{-4}	6.7444×10^{-1}	1.1936×10^{1}	1 total
K$^+$	3.0692×10^{-4}	3.0692×10^{-4}	8.9884×10^{-1}	4.0415	1 total
Mg^{++}	6.3025×10^{-4}	6.9944×10^{-4}	6.8849×10^{-1}	1.1908×10^{1}	1 total
Na$^+$	5.2197×10^{-3}	5.2197×10^{-3}	9.0166×10^{-1}	5.2721	1 total
Cl$^-$	2.4696×10^{-3}	2.4706×10^{-3}	8.9884×10^{-1}	-1.0162×10^{1}	−1 charge
SO$_4^{-2}$	5.9941×10^{-4}	6.6627×10^{-4}	6.5908×10^{-1}	-1.8331×10^{1}	1 total
HCO$_3^-$	4.4631×10^{-3}	4.7528×10^{-3}	9.0166×10^{-1}	−9.9048	1 total
F$^-$	1.9919×10^{-5}	2.0154×10^{-5}	9.0027×10^{-1}	-1.2255×10^{1}	1 total
SiO$_2$(aq)	3.6615×10^{-4}	3.6615×10^{-4}	1.0000	−3.4363	1 total
H$^+$	2.7897×10^{-8}	2.0345×10^{-4}	9.1373×10^{-1}	0.0000	3 calcite
Al^{+++}	3.5938×10^{-17}	5.5068×10^{-10}	4.4062×10^{-1}	6.2189	3 K-feldspar
Fe^{++}	1.0078×10^{-11}	1.6446×10^{-11}	6.7444×10^{-1}	4.1123	3 goethite
Sr^{++}	4.7300×10^{-13}	5.0000×10^{-13}	6.6693×10^{-1}	2.7837	1 total
PuO$_2^+$	9.9671×10^{-15}	4.0000×10^{-9}	9.0166×10^{-1}	−6.4470	1 total
UO$_2^{++}$	1.1940×10^{-17}	1.1110×10^{-10}	6.6305×10^{-1}	−1.8141	1 total
NpO$_2^+$	7.1760×10^{-11}	1.1150×10^{-10}	9.0166×10^{-1}	−2.5897	1 total
Am^{+++}	7.5783×10^{-14}	2.0000×10^{-11}	4.0148×10^{-1}	9.5429	1 total
Cs$^+$	4.0000×10^{-13}	4.0000×10^{-13}	8.9736×10^{-1}	−4.8435	1 total
O$_2$(aq)	1.2611×10^{-48}	-1.0030×10^{-9}	1.0000	-4.7899×10^{1}	4 O$_2$(g)

Solution conditions:

      Temperature: 25.0ºC   Ionic strength: 1.0087×10^{-2} Solution density: 0.99780 g/cm^3

      pH: 7.5936   pe: 1.931   Eh: 1.1430×10^{-1} V

      Charge balance: −q = -6.3071×10^{-16}

Computational parameters:

      Boundary condition: type 1   Iterations: 5

Source: Simmons 2002 [157578], SN-LANL-SCI-234-V1, p. 31.

Table 10.3-6 continued. Composition of Injected Fluid

Table 10.3-6b. Properties of Complexes				
Complex	Molality	Activity Coeff.	Species Activity/H$^+$	log K
$CO_2(aq)$	2.25165×10^{-4}	1.0000	–3.6475	6.3414
$MgSO_4(aq)$	4.43159×10^{-5}	1.0000	–4.3534	2.4125
$CaSO_4(aq)$	2.25424×10^{-5}	1.0000	–4.6470	2.1004
$CaHCO_3^+$	2.23075×10^{-5}	0.90166	2.9029	1.0429
$MgHCO_3^+$	2.08899×10^{-5}	0.90166	2.8744	1.0329
CO_3^{-2}	1.12691×10^{-5}	0.66305	–20.057	–10.325
$CaCO_3(aq)$	7.00620×10^{-6}	1.0000	–5.1545	–7.0088
$MgCO_3(aq)$	3.01655×10^{-6}	1.0000	–5.5205	–7.3562
$MgCl^+$	7.76285×10^{-7}	0.90166	1.4445	–0.13865
OH^-	4.44777×10^{-7}	0.90027	–13.906	–13.991
$CaCl^+$	2.22229×10^{-7}	0.90166	0.90124	–0.70039
MgF^+	1.92570×10^{-7}	0.90166	0.83903	1.3486
CaF^+	4.28435×10^{-8}	0.90166	0.18632	0.67736
$Pu(OH)_4(aq)$	3.99990×10^{-9}	1.0000	–8.3980	–13.920
$CaOH^+$	2.78300×10^{-9}	0.90166	–1.0010	–12.850
AlO_2^-	5.49982×10^{-10}	0.90166	–16.814	–22.879
$CaCl_2(aq)$	4.95545×10^{-10}	1.0000	–9.3049	–0.65346
$UO_2(CO_3)_3^{-4}$	5.83351×10^{-11}	0.18815	–40.452	–9.4530
$UO_2(CO_3)_2^{-2}$	5.18682×10^{-11}	0.65908	–25.394	–3.7613

Source: Simmons 2002 [157578], SN-LANL-SCI-234-V1, p. 90.

Table 10.3-6c. Mineral Saturation Indices		
Mineral	Saturation Index	log K
Dolomite	1.16594	–2.52402
Hematite	9.59704×10^{-1}	1.68702×10^{1}
Quartz	5.69305×10^{-1}	4.00565
Chalcedony	2.98104×10^{-1}	3.73444
Goethite	0.00000	7.95526
Calcite	0.00000	–1.85424
K-feldspar	0.00000	2.94216×10^{-1}
$Pu(OH)_4$	-1.57462×10^{-1}	–5.67951
Magnesite	-4.62767×10^{-1}	–2.29848
SiO_2(am)	-7.16385×10^{-1}	2.71996
Kaolinite	–1.70898	–6.79726
Gibbsite	–1.77543	–7.75591
Muscovite	–1.90002	-1.35668×10^{1}
Gypsum	–2.27448	4.47292
Beidellite-Ca	–2.29087	–5.56815
Sepiolite	–3.72692	-3.04075×10^{1}
Brucite	–4.47379	-1.62984×10^{1}
Magnetite	–5.38525	6.50570

Source: Simmons 2002 [157578], SN-LANL-SCI-234-V1, p. 32.

Table 10.3-6d. Gas Compositions			
Gas	log Partial Pressure	Pressure (bars)	log K
O_2(g)	–45.00	1.0000×10^{-45}	2.8993
CO_2(g)	–2.180	6.6104×10^{-3}	7.8092

Source: Simmons 2002 [157578], SN-LANL-SCI-234-V1, p. 32.

Table 10.3-7. Fitted Surface Complexation Site Densities

Site	Concentration (mol/bulk dm^3)
>FeOH	4.0×10^{-7}
>AlOH, >SiOH	5.0×10^{-6}
>Ca++	1.0×10^{-7}

Source: Simmons 2002 [157578], SN-LANL-SCI-234-V1, p. 28.

Table 10.3-8. Contribution of Radionuclides to Surface Complexation Sites

Component	Site	Mineral K_d (dm^3/dm^3)	Retardation: 1 + K_d	% Adsorbed
Sr^{++}	>FeOH	5.9996×10^{-5}		
	>SiOH	0.0000		
	>AlOH	0.0000		
	>Ca^{++}	4.9530×10^{-6}		
Total of all sites:		6.4949×10^{-5}	1.0001	6.4945×10^{-3}
PuO$_2^+$	>FeOH	2.3473×10^1		
	>SiOH	1.7024×10^{-11}		
	>AlOH	3.4754×10^1		
	>Ca^{++}	7.0217×10^{-8}		
Total of all sites:		5.8227×10^1	5.9227×10^1	9.8312×10^1
UO$_2^{++}$	>FeOH	4.4734×10^{-2}		
	>SiOH	1.1785×10^{-3}		
	>AlOH	5.7571×10^{-3}		
	>Ca^{++}	4.1468×10^{-6}		
Total of all sites:		5.1674×10^{-2}	1.0517	4.9135
NpO$_2^+$	>FeOH	7.7954×10^{-3}		
	>SiOH	7.5785×10^4		
	>AlOH	7.5055×10^{-4}		
	>Ca^{++}	5.7351×10^{-2}		
Total of all sites:		7.5785×10^4	7.5786×10^4	9.9999×10^1
Am^{+++}	>FeOH	4.9624×10^{-1}		
	>SiOH	3.9129×10^{-1}		
	>AlOH	2.8157×10^1		
	>Ca^{++}	4.0926		
Total of all sites:		3.3137×10^1	3.4137×10^1	9.7071×10^1

Source: Simmons 2002 [157578], SN-LANL-SCI-234-V1, p. 33.

Table 10.4-1. Measurements of U-Th Isotopic Composition and Concentration in Various Water Samples Collected near the Nopal I Uranium Deposit

Sampling Location	Sample ID	Collection Date	U (ppb)	(+/-) (%)	$^{234}U/^{238}U$ atom ratio (×10^{-6})	(+/-) (%)	δD (‰)	δ^{18}O (‰)	Notes
Perched water from borehole at +10 level	BH12W95-5	August 1995	4.79	0.20	119.66	0.18			
	BH12W95-11	September 1995	5.77	0.25	120.86	0.14			
	AS-5	25 February 2000	5.73	0.19	156.75	0.10	-64	-9.3	
	030701 2001	7 March 2001	10.40	0.19	112.59	0.11			
8.5 m into north part of adit at +00 level	ADIT95-6	September 1995	0.20	2.4	278.40	0.16			
	AS-4	25 February 2000	2.87	0.30	121.15	0.25	-1	-2.8	
	030701-02	7 March 2001	1.20	0.24	142.05	0.20			E in Figure 10.4-1
23 m from adit entrance	ADIT95-9	September 1995	0.89	0.54	156.16	0.11			
	AS-3	February 2000	4.03	0.19	64.61	0.18	-7	-3.6	
	030701-03	7 March 2001	26.96	0.18	64.36	0.10			D in Figure 10.4-1
15 m from adit entrance	AS-2	25 February 2000	36.92	0.19	51.53	0.16	-7	-3.4	
	030701-04	7 March 2001	16.49	0.28	50.51	0.40			C in Figures 10.4-1, 10.4-2
12 m from adit entrance	AS-1	25 February 2000	68.46	0.19	58.21	0.14	-11	-2.5	B in Figures 10.4-1, 10.4-2
5 m from adit entrance	030701-05	7 March 2001	13.01	0.23	56.14	0.20			A in Figures 10.4-1, 10.4-2
Abandoned mining camp supply well	AS-6	25 February 2000	2.53	0.25	64.93	0.30			
Poços Ranch	WVW95-03	September 1995	0.17	2.8	76.02	0.22			Well
	AS-7	25 February 2000	0.27	1.0	140.00	1.0	-61	-8.7	Holding Tank
	030701-06	7 March 2001	5.71	0.19	111.69	0.10			Holding Tank

Source: 1995 samples from Pickett and Murphy 1999 [110009], Table II.
2000 and 2001 samples from Simmons 2002 [157578], SN-LANL-SCI-237-V1, p. 16; SN-LBNL-SCI-108-V1, pp. 86, 87.